IARD

- Institute for Advanced Research and Development

IARD 15-99 (105-1)

Unclassified

Final Research Report

Comparison of Atmospheric Transmittance Measurements in the 3-5 μm and 8-12 μm Spectral Regions with MODTRAN: Consideration for long path geometries

Adam D. Devir

IARD – Institute for Advanced Research & Development

June 1999

Contract F61775-98-WE082, Project SPC-98-4042, EOARD, USAF.

47, Ha-Taasia Str., POB 271, Industrial Park Tel-Hanan, Nesher, 20302
Tel. 972-4-8216402, Fax. 972-4-8216396
E-mail: iardad@IARD.org.il

Comparison of Atmospheric Transmittance Measurements in the 3-5 μm and 8-12 μm Spectral Regions with MODTRAN: Consideration for long path geometries

Date: 27/01/99	Authors: Dr. A. D. Devir
Classification: Unclassified	Checked by: Prof. A. Lessin
Requested by: EOARD USAF	Approved by: Dr. Y. Bushlin
Order number: Contract F61775-98-WE082, Project SPC-98-4042, EOARD, USAF, Item 0002	Report type: Final Research Report
Distribution: EOARD USAF	Language: English
Remarks:	Reference: IARD 15-99 (105-1)

ABSTRACT

This work was performed as a part of the contract **F61775-98-WE082** "***Comparison of Atmospheric Transmittance Measurements in the 3-5μm and 8-12μm Spectral Regions with MODTRAN: Consideration for long path geometries***", in accordance with the item 0002 of the project SPC-98-4042.

Radiance measurements conducted during tropospheric operations to detect objects on the Earth's surface from a manned aircraft or from an unmanned airborne vehicle (UAV) will involve long, near-horizontal viewing geometries. The computer code MODTRAN is widely used for the prediction of the propagation of infrared radiation through the lower atmosphere.

This program was undertaken by the IARD to test and validate the predictions of the MODTRAN code for the 3-5μm and 8-12μm spectral regions under semi-arid desert conditions with well defined meteorological parameters.

The first stage of the project included preparation and performing field-test experiments. The final stage includes analysis of received experimental data and performing parametric calculations of atmospheric transmittance by code MODTRAN 3.7.

This document describes results of the performed analysis and comparison of the theoretical predictions of MODTRAN 3.7 to the experimental results.

Principal investigator: **Dr.** Adam D. Devir

IARD–Institute for Advanced Research & Development

CONTENTS

1. INTRODUCTION

Objective

The purpose of this research was to refine space atmospheric transmittance measurements in the 3-5 and 8-12 μm spectral regions and to compare them with the latest predictions of the MODTRAN code. Past experimental work [1] had demonstrated that the computer code MODTRAN 3.7, widely used for the prediction of the propagation of infrared radiation through the lower atmosphere, gives rather good agreement with experimental results (see following paragraph). The results of the research effort reported herein have a strong impact on the potential use of this code to predict the data expected from IR sensors to be deployed for observation and detection of objects located on the Earth's surface, from either a manned aircraft or from an unmanned airborne vehicle (UAV). The fact that these observation were made in very long near-horizontal optical paths tests the validity of the code at the extreme of its potential use.

Early atmospheric transmittance measurements were conducted in Israel in June 1990. These measurements were made in the 3-5μm and 8-12μm spectral region with spectral resolution of $\Delta\lambda/\lambda=0.04$. The instrument used was a circular-variable-filter (CVF) spectroradiometer. The comparison of the experimental results with MODTRAN predictions showed good agreement in the 3-5μm spectral region but poorer agreement in the 8-12μm spectral region [1].

Following these early measurements it was proposed to EOARD to conduct a more intensive campaign of field tests of atmospheric transmittance measurements in long near-horizontal path geometries under desert conditions, if possible. The proposed campaign was planned to take place in Israel in the summer (July-August) 1998. However, it was actually performed only in the beginning of the winter (November 1998 - January 1999). During this period we managed to make three field tests.

This report compares the theoretical predictions of MODTRAN 3.7 to the experimental results that were obtained in the third field-test that took place in Mitzpe' Ramon (altitude 850m) in the southern part of Israel (the Negev). A general view of the experimental set-up is shown in Figure 1. In this field-test we made good atmospheric transmittance measurements during January 11th and 12th. The visibility conditions were very good and there were no indications for thin cirrus clouds.

2. THE FIELD TEST

The Experimental Set-up

In this field-test we used the SR-5000 spectroradiometer that has a spectral resolution of $\Delta\lambda/\lambda$=0.02 (according to the manufacturer). This is a CVF spectroradiometer with a Newtonian optics with 5" aperture and focal length of 20" (F#=4.0). A general description of the optical layout of the SR-5000 is shown in Figure 2. The main advantages of this completely computerised spectroradiometer are its ruggedness, its suitability for field experiments and its simple and easy modes of operation. The SR-5000 can make a complete spectral scan within a predetermined time (from 0.1sec to 64sec). We decided to operate it at an optimal scan rate of 2sec/scan. The corresponding chopper (50% duty cycle) frequency was chosen to be 800Hz. The CVF in our model spanned the whole spectral region from 1.3μm to 14μm. To cover this spectral region, the detector in the SR5000 is an InSb/CMT "sandwich" detector with automatic switching between the two elements at λ=5.7μm.

The Field-Of-View (FOV) of this spectroradiometer was chosen to be 0.5mrad (though it can be varied from 0.3mrad to 6mrad). This value enabled us to make radiometric measurements of the sun (T_s=5900K) and of the calibration blackbody (T_c =1273K) almost without saturation at the short wavelengths (λ=2.8μm) while measuring the sun, and without having to deal with very low signal levels in this spectral region while measuring the calibration blackbody (see Figure 27, below). Since the SR-5000 can be operated with 4 different setting of fixed gain (1, 10, 100, and 1000), we chose to operate the SR-5000 with the largest FOV setting together with the smallest gain setting (to avoid the introduction of unnecessary noise). The operation of the SR-5000 with FOV=0.5mrad was possible with gain=1. Though there was some saturation in the NIR wavelengths (λ=1.3-2.0μm) while measuring the sun, the measurements in the spectral region of interest (3-5μm and 7-14μm) was obtained with very high signal-to-noise (S/N) ratios.

The Measurement Theory

The atmospheric transmittance measurements with the SR-5000 are based on a very simple theory because both the calibration process of the spectroradiometer by external

blackbody and the measurements of the sun are made with full FOV. A full FOV means that the angular dimension of the measured object is larger than the angular dimension of the FOV. In this configuration the dependence of the measured signal on the measurement distance is only through the effect of the atmospheric transmittance and the actual size of the FOV (see below). In our tests the calibration was done from a distance of about 15m. This distance is sufficient small so that the angular dimension of the aperture of the blackbody (diameter = 22.2mm or 1.48 mrad) was larger than the FOV (0.5mrad).

It can be shown that during the calibration the measured signal $V_c(\lambda)$ can be expressed as:

(1) $$V_c(\lambda) = K\cdot \{P(T_c, \lambda)\cdot\tau_c(L_c, \lambda) - P(T_{ibb},\lambda)\}\cdot FOV_c^2 \cdot A_{rad}\cdot F(\lambda)\cdot R(\lambda)$$

Where: $V_c(\lambda)$ is the measured signal (V).

K is a proportionality constant (Volt/Watt).

$P(T_c, \lambda)$ is Planck's function at T_c = 1273K (Watt/str·cm^2·μm)

$\tau_c(L_c, \lambda)$ is the atmospheric transmittance for the calibration distance L_c.

L_c is the calibration distance (cm).

$P(T_{ibb},\lambda)$ is Planck's function at the temperature of the internal blackbody.

FOV_c is the angular dimension of the FOV of the SR-5000 during the calibration stage (mrad).

A_{rad} is the clear aperture of the SR-5000 (cm^2).

$F(\lambda)$ is the spectral transmittance of the CVF

$R(\lambda)$ is the relative response of the InSb/CMT detector.

Calculation shows that the radiance of the internal blackbody (T_{ibb}=300K) which is the second term in the { } in Eq. 1 is very small compared to radiance of the calibration blackbody (T_c=1273K) which is the first term in { } and therefore can be neglected. Hence Eq. 1 can be rewritten as:

(2) $$V_c(\lambda) = K\cdot P(T_c, \lambda)\cdot\tau_c(L_c, \lambda)\cdot FOV_c^2 \cdot A_{rad}\cdot F(\lambda)\cdot R(\lambda)$$

The signal obtained during the measurement of the sun - $V_m(\lambda)$ - can be expressed as:

$$(3) \quad V_m(\theta, \lambda) = K \cdot FOV_0^2 \cdot A_{rad} \cdot F(\lambda) \cdot R(\lambda) \cdot \{P(T_s, \lambda) \cdot \tau_m(\theta, \lambda) + I_{scatt}(\lambda) + [1-\tau_m(\theta, \lambda)] \cdot P(T_{amb}, \lambda) - P(T_{ibb}, \lambda)\}$$

Where: $V_m(\theta, \lambda)$ is the measured signal as a function of the zenith angle θ (V).

$P(T_s, \lambda)$ is Planck's function at $T_s = 5900K$[3] (Watt/str·cm^2·μm).

$\tau_m(\theta, \lambda)$ is the ground-to-space atmospheric transmittance for zenith angle θ.

$P(T_{ibb}, \lambda)$ is Planck's function at the temperature of the internal blackbody.

FOV_0 is the angular dimension of the FOV of the SR-5000 during the measurement of the sun (mrad).

The second term, which is the solar radiance scattered into the FOV (by the atmosphere and by internal surfaces located in the SR-5000) was measured (by measuring the sky very close to the solar disk) to be is very small compared to the first term (see below). The same can be said as for the path radiance (the third term) and the radiance of the internal blackbody. Consequently Eq. (3) can be rewritten as:

$$(4) \quad V_m(\theta, \lambda) = K \cdot FOV_m^2 \cdot A_{rad} \cdot F(\lambda) \cdot R(\lambda) \cdot \{P(T_m, \lambda) \cdot \tau_m(\theta, \lambda)$$

From Eqs. (4) and (2) we obtain that the ground-to-space atmospheric transmittance for zenith angle θ - $\tau_m(\theta, \lambda)$ - can be expressed as:

$$(5) \quad \tau_m(\theta, \lambda) = \tau_c(\lambda) \cdot [V_m(\theta, \lambda)/V_c(\lambda)] \cdot [P(T_c, \lambda)/P(T_s, \lambda)] \cdot [FOV_c/FOV_m]^2$$

The last term is due to the fact that the FOV of the spectroradiometer is determined by the equation:

$$(6) \quad FOV = \pi \cdot (d/v)^2/4$$

Where d is the diameter of the field stop and v is the distance between the field stop and the primary mirror. During the measurement of the sun is measured the SR-5000 is focused to infinity so that v = f. However, during the calibration stage the SR-5000 is focused to fairly large distance (L_c ~15m) but not to infinity. Simple calculation show us that $v = f\cdot[L_c/(L_c-f)]$. For f = 51cm (20") and L_c = 1500cm one obtains that $v = f\cdot 1.035$. Hence, for L_c = 1500cm one obtains that:

(7) $$[FOV_c/FOV_m]^2 = [f/v]^2 = [(L_c - f) / L_c]^2 = 0.933$$

For L_c =1600cm one obtains that $[FOV_c/FOV_m]^2 = 0.937$, and for L_c =1700cm one obtains that $[FOV_c/FOV_m]^2 = 0.933$. This means that (a reasonable) 5cm error in the measured calibration distance L_c (that was always between 15m and 17m) will yield only a negligible relative error of 0.02% in the value of $[FOV_c/FOV_m]^2$.

We checked the magnitude of the second term in Eq. 3 (the solar radiance scattered into the FOV) by measuring the sky just near the sun with special care not to overheat the internal blackbody. During these tests it was discovered that the amplifiers of the SR-5000 did not have an accurate zero DC offset. Therefore, this offset (or artificial background) was measured and subtracted from all our measured signals. This DC offset changes with the transition from the amplifier of the InSb detector to the amplifier of the CMT detector - a transition that takes place at λ=5.7μm.

It should be noted that for each zenith angle we made 50 successive measurements. From the average of these 50 measurements – $V'_m(\lambda)$ - the offset/background signal was subtracted to produce the true signal – $V_m(\lambda)$. Similar average and subtraction was made on the calibration signal - $V'_c(\lambda)$ - to obtain the true calibration signal – $V_c(\lambda)$. The true calibration and measurements signals were introduced to Eq. 5.

3. THE RESULTS

As mentioned earlier good experimental results were obtained from the two-day campaign that took place in Mitzpe' Ramon in the Negev in January 11 and 12, 1999.

The profiles of the air pressure (in mb) - $P_{air}(h)$, air temperature (in C) - $T_{air}(h)$ and water vapour density (in gr/m^3) - $\rho_{water}(h)$ that were measured by the radiosonde in the morning of these two days are summarised in Table 1 and 2, respectively, and are shown in Figures 3,4 and 5, respectively.

The meteorological parameters that were measured on the ground (H=0.85km) on 11/1/99 and 12/1/99 are summarised in Table 3 and 4, respectively. These parameters were used to clamp the radiosonde profile to the ground temperature, pressure and absolute humidity (in gr/m^3).

These profiles were clamped to the actual surface values according to the following method: Since the radiosonde balloon was released in the morning, its data does not represent the exact meteorological conditions along the day. To overcome this problem, the meteorological conditions along the day were calculated from the radiosonde data by clamping the air temperature - $T_{air}(h)$, the water vapour content - $\rho_{water}(h)$ and the pressure $P_{air}(h)$ to the ground data. This clamped profile was obtained according to the following equations:

(8) $$T_{air,\ ground\ clamped}(h) = T_{air,\ sonde}(h) + \Delta T$$

(9) $$\rho_{water,\ ground\ clamped}(h) = \rho_{water,\ sonde}(h) \cdot K$$

(10) $$P_{air,\ ground\ clamped}(h) = P_{air,\ sonde}(h) \cdot G$$

Where:

$\Delta T = T_{ground}(h=850m) - T_{air,\ sonde}(h=850m)$

$K = \rho_{ground}(h=850m) / \rho_{water,\ sonde}(h=850m)$

$G = P_{ground}(h=850m) / P_{air,\ sonde}(h=850m)$

According to the statistical behaviour of the altitude profiles of T, ρ and P in Israel, this clamping is valid for altitudes, ranging from Mitzpe' Ramon ground level (h=0.85 km) up to altitude of h=10 km.

The MODTRAN 3.7 code was run according to the ground "clamped" radiosonde profiles. We used a rural aerosol model since it is the most suitable one for the region involved as long as the desert aerosol model is not recommended. The final transmittance values were scanned with a Gaussian slit-function with FWHM=3% of the wavelength. This value is somewhat higher than the value quoted by the manufacturer (FWHM=2%). When we used FWHM=2% we obtained in the predicted transmittance values distinct spectral features that are not distinct in our current measurements.

The results from the measurements made at zenith angles between 80° and 89° in the evening of January 11,1999 appear in Figures 6 to 15. Each figure is composed of two parts "a" and "b". Part "a" refers to the 2.8-5.4μm spectral region and part "b" refers to the 7-13μm spectral region.

The results from the measurements made at zenith angles between 80° and 89° in the morning of January 12,1999 appear in Figures 16 to 25. Each figure is composed of two parts "a" and "b". Part "a" refers to the 2.8-5.4μm spectral region and part "b" refers to the 7-13μm spectral region.

Above each of these figures there is full documentation of the MODTRAN parameters that were used. The code was executed in ground-to-space (ITYPE=3) transmittance mode (IEMSCT=0) with user-specified radiosonde data (MODEL=7):

The first line presents the atmospheric model of all atmospheric constituents that do not appeare in the user-specified radiosonde data (Midlatitude Winter) - and the different flags used in the code: (X, Y - 1:1, 2:2, 3:3, 4:4 = r,n-w,3,r,a).

The second line presents the CO_2 concentration (360 ppm), the aerosol model (Rural) and the ground altitude (0.85km).

The third line presents the initial (0.85km) and final (0km - this value is not relevant in ground to space geometry - ITYPE=3) altitudes.

The fourth line presents the initial wavenumber ($740cm^{-1}$) , the final wavenumber ($6500cm^{-1}$), the wavnumber increment ($5cm^{-1}$) and the width of the slit-function (FWHM=3%).

The fifth line presents the visibility, the zenith angle, and the ground altitude (0.85km) used to clamp the radio sonde data to the ground meteorological parameters: P(mb), T(K) and the water content of the atmosphere (gr/cm^3).

It should be noted that after the end of the test it was discovered that a small angle shift of 10' (or 0.17°) has to be added to all elevation readings. This small shift in the reading was caused by small vernir knob in the teodolite that was not zeroed. Therefore, we added 0.17° to all elevations, or actually, we subtracted 0.17° from all zenith angles.

Layer #	Alt. (km)	T (C)	T(K)	P(mb)	Water (gr/m^3)
1	0	19.4	2.926E+02	1.020E+03	5.381E+00
2	0.1	18.3	2.915E+02	1.009E+03	5.472E+00
3	0.2	17.2	2.904E+02	9.980E+02	5.563E+00
4	0.3	16.2	2.894E+02	9.860E+02	5.652E+00
5	0.4	15.4	2.886E+02	9.740E+02	5.516E+00
6	0.5	15.0	2.882E+02	9.630E+02	5.127E+00
7	0.75	13.6	2.868E+02	9.350E+02	4.235E+00
8	0.85	12.8	2.860E+02	9.230E+02	4.143E+00
9	1	11.6	2.848E+02	9.070E+02	3.844E+00
10	1.25	9.3	2.825E+02	8.800E+02	3.234E+00
11	1.5	7.3	2.805E+02	8.540E+02	2.448E+00
12	2	6.5	2.797E+02	8.040E+02	7.497E-01
13	2.5	4.3	2.775E+02	7.560E+02	6.485E-01
14	3	1.9	2.751E+02	7.110E+02	5.519E-01
15	3.5	-0.4	2.728E+02	6.680E+02	4.243E-01
16	4	-4.3	2.689E+02	6.270E+02	3.583E-01
17	4.5	-7.2	2.660E+02	5.880E+02	2.904E-01
18	5	-10.8	2.624E+02	5.510E+02	2.221E-01
19	6	-18.1	2.550E+02	4.780E+02	1.401E-01
20	7	-25.2	2.479E+02	4.155E+02	7.005E-02
21	8	-32.2	2.409E+02	3.600E+02	4.003E-02
22	9	-38.9	2.343E+02	3.106E+02	2.001E-02
23	10	-44.5	2.286E+02	2.675E+02	1.001E-02
24	12	-50.7	2.225E+02	2.102E+02	6.204E-03
25	14	-53.5	2.196E+02	1.528E+02	2.402E-03
26	16	-56.8	2.163E+02	1.104E+02	4.503E-04
27	18	-58.0	2.152E+02	8.283E+01	3.502E-04
28	20	-55.6	2.175E+02	5.529E+01	2.502E-04
29	25	-47.5	2.257E+02	2.440E+01	2.252E-04
30	30	-41.8	2.314E+02	1.085E+01	2.001E-04
31	35	-27.3	2.459E+02	5.202E+00	1.076E-04
32	40	-12.8	2.603E+02	2.611E+00	1.501E-05
33	45	-8.3	2.648E+02	1.296E+00	9.081E-06
34	50	-3.8	2.693E+02	6.829E-01	3.152E-06
35	70	-38.1	2.350E+02	4.690E-02	7.005E-08
36	100	-58.6	2.145E+02	3.013E-04	5.003E-10

Table 1: The meteorological profile of 11.1.99

Layer #	Alt. (km)	T (C)	T(K)	P(mb)	Water (gr/m^3)
1	0	12.9	2.861E+02	1.006E+03	3.267E+00
2	0.1	12.9	2.861E+02	1.006E+03	3.267E+00
3	0.2	19.6	2.928E+02	9.940E+02	4.895E+00
4	0.3	18.5	2.917E+02	9.830E+02	4.746E+00
5	0.4	17.6	2.908E+02	9.720E+02	4.499E+00
6	0.5	16.6	2.898E+02	9.600E+02	4.378E+00
7	0.75	14.2	2.874E+02	9.320E+02	3.906E+00
8	0.85	13.2	2.864E+02	9.210E+02	3.787E+00
9	1.0	11.9	2.851E+02	9.050E+02	3.705E+00
10	1.25	9.7	2.829E+02	8.780E+02	2.949E+00
11	1.5	8.6	2.818E+02	8.520E+02	2.319E+00
12	2.0	9.4	2.826E+02	8.020E+02	1.718E+00
13	2.5	6.1	2.793E+02	7.550E+02	1.388E+00
14	3.0	3.4	2.766E+02	7.100E+02	1.160E+00
15	3.5	0.2	2.734E+02	6.670E+02	9.337E-01
16	4.0	-3.4	2.698E+02	6.260E+02	8.023E-01
17	4.5	-5.8	2.674E+02	5.880E+02	5.790E-01
18	5.0	-9.8	2.634E+02	5.510E+02	4.550E-01
19	6.0	-17.0	2.562E+02	4.773E+02	2.112E-01
20	7.0	-24.1	2.491E+02	4.149E+02	1.056E-01
21	8.0	-31.1	2.421E+02	3.594E+02	6.035E-02
22	9.0	-37.8	2.354E+02	3.101E+02	3.017E-02
23	10.0	-43.4	2.298E+02	2.671E+02	1.509E-02
24	12.0	-49.6	2.236E+02	2.098E+02	9.354E-03
25	14.0	-52.4	2.208E+02	1.526E+02	3.621E-03
26	16.0	-55.7	2.175E+02	1.102E+02	6.789E-04
27	18.0	-56.9	2.163E+02	8.270E+01	5.280E-04
28	20.0	-54.5	2.186E+02	5.521E+01	3.772E-04
29	25.0	-46.3	2.268E+02	2.437E+01	3.395E-04
30	30.0	-40.6	2.325E+02	1.083E+01	3.017E-04
31	35.0	-26.2	2.470E+02	5.194E+00	1.622E-04
32	40.0	-11.7	2.615E+02	2.607E+00	2.263E-05
33	45.0	-7.2	2.660E+02	1.293E+00	1.369E-05
34	50.0	-2.7	2.705E+02	6.818E-01	4.752E-06
35	70.0	-37.0	2.362E+02	4.683E-02	1.056E-07
36	100.0	-57.5	2.157E+02	3.008E-04	7.544E-10

Table 2: The meteorological profile of 12.1.99

Date	Local Time	Zenith Angle	File #	T(C)	T(K)	P(Torr)	Water (gr/m^3)	VIS (km)	P(mb)
11/1	08:20	72	11m72	10.00	282.2	696.0	5.82	32.5	927.7
11/1	08:32	70	11m70	10.75	283.9	696.0	6.60	32.5	927.7
11/1	08:51	67	11m67	12.25	285.4	696.0	6.60	32.5	927.7
11/1	08:59	65	11m65	13.00	286.2	696.0	6.46	32.5	927.7
11/1	09:19	63	11m63	13.50	286.7	696.0	6.43	32.5	927.7
11/1	08:44	60	11m60	14.50	287.7	696.0	6.47	32.5	927.7
11/1	15:14	72	11e72	17.00	290.2	696.5	5.79	32.5	928.4
11/1	15:26	74	11e74	17.00	290.2	696.5	5.79	35	928.4
11/1	15:38	76	11e76	17.00	290.2	695.0	5.79	35	926.4
11/1	15:49	78	11e78	16.00	289.2	695.0	5.99	35	926.4
11/1	16:00	80	11e80	15.50	288.7	695.0	5.42	32.5	926.4
11/1	16:06	81	11e81	15.50	288.7	695.0	5.42	32.5	926.4
11/1	16:12	82	11e82	15.00	288.2	695.0	5.64	32.5	926.4
11/1	16:17	83	11e83	15.00	288.2	695.0	5.64	32.5	926.4
11/1	16:22	84	11e84	14.75	287.9	695.0	5.55	32.5	926.4
11/1	16:28	85	11e85	14.60	287.8	695.0	5.75	32.5	926.4
11/1	16:33	86	11e86	14.50	287.7	696.5	5.47	30	928.4
11/1	16:39	87	11e87	14.00	287.2	696.5	5.67	30	928.4
11/1	15:45	88	11e88	13.80	287.0	696.5	5.60	30	928.4
11/1	15:51	89	11e89	13.20	286.4	696.5	5.51	30	928.4

Table 3: Summary of all the meteorological parameters that were measured on the ground (H=0.85km) on 11/1/99.

Date	Local Time	Zenith Angle	File #	T(C)	T(K)	P(Torr)	Water (gr/m^3)	VIS (km)	P(mb)
12/1	06:44	89	12m89	7.00	280.2	696.5	4.34	35	928.4
12/1	06:49	88	12m88	6.75	279.9	696.5	4.50	35	928.4
12/1	06:55	87	12m87	6.50	279.7	696.5	4.57	35	928.4
12/1	07:01	86	12m86	6.50	279.7	696.5	4.35	35	928.4
12/1	07:06	85	12m85	7.20	280.4	696.5	4.47	35	928.4
12/1	07:11	84	12m84	8.00	281.2	696.0	4.30	35	927.7
12/1	07:17	83	12m83	8.00	281.2	696.0	4.30	35	927.7
12/1	07:22	82	12m82	8.00	281.2	696.0	4.71	35	927.7
12/1	07:28	81	12m81	8.00	281.2	696.0	4.30	35	927.7
12/1	07:33	80	12m80	8.50	281.7	696.0	4.44	35	927.7
12/1	07:44	78	12m78	9.00	282.2	696.0	4.67	35	927.7
12/1	07:56	76	12m76	10.00	283.2	696.0	5.17	35	927.7
12/1	08:07	74	12m74	11.20	284.4	696.0	4.96	35	927.7
12/1	08:19	72	12m72	11.80	285.0	696.0	5.79	35	927.7
12/1	08:32	70	12m70	12.50	285.7	696.0	5.38	35	927.7
12/1	09:04	65	12m65	14.00	287.2	695.5	5.67	35	927.0
12/1	09:51	59	12m59	16.00	289.2	695.5	5.18	35	927.0

Table 4: Summary of all the meteorological parameters that were measured on the ground (H=0.85km) on 12/1/99.

4. DISCUSSION OF THE RESULTS

From the results we see that there is very good agreement between the experimental data and the theoretical prediction of MODTRAN3.7 in low elevations, or in zenith angles close to 90°. As the elevation angle of our LOS increases - the agreement is reduced. This seems unreasonable from theoretical point of view since the largest errors in the composition of the atmosphere and its profile-dependent attenuating constituents (the aerosols and the absolute humidity) should be found in the lower atmospheric layers but far from the measurement point. These are the layers that have the major effect on the transmittance in the lower elevations - elevations where we obtained good matching between the theory and the experimental results. Consequently, the error in higher elevations is due to some other mechanism. This mechanism was found after long time to be in the heating of the detector element due to the average power (or flux) that reaches it from the FOV (or field stop).

The detector of the SR-5000 is an InSb-MCT "sandwich" detector (with diameter of 2mm) that can be "saturated" by high powers or fluxes (as well as by the electronics). This detector is composed of InSb element that is placed over an MCT element (there is some spacing between the two elements). Both elements are in good thermal contact with the heat sink that is intended to keep them at 77K. The D* value of the detector is increased by the use of cold-shield with full angle of 30°. Despite the fact that we operated the instrument with small FOV of 0.5mrad, the power that arrived to the detector from the sun disk (that filled that FOV of 0.5mrad) was very high. The spectral power (Watt/μm) that reaches the detector element from the sun can be calculated from the following equation:

$$P(\lambda)= \tau_m(\lambda)\cdot P(T_s, \lambda)\cdot (FOV_m)^2 \cdot A_{rad}\cdot \tau_{opt} \quad (11)$$

Where:

A_{rad} - is the clear aperture of the SR-5000 taken as A_{rad} =110cm^2 (for 5" aperture with 10% central obscuration).

τ_{opt} - is the average transmittance of all the optics of the SR-5000, taken as τ_{opt}=0.7.

The results of this calculation are shown in Figure 26. This figure shows the spectral power (W/μm) that reaches the detector element from the sun at two elevations: 10° and 1° compared

to the spectral power that reaches the detector from the aperture of the blackbody (1000C) used for the calibration. As one can see the spectral power from the sun, especially below 2.5μm, is more than two orders of magnitude higher than that of the calibration blackbody.

Moreover, the time-averaged power (due to the chopper with 50% duty cycle - see Figure 2) that reaches the detector element is 0.72mW at sun elevation of 10° compared to 0.31mW at sun elevation of 1°. These values are, again, two orders of magnitude higher than the average power of 0.005mW that reaches the detector at the calibration stage. It should be noted that these are very high powers if one compares them to the (calculated) power that reaches the 2mm-diameter detector (in the 30° cold-shield) from a uniform DC (un-chopped) uniform background at temperature T_b that fills the FOV of the cold-shield. This calculation shows that 0.31mW is equivalent to T_b = 380K and 0.72mW is equivalent to T_b = 465K (a value of 0.12mW is equivalent to T_b = 300K). It is quite evident that these are rather too hot equivalent backgrounds for normal detector operation especially when the sun is much above the horizon.

These high power levels (especially at high elevation angles) are heating the detector element to the limits of the capabilities of its heat dissipation to the heat sink. Therefore, it is highly probable that at these high power levels the detector temperature is higher than the desired value of 77K. **As a result of this heating, R(λ) - the value of the response function of the detector elements - are reduced (and also spectrally changed).** This reduction will manifest itself in lower detector signal - $V_m(\lambda)$ or lower measured values of the transmittance - $\tau_m(\theta, \lambda)$. It should be noted that the major part of this heating power is contributed from the spectral region below 2.5μm: 91% at elevation of 10° and 96% at elevation of 1°. It should be noted that our early measurements [1] were made with different spectroradiometer equipped with a CVF that blocked completely all radiation below 2.8μm, and did not transmit it to the detector. Therefore, we did not have in that field test, any problems of detector heating and response reduction.

Moreover, the high powers involved manifest themselves also in electronic saturation as can be seen from the magnitude of the raw signal. At elevation of 10° the signal levels of the detector (at 1.7μm) saturate the preamplifier, as can from the fixed signal level of 10V, as shown in Figure 27.

The DC heating of the detector elements manifest itself also in comparing the morning results (of January 12) to the evening results (of January 11). In the morning the whole radiometer was cooler thus improving the stability of the response function of the detector and enabling it to measure more accurately at higher elevations than in the evening.

As one can see there is unexplained spectral "tail" above 12.5μm in the measured transmittance on January 11, 1999. This feature is an artifact caused by the limited S/N of the SR-5000 system. This can be seen from figure 27 that shows that the magnitude of the measured signal - $V_m(\theta=89^\circ, \lambda>13\mu m)$ - is smaller than 2mV (for full scale of 10V). Since the SR-5000 is 14bit system then the LSB is about 10/16,384=0.6mV that means that we are hardly above noise level.

We found that at low elevation angles there is a good **absolute and spectral matching** between the experimental results and the MODTRAN3.7 prediction in the 2.8-5.4μm spectral region. Good matching is found also in the 8-12μm spectral region but not as good as in the 2.8-5.4μm spectral region.

In the 8-12μm spectral region there is some spectral discrepancy between the predicted results (scanned over the 3% FWHM Gaussian slit-function) and the experimental results. This discrepancy is especially noticeable at 8.5μm (see for example Figure 24b). Detailed examination of the contribution of different atmospheric constituents to the total absorption indicates that only N_2O and to less extent O_3 and CO_2 could have caused this discrepancy (see Figure 32 below).

A similar spectral discrepancy between the predicted and the experimental results is also found in the 3.8-4.0 spectral region (see for example Figure 19a). Again, a detailed analysis (see figure 33 below) indicates that only N_2O and CO_2 could have caused this discrepancy. The fact that the absorption and the mixing ratio of CO_2 is very well known, leaves N_2O as a possible cause for these discrepancies. Since the profile of these gases was taken from the Midlatitude Winter atmospheric profile (see section III above), there should be done some more profound analysis of the cause for these phenomena.

Another local discrepancy can be found in the fact that the MODTRAN 3.7 predictions at wavelengths below 3.5μm are somewhat lower than the measured (see figure 23a). Since the absorption in this spectral region is dominated by the water absorption (both line and continuum) and since the discrepancy is more-or-less spectrally uniform, it may be possible that the water continuum is responsible for it.

5. ERROR ANALYSIS

The validity of the experimental results depends on the error in the experimental data as well as in the parameters that affect the predicted transmittance values. The measured transmittance values are expressed according to Eq. (5):

$$\tau_m(\theta, \lambda)= \tau_c(\lambda)\cdot[V_m(\theta, \lambda)/V_c(\lambda)]\cdot[P(T_c, \lambda)/P(T_s, \lambda)]\cdot[FOV_c/FOV_m]^2$$

From this equation it is quite easy to calculate the relative error of the measured transmittance:

$$\begin{aligned}\Delta\tau_m(\theta, \lambda)/\tau_m(\theta, \lambda) = {} & \Delta V_m(\theta, \lambda)/V_m(\theta, \lambda) + \\ & \Delta V_c(\lambda)/V_c(\lambda) + \\ & \Delta P(T_c, \lambda)/P(T_c,\lambda) + \\ & ERR_{FOV}\end{aligned}$$

For the sake of simplicity, we'll calculate the average value of $<\Delta\tau_m(\theta, \lambda)/\tau_m(\theta, \lambda)>$ in two spectral regions: 3-5μm and 8-12μm.

It was already shown that the expected relative error in the term $[FOV_c/FOV_m]^2$ is equal to a negligible value of $ERR_{FOV} = 0.02\%$.

The relative error in the calibration blackbody can be calculated from its temperature stability. According to the data sheet that is better than 2K at $T_c = 1273K$. This yield an averaged relative error - $<\Delta P(T_c, \lambda)/P(T_c, \lambda)>$ - of 0.48% in the 3-5μm and 0.26% in the 8-12μm.

The relative error in the calibration signal was calculated from one calibration that was done in the evening of January 11, 1999. The averaged relative error - $<\Delta V_c(\lambda)/V_c(\lambda)>$ - was calculated as 0.7% in the 3-5μm and 2.5% in the 8-12μm.

The relative error in the measured signal $V_m(\theta, \lambda)$ was calculated from the measurement file that was done at zenith angle of 86° in the evening of January 11, 1999. Since each measured signal $V_m(\theta, \lambda)$ is average of fifty spectral scans (CVF scans), we calculated, at discrete wavelengths, the average values and the standard deviations of $V_m(\theta, \lambda)$. The averaged relative error - $<\Delta V_m(\lambda)/V_m(\lambda)>$ - was calculated as 0.8% in the 3-5μm and 1.7% in the 8-12μm.

From this analysis we can conclude that the averaged relative error of the measured transmittance - $<\Delta\tau_m(\theta, \lambda)/\tau_m(\theta, \lambda)>$ - is equal to 2.0% in the 3-5μm and 4.5% in the 8-12μm. The rather large error in the 8-12μm spectral region is mainly due to the low sensitivity of the "sandwich" detector, where the InSb detector covers the CMT detector.

The averaged relative error of the calculated transmittance - $<\Delta\tau(\theta, \lambda)/\tau(\theta, \lambda)>$ - was calculated from the sensitivity of the calculation to different input parameters. The only input parameter that can have rather large error is the visibility that was measured by us. We assumed that a relative error of 10% is a reasonable approximation. This means that a value of VIS=35km means the visibility can be between 31.5km and 38.5km. This may be a little pessimistic approach but due to the long optical paths we assume that it is not far from realistic approach. Therefore, we calculated the averaged relative error of all our predicted transmittance values in four spectral regions: 3.5-4.0μm, 4.5-5.0μm, 8.0-9.0μm and 10.0-12.5μm. The results for the morning measurements of the January 12, 1999 are presented in Table 1 and in Figures 28-31.

As can be expected close to the horizon (zenith angles close to 90 degrees) the relative error is about 5% and it decreases as the elevation angle increases and at longer wavelengths. The maximal absolute transmittance error at zenith angles between 89° and 87° can be calculated from Table 5 and Figures 24-27 as ~1.0 % in the 3-5μm and ~0.7% in the 8-12μm.

	The Relative Error in the Calculated Transmittance (in %)				
Zenith Angle	10% Visibility Error	3.5-4.1μm	4.5-5.0μm	8.0-9.0μm	10.0-12.5μm
80	+	+0.7	+0.6	+0.6	+0.5
	-	-0.9	-0.8	-0.7	-0.6
81	+	+0.8	+0.7	+0.7	+0.6
	-	-1.0	-0.8	-0.8	-0.7
82	+	+0.9	+0.8	+0.8	+0.7
	-	-1.1	-1.0	-0.9	-0.8
83	+	+1.0	+0.9	+0.9	+0.7
	-	-1.2	-1.1	-1.0	-0.9
84	+	+1.2	+1.0	+1.0	+0.9
	-	-1.4	-1.2	-1.2	-1.0
85	+	+1.4	+1.2	+1.2	+1.0
	-	-1.7	-1.5	-1.4	-1.2
86	+	+1.7	+1.5	+1.5	+1.3
	-	-2.1	-1.8	-1.8	-1.5
87	+	+2.2	+1.9	+1.9	+1.6
	-	-2.3	-2.4	-2.3	-2.0
88	+	+3.2	+2.8	+2.7	+2.3
	-	-3.8	-3.3	-3.2	-2.8
89	+	+5.3	+3.7	+4.4	+3.8
	-	-6.1	-6.1	-5.2	-4.5

Table 5: The relative error in the predicted transmittance (in %) for 10% relative error in the measured visibility

6. CONCLUSIONS

1) The results obtained show good agreement with the prediction of the MODTRAN3.7 code at low elevation angles (close to the horizon). The disagreement with the prediction at higher elevations was due to the heating of the detector - an effect that was discovered, unfortunately, only after the end of the field tests when the results were compared to the MODTRAN code.
2) The averaged relative error of the measured transmittance - $<\Delta\tau_m(\theta, \lambda)/\tau_m(\theta, \lambda)>$ - was found to be 2.0% in the 3-5μm and 4.5% in the 8-12μm.
3) The maximal error of the predicted transmittance is caused by the inherent error in the visibility that is a dominant and important parameter of the MODTRAN3.7 code, especially at low elevation angles. The value of 10% was chosen as rather realistic approximation of this error. Correspondingly, The maximum relative error in the calculated transmittance values - $<\Delta\tau(\theta, \lambda)/\tau(\theta, \lambda)>$ - was found to be as ~1.0 % in the 3-5μm and ~0.7% in the 8-12μm.
4) We found that at low elevation angles there was a good absolute and spectral matching between the experimental results and the MODTRAN3.7 prediction in the 2.8-5.4μm spectral region.
5) We found that at low elevation angles there was rather good absolute and spectral matching between the experimental results and the MODTRAN3.7 prediction in the 8-12μm spectral region.
6) The spectral discrepancy at 8.5μm between the predicted results and the experimental results (see Figure 32) can be attributed either to the modeling of the altitude profile or to the absorption coefficients of N_2O (or to less extent to those of O_3 or CO_2 or the aerosol absorption).
7) The spectral discrepancy between the predicted and the experimental results in the 3.8-4.0 spectral region (see Figure 33) can be attributed, as well, either to the modeling of the altitude profile or to the absorption coefficients of N_2O but hardly to those of CO_2.
8) The fact that the MODTRAN 3.7 prediction at wavelengths below 3.5μm is somewhat lower than the measured values (see figure 23a) can be attributed to the modeling of the water continuum.

9) We found that the rural aerosol model can give very good description for the aerosol attenuation in the desert regions of Israel (Negev). It should be noted that during the field test there was almost no wind that determines the visibility in the desert aerosol model. Since without wind the visibility values of this model can be unrealistic and the fact that it is known that the desert aerosol model has some problems in it left us with the rural aerosol model.

10) We propose to repeat these field tests in south part of Israel in the summer when the air temperatures are high in the evenings hours as well as in the early morning hours. These test conditions can validate the effect of the air temperature on the water continuum in the 8-12μm spectral region.

11) Since the SR-5000 is a 14bit system it will be possible to operate it in the future tests with a 1:10 attenuator and still obtain high S/N ratios in the calibration signal. This is what we propose to do in the future field tests because (the heating problem aside) the SR-5000 spectroradiometer seems to be ideal instrument for these measurements.

12) In these proposed tests the measured transmittance will be compared to the predictions also in the 1.3-2.5μm spectral region - a region that was (unfortunately) saturated in the present tests.

13) We also want to build a small spectroradiometer that will measure the transmittance in the center of the photopic region (about λ=0.55μm) in these proposed tests, in order to validate the visibility values that will be obtained by the visibility meter. This will remove the large error in the visibility values that are measured in-situ compared to their value as averaged over near-horizontal long optical paths.

7. ACKNOWLEDGEMENT

We would like to thank the European Office of Aerospace Research and Development (EOARD) for its funding of this research.

References

1. A. J. Ratkowski, G. P. Anderson, J. H. Chetwynd, R. M. Nadile, A. D. Devir and T. D. Conley, "A comparison of atmospheric transmittance measurements in the 3-5μm and 8-12μm spectral regions with MODTRAN: considerations for long near-horizontal path geometries", Proc SPIE, Vol. 3219, pp. 2-10, 1998.
2. W. M. Gutman, W. A. Peterson, B. K. Matise, J. L. Manning and R. E. Soulon, "Atmospheric transmittance spectroscopy using the sun as the source", Appl. Optics, 29, pp.3213-3217, 1990.
3. D. Kryskowski and G. H. Suits, "Natural Sources" Ch. 3 in "Sources of Radiation" Vol. 1 of "The Infrared and Electro-Optical Systems Handbook", ERIM/SPIE 1993.

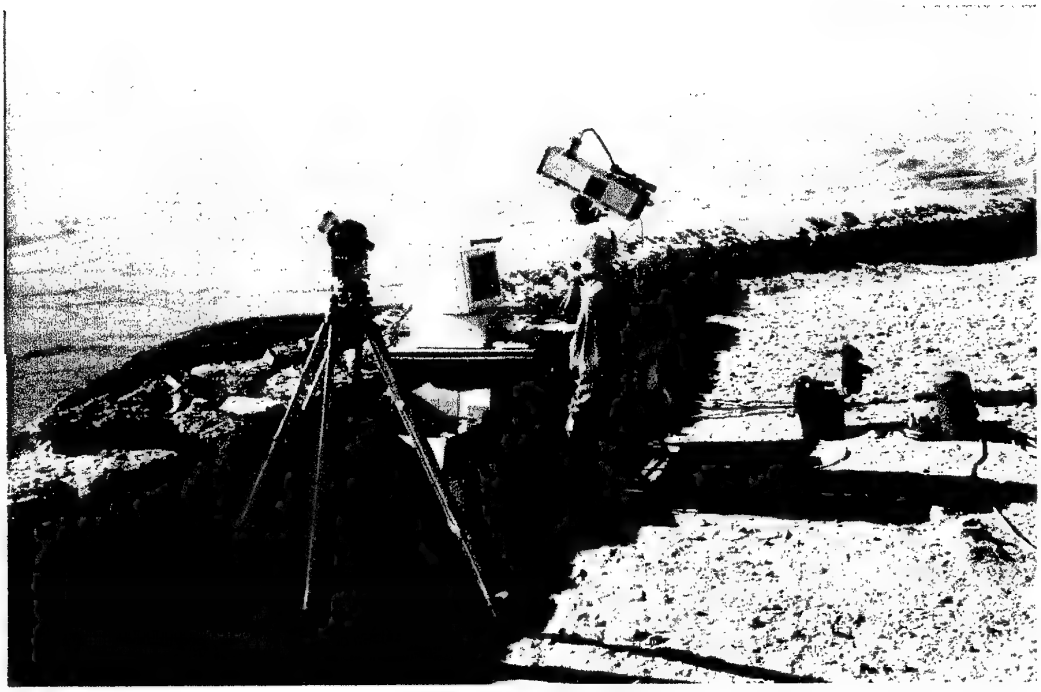

Figure 1: The experimental set-up in Mitzpe' Ramon in the Negev

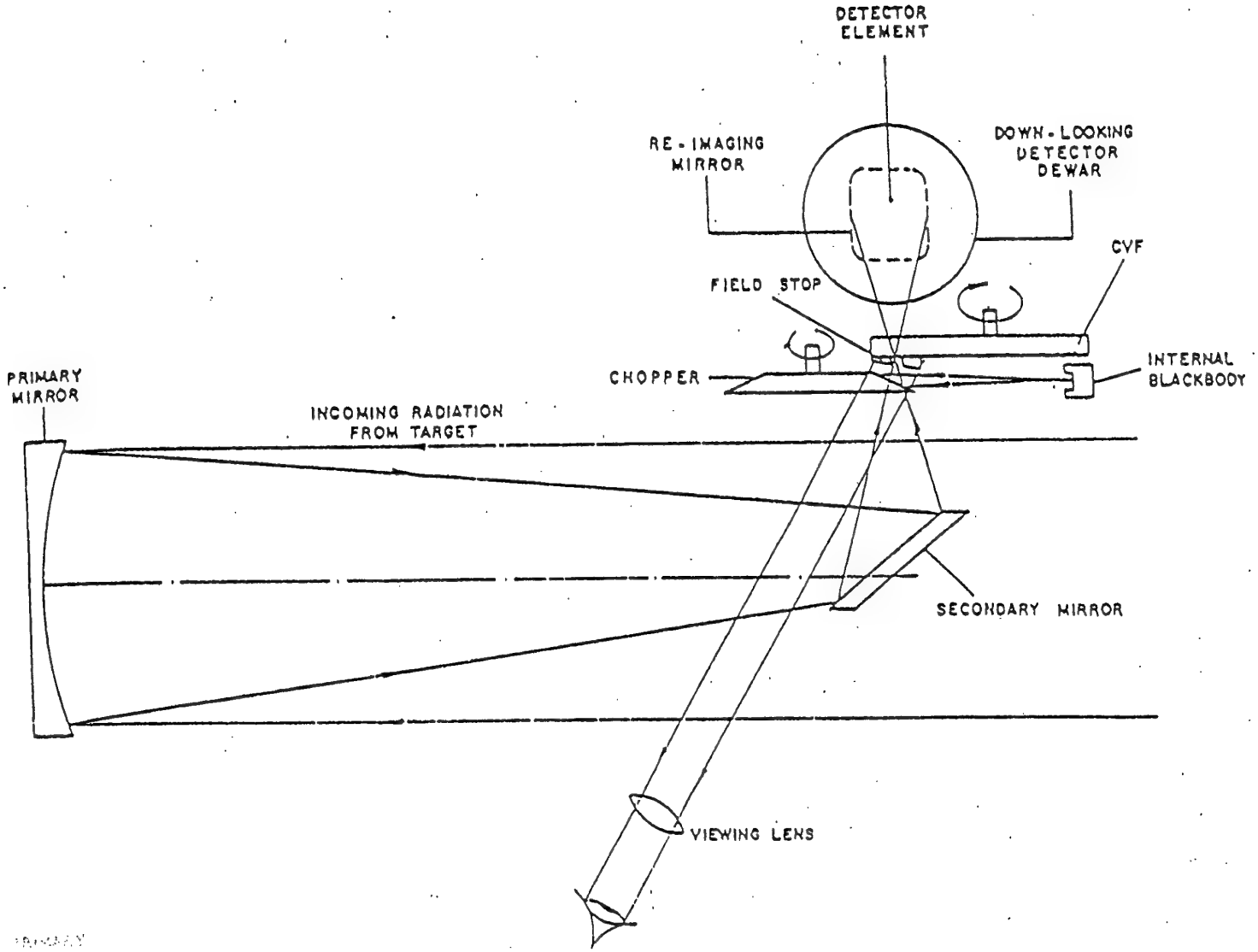

Figure 2: The optical layout of the SR-5000 spectroradiometer.

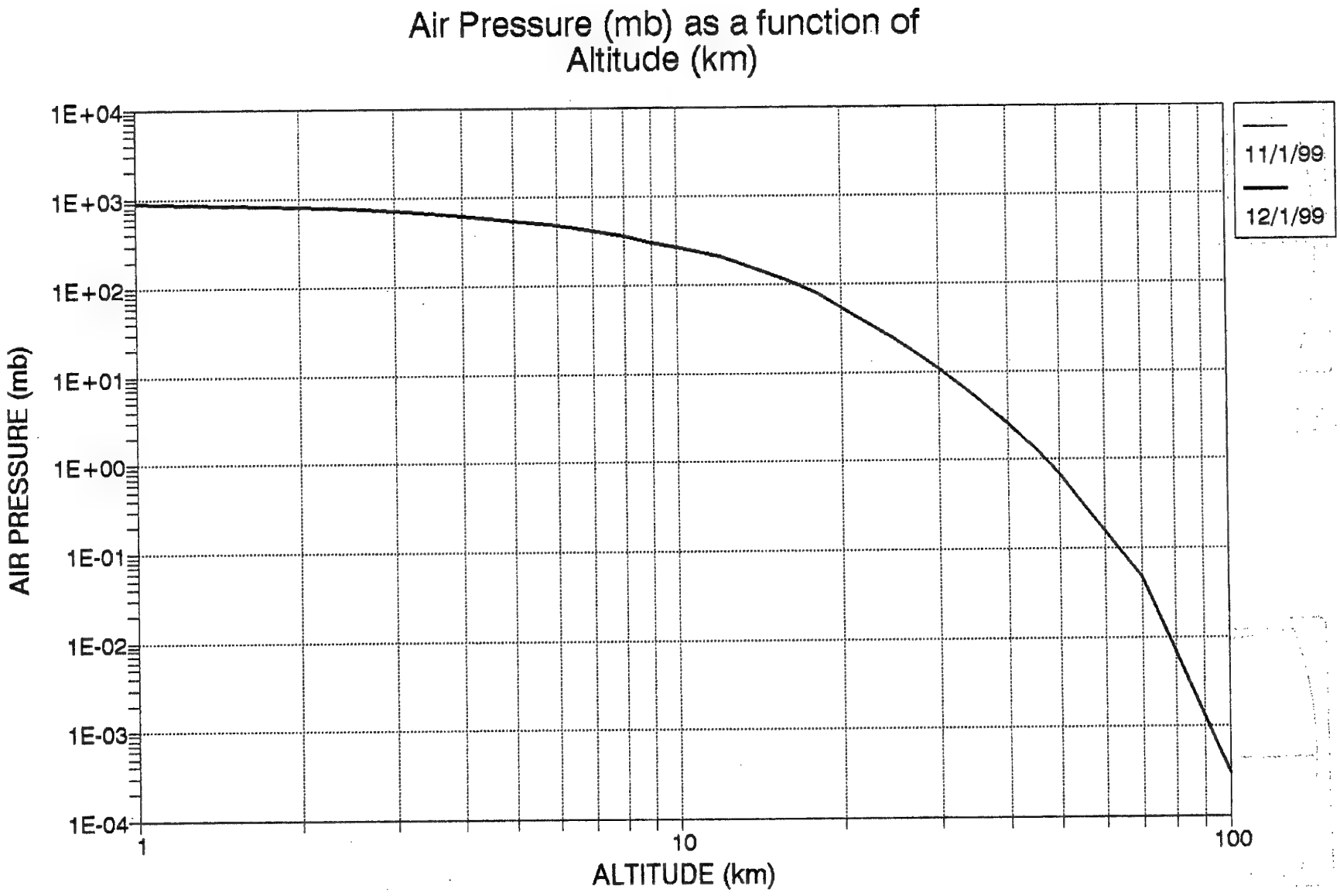

Figure 3: The profile of the air pressure P(mb) as measured by the radiosonde in January 11th and 12th, 1999.

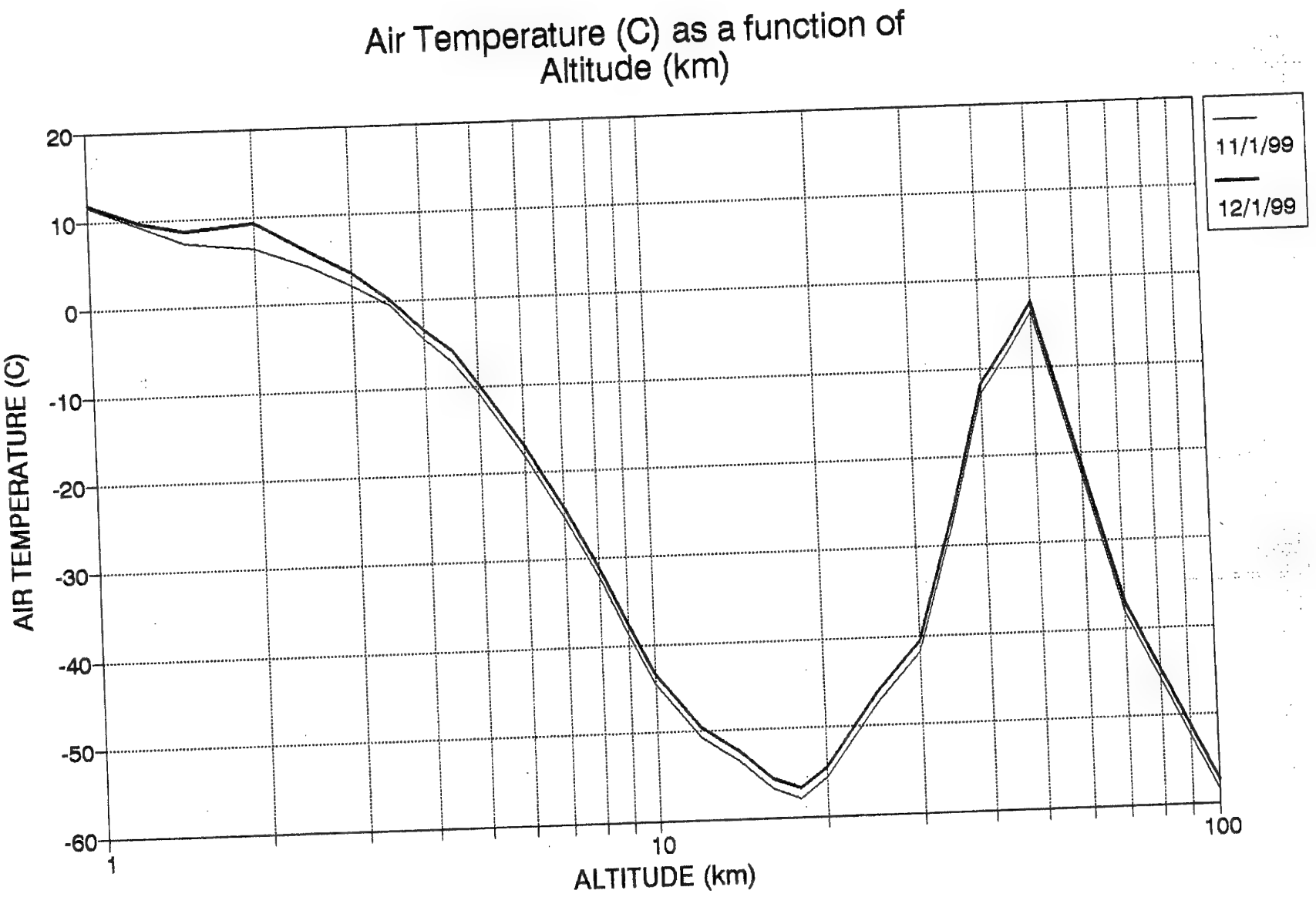

Figure 4: The profile of the air temperature T(K) as measured by the radiosonde in January 11th and 12th, 1999.

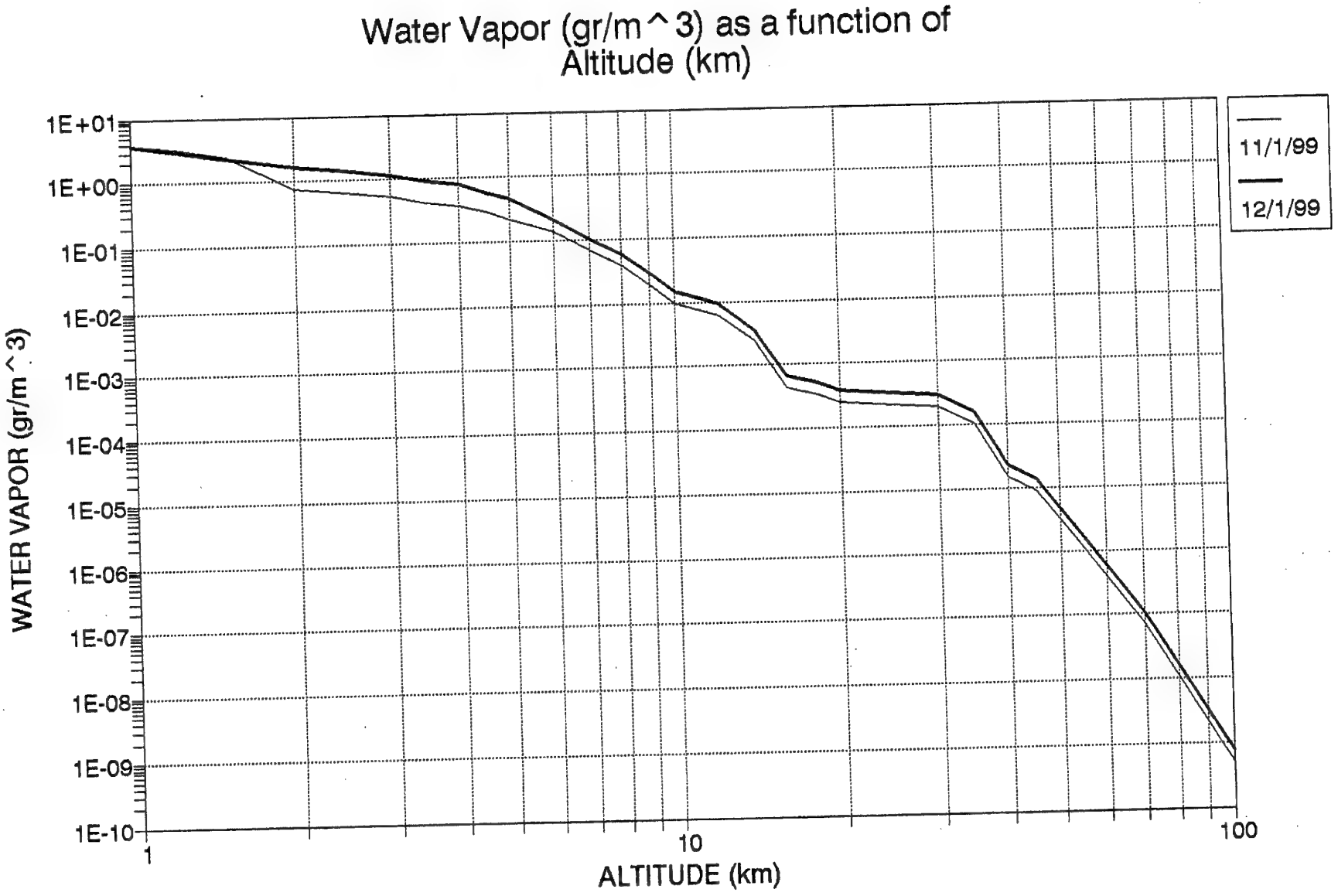

Figure 5: The profile of the water vapour density ρ_{water} (gr/m^3) as measured by the radiosonde in January 11th and 12th, 1999.

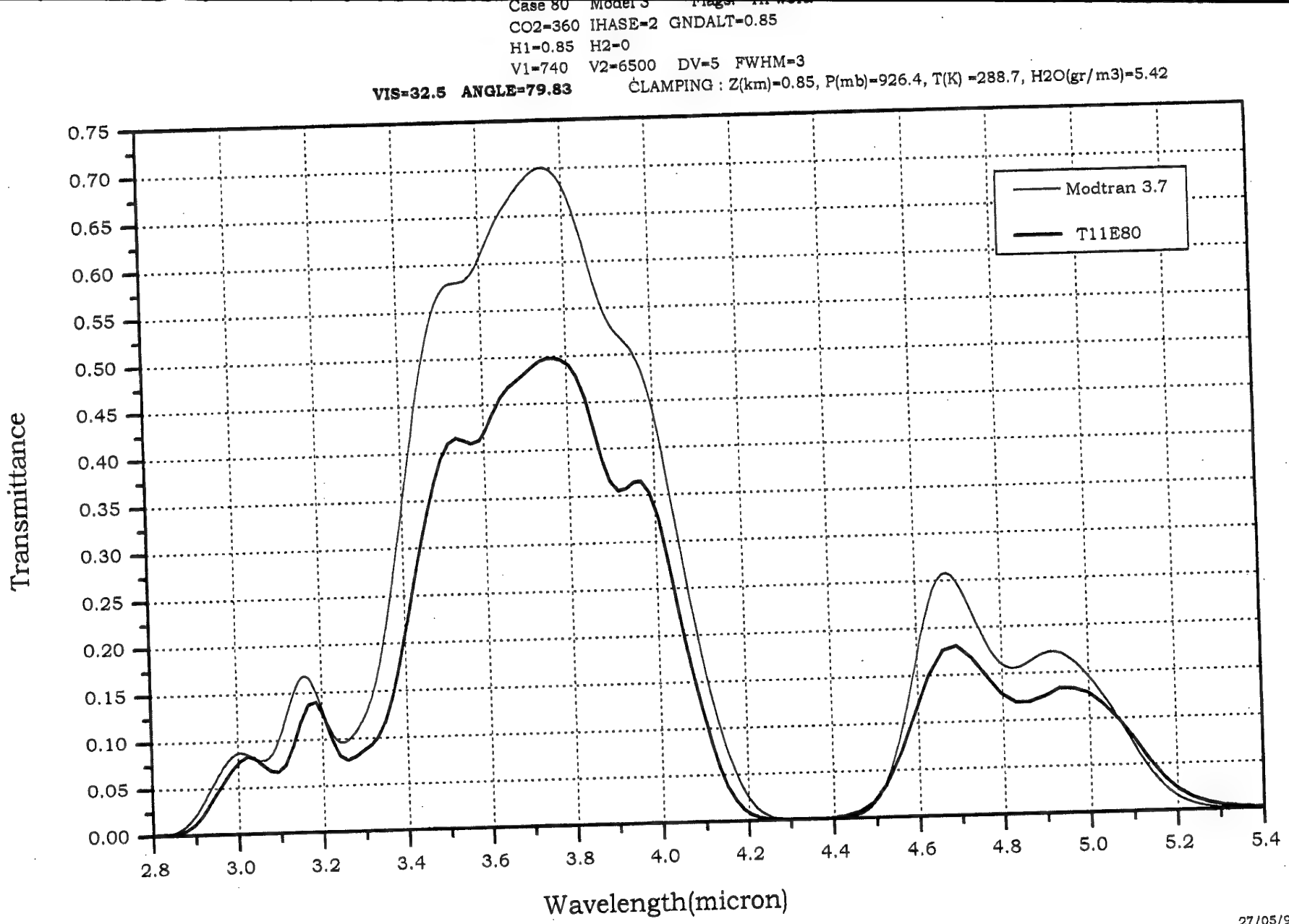

Figure 6a: The experimental results in the 2.8-5.4μm spectral region for zenith angle 80° compared to the prediction of the MODTRAN 3.7 code

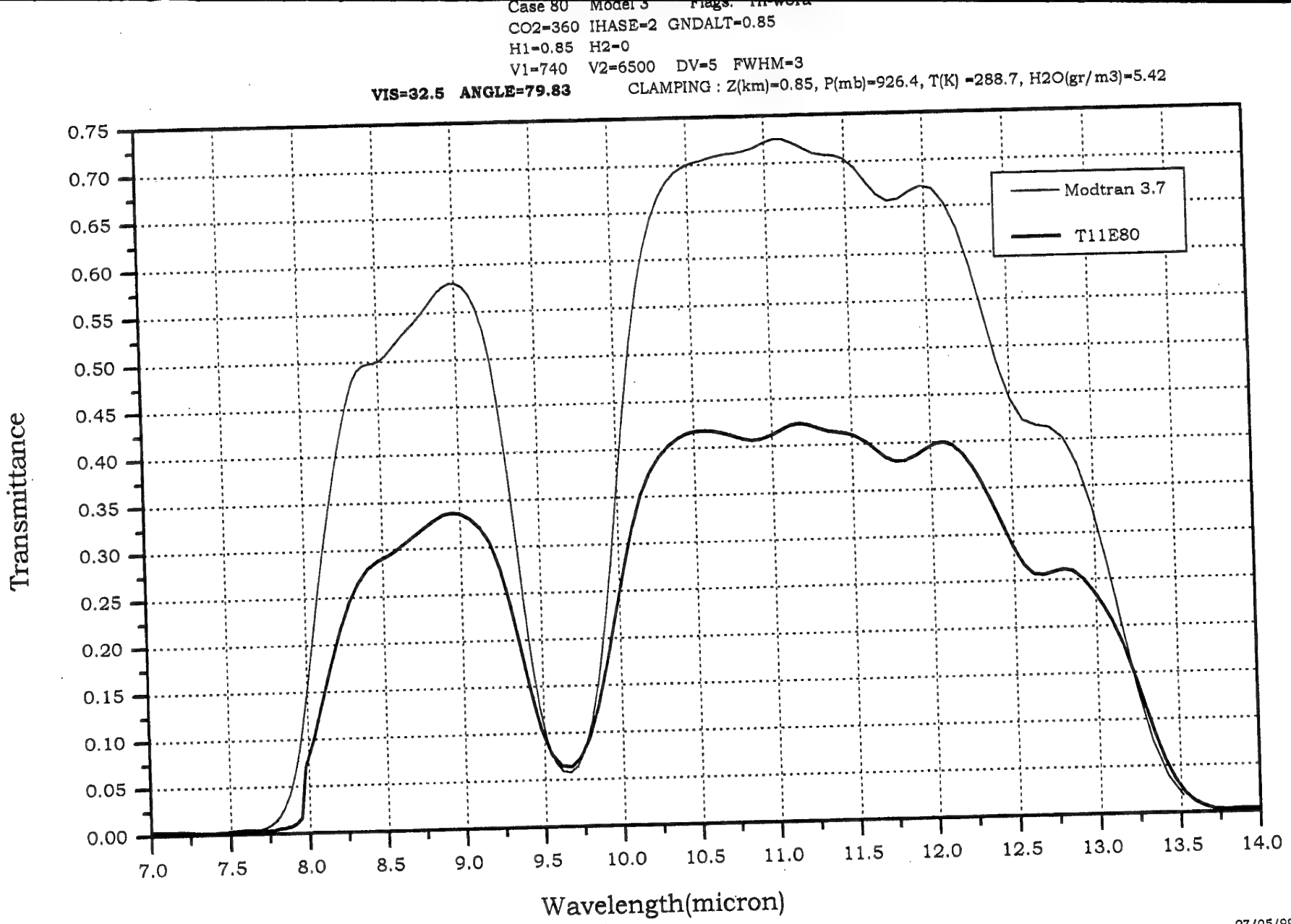

Figure 6b: The experimental results in the 7-14μm spectral region for zenith angle 80° compared to the prediction of the MODTRAN 3.7 code.

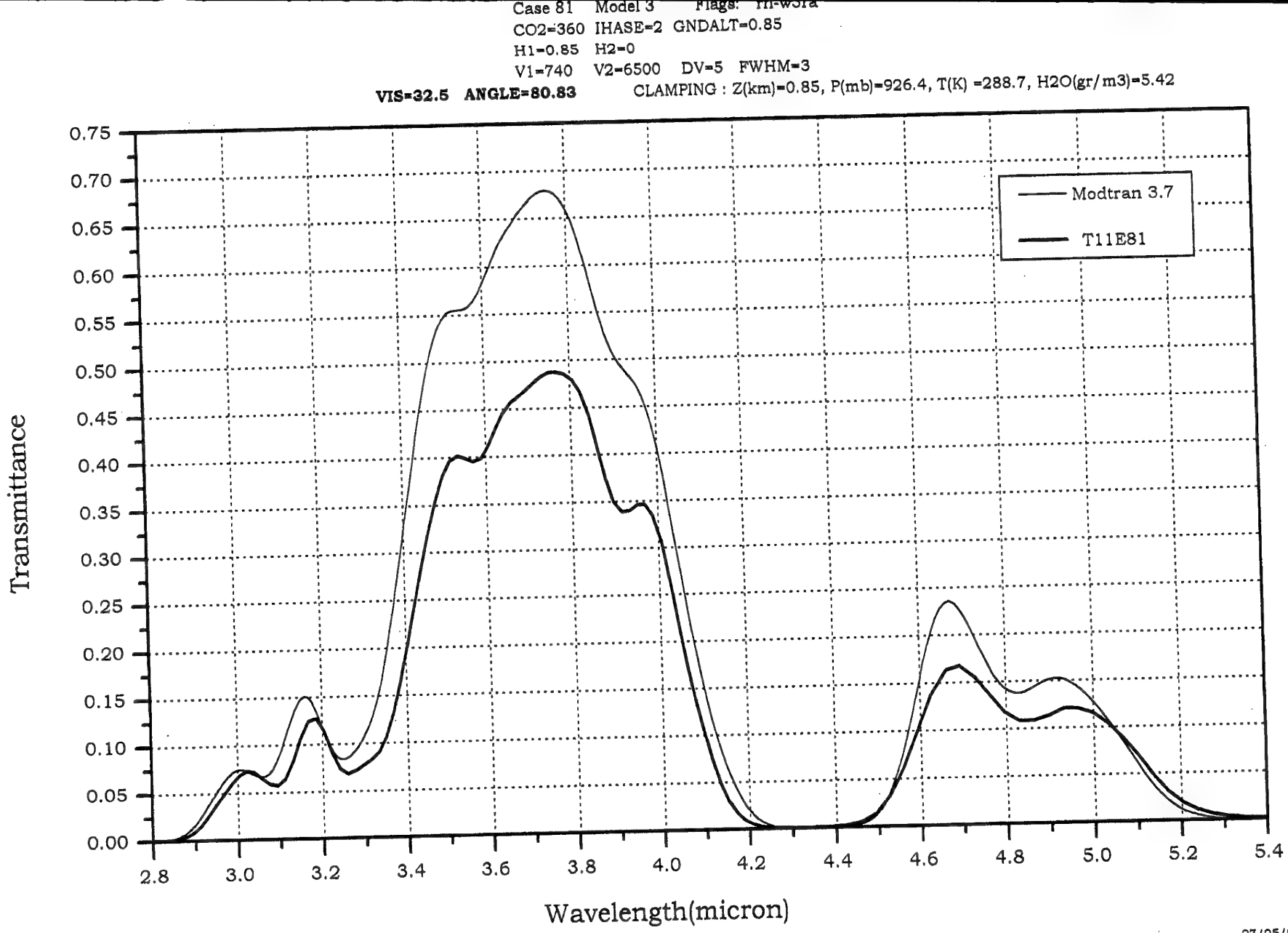

Figure 7a: The experimental results in the 2.8-5.4μm spectral region for zenith angle 81° compared to the prediction of the MODTRAN 3.7 code

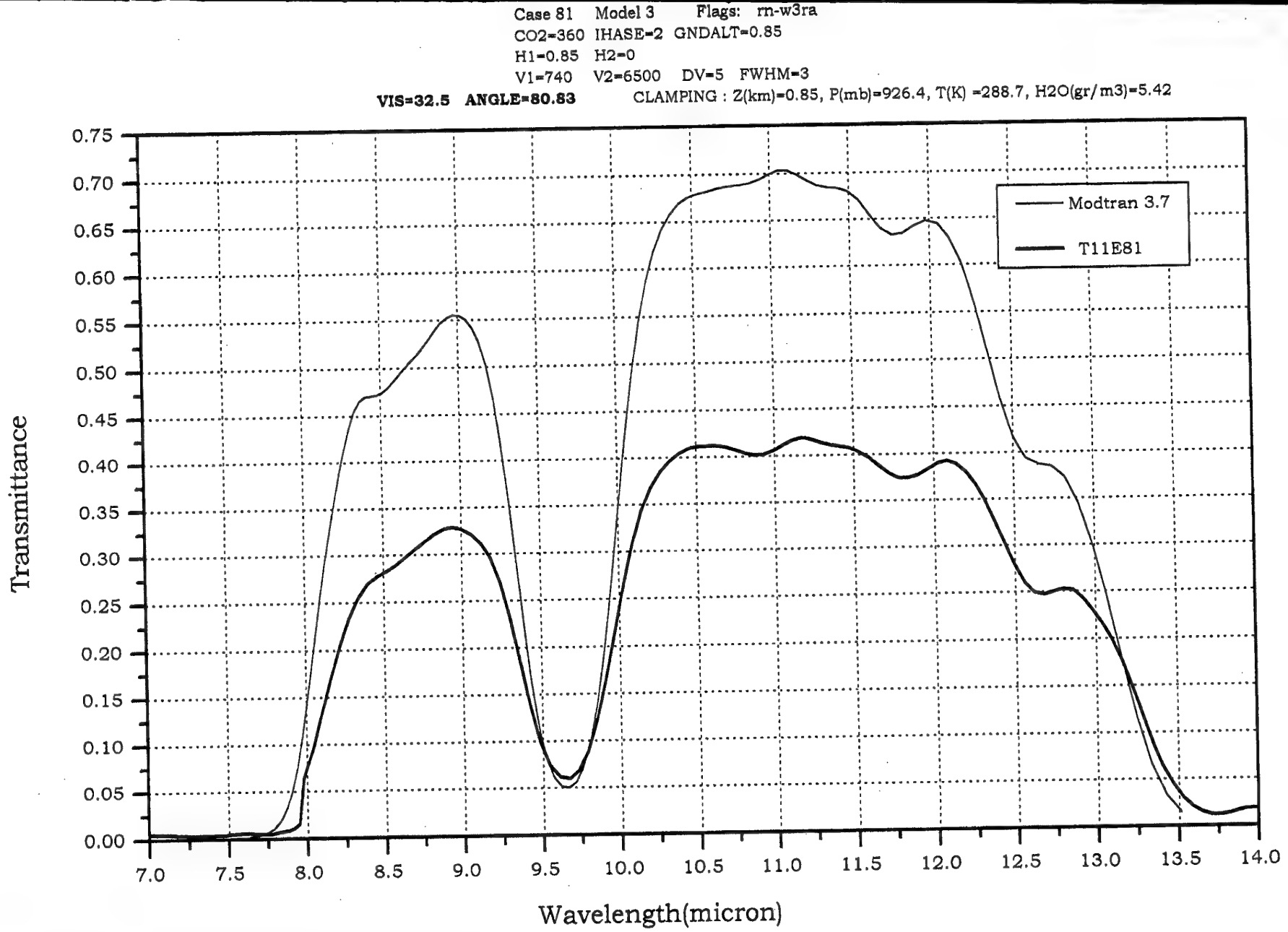

Figure 7b: The experimental results in the 7-14μm spectral region for zenith angle 81° compared to the prediction of the MODTRAN 3.7 code.

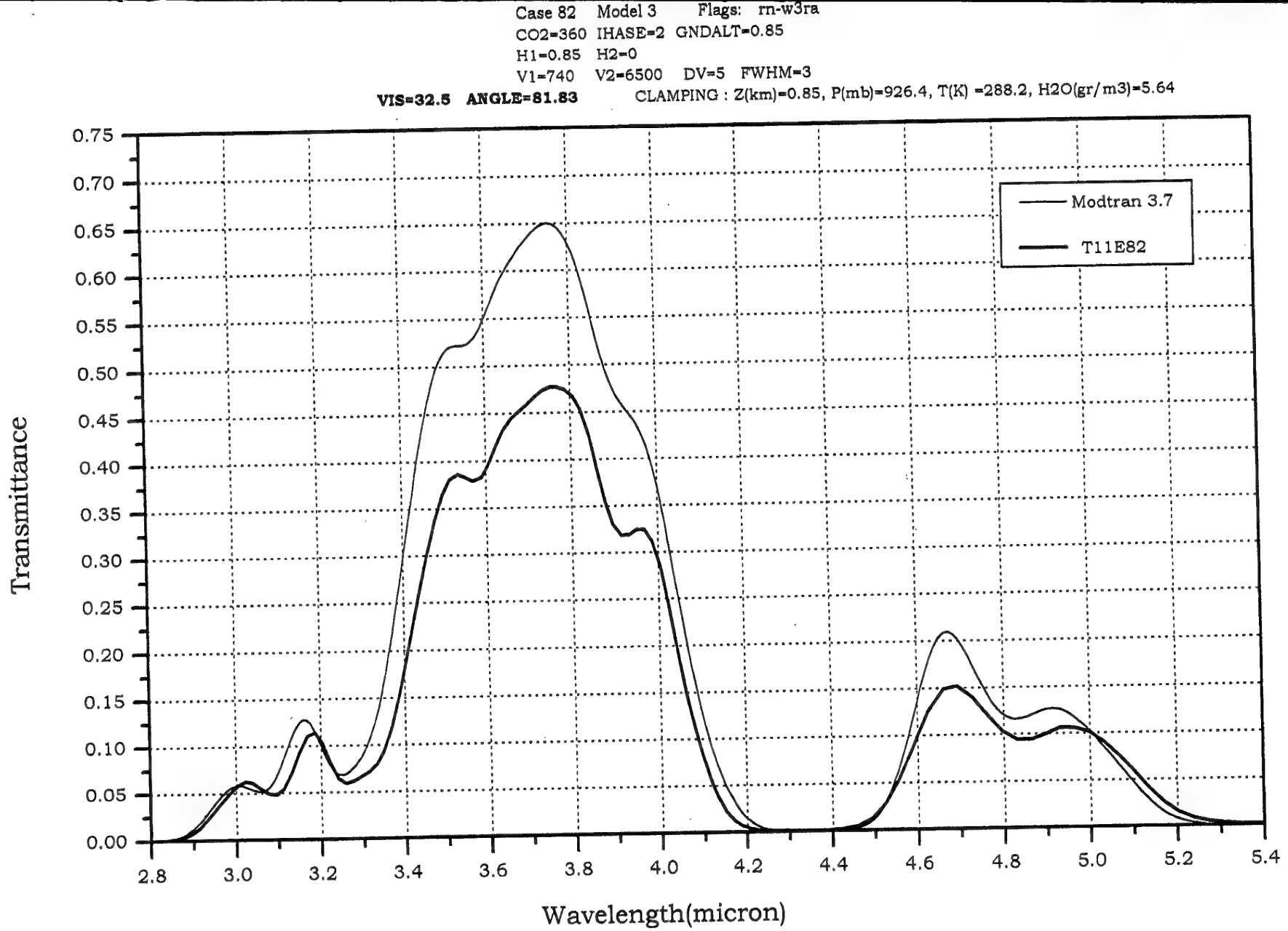

Figure 8a: The experimental results in the 2.8-5.4μm spectral region for zenith angle 82° compared to the prediction of the MODTRAN 3.7 code

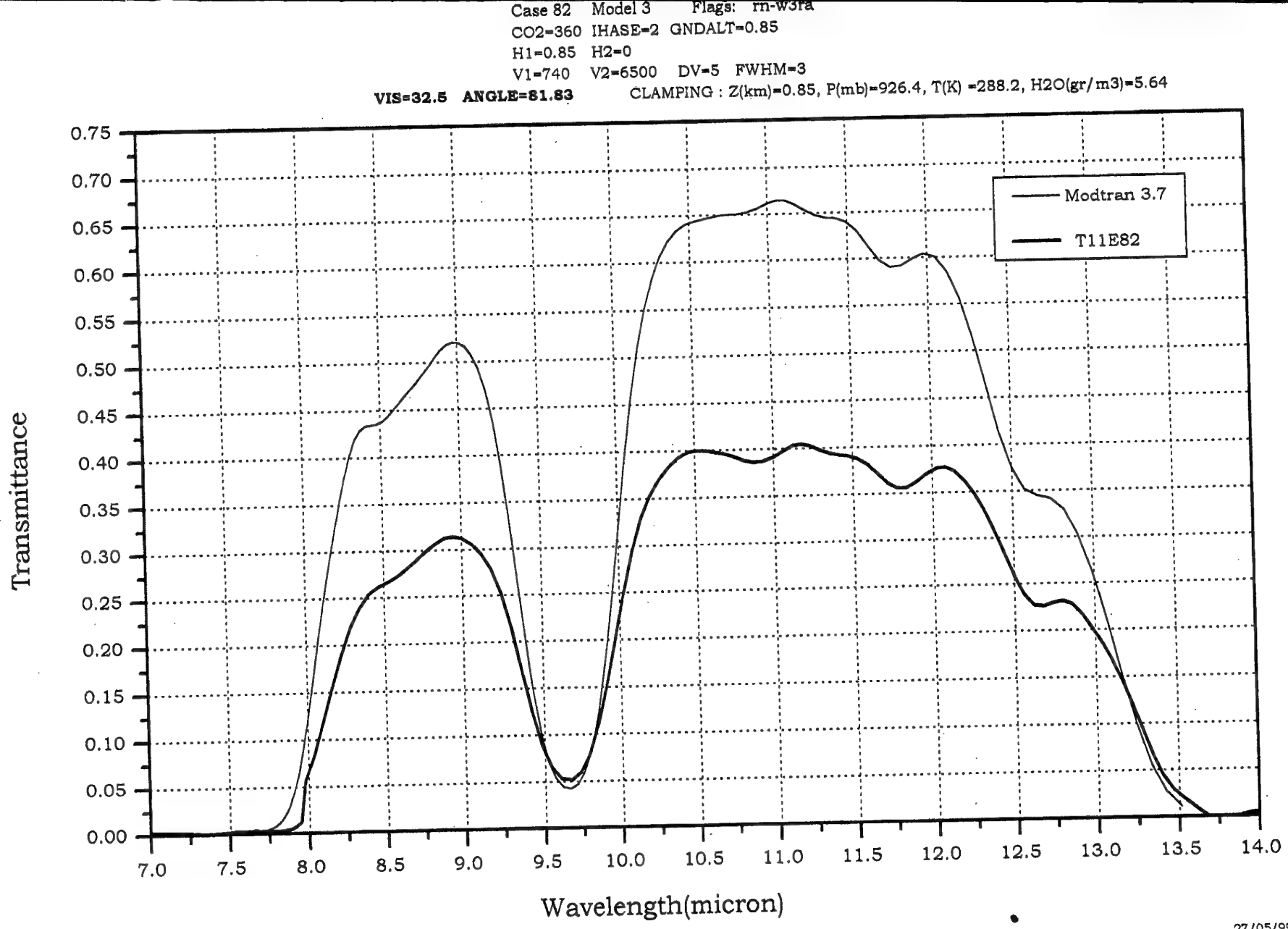

Figure 8b: The experimental results in the 7-14μm spectral region for zenith angle 82° compared to the prediction of the MODTRAN 3.7 code.

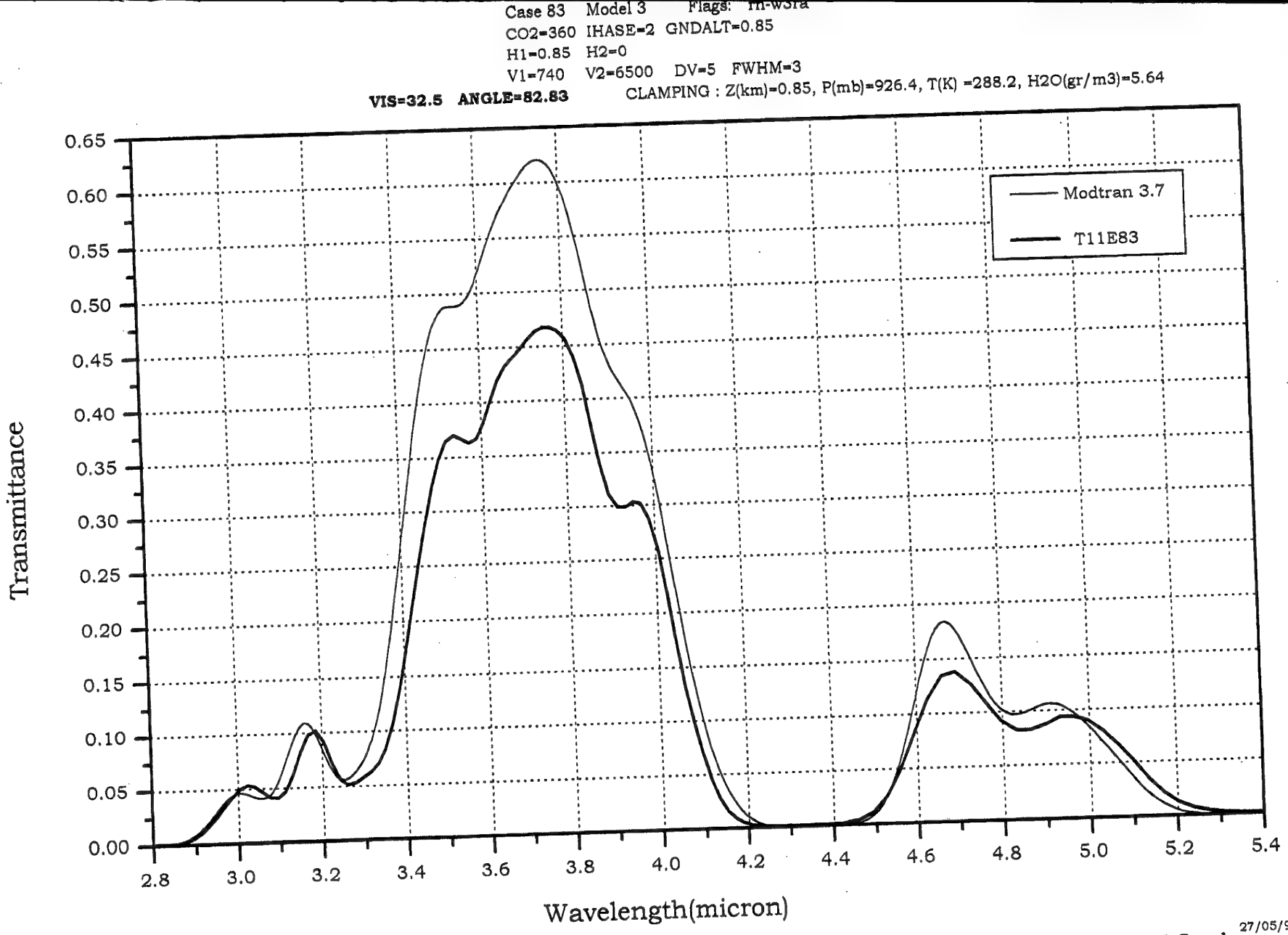

Figure 9a: The experimental results in the 2.8-5.4μm spectral region for zenith angle 83° compared to the prediction of the MODTRAN 3.7 code

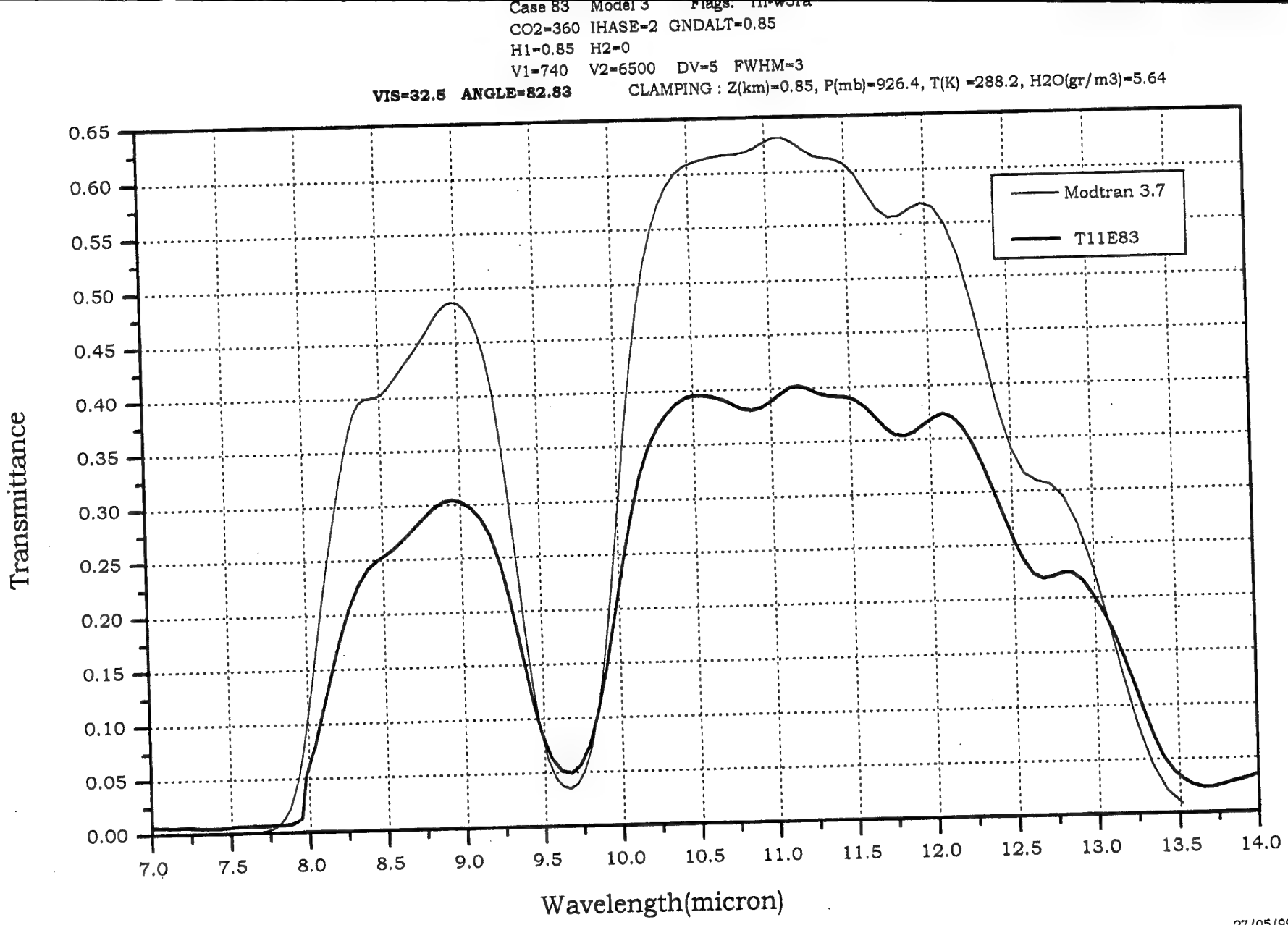

Figure 9b: The experimental results in the 7-14μm spectral region for zenith angle 83° compared to the prediction of the MODTRAN 3.7 code.

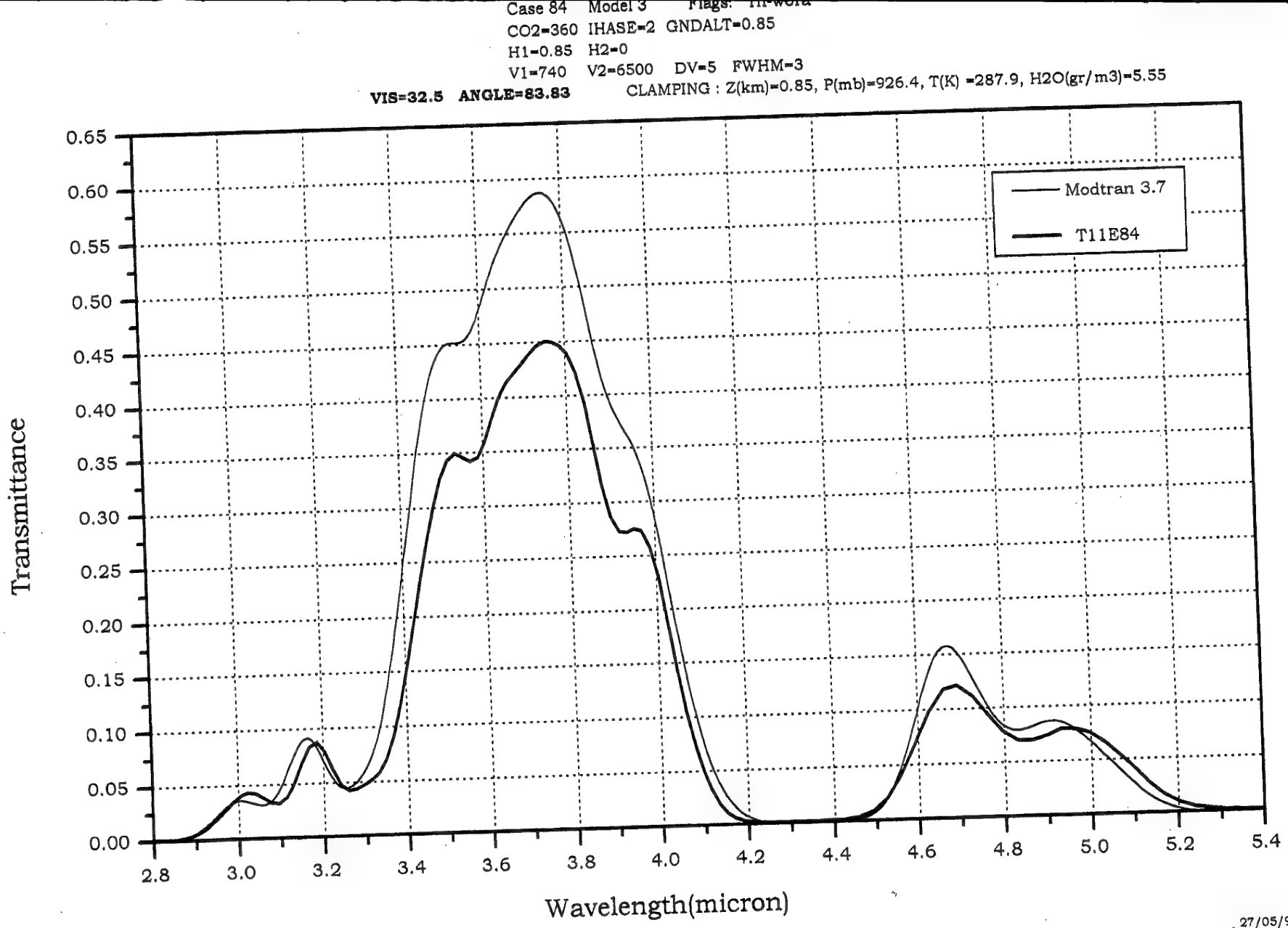

Figure 10a: The experimental results in the 2.8-5.4μm spectral region for zenith angle 84° compared to the prediction of the MODTRAN 3.7 code.

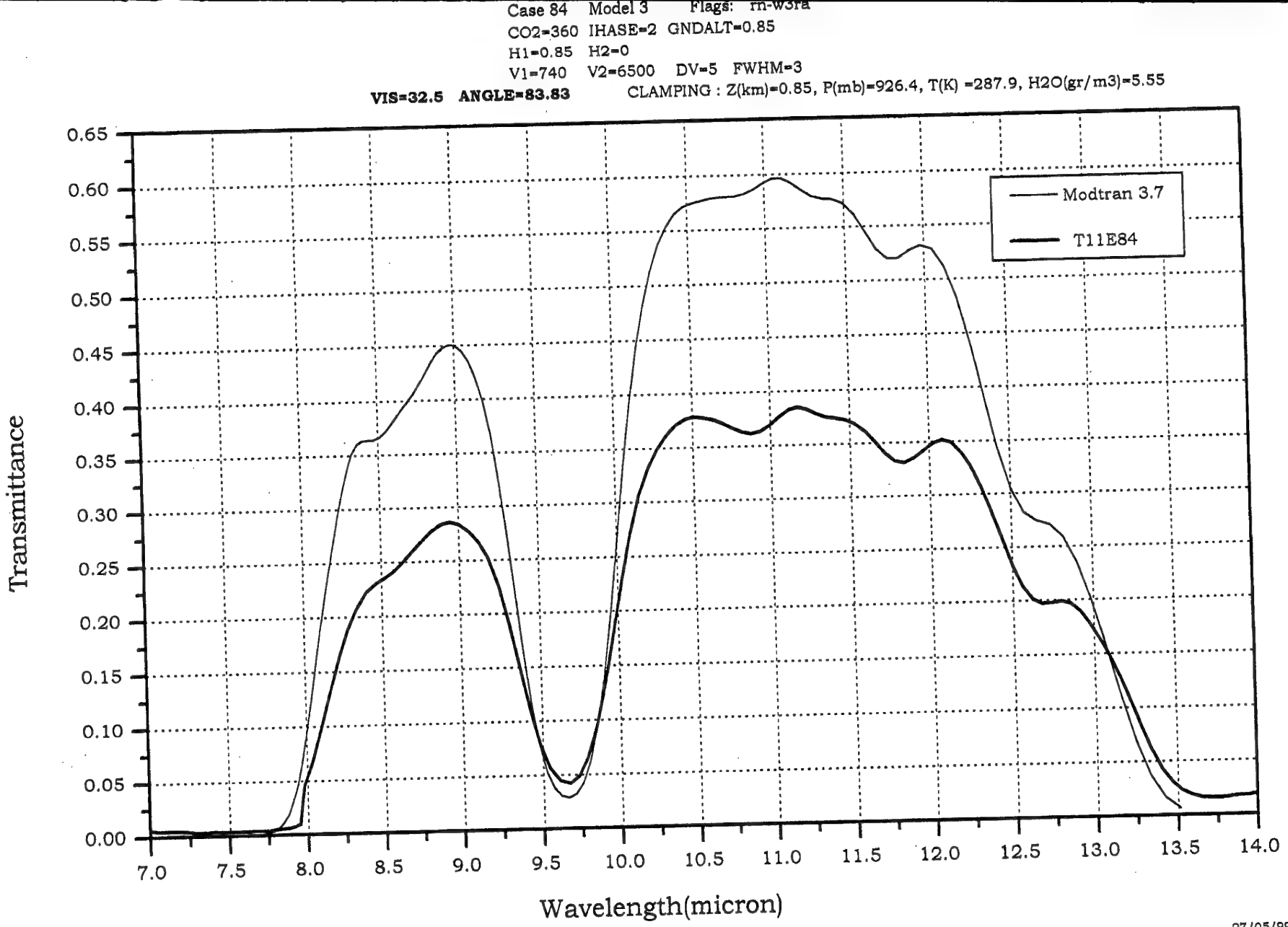

Figure 10b: The experimental results in the 7-14μm spectral region for zenith angle 84° compared to the prediction of the MODTRAN 3.7 code.

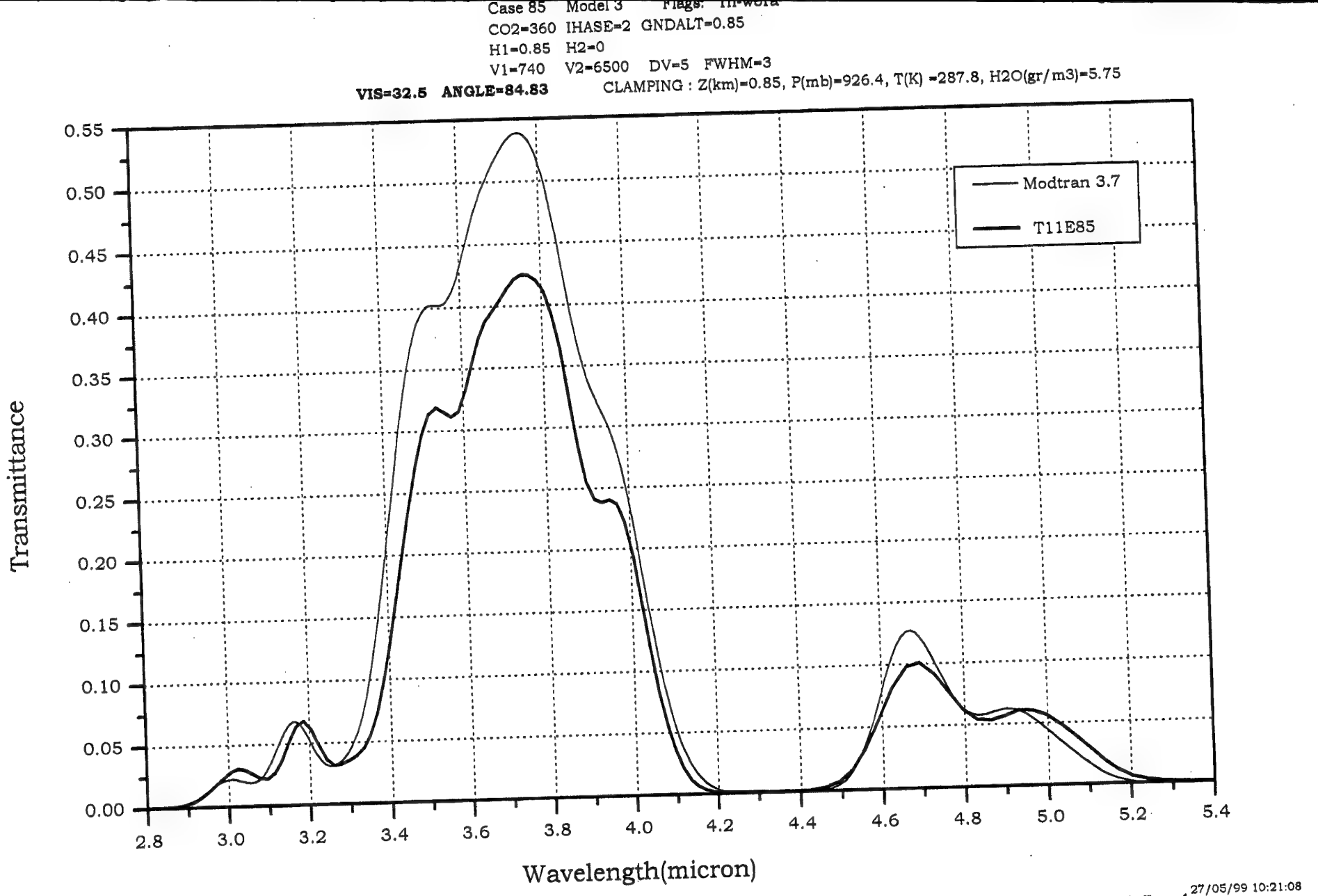

Figure 11a: The experimental results in the 2.8-5.4μm spectral region for zenith angle 85° compared to the prediction of the MODTRAN 3.7 code.

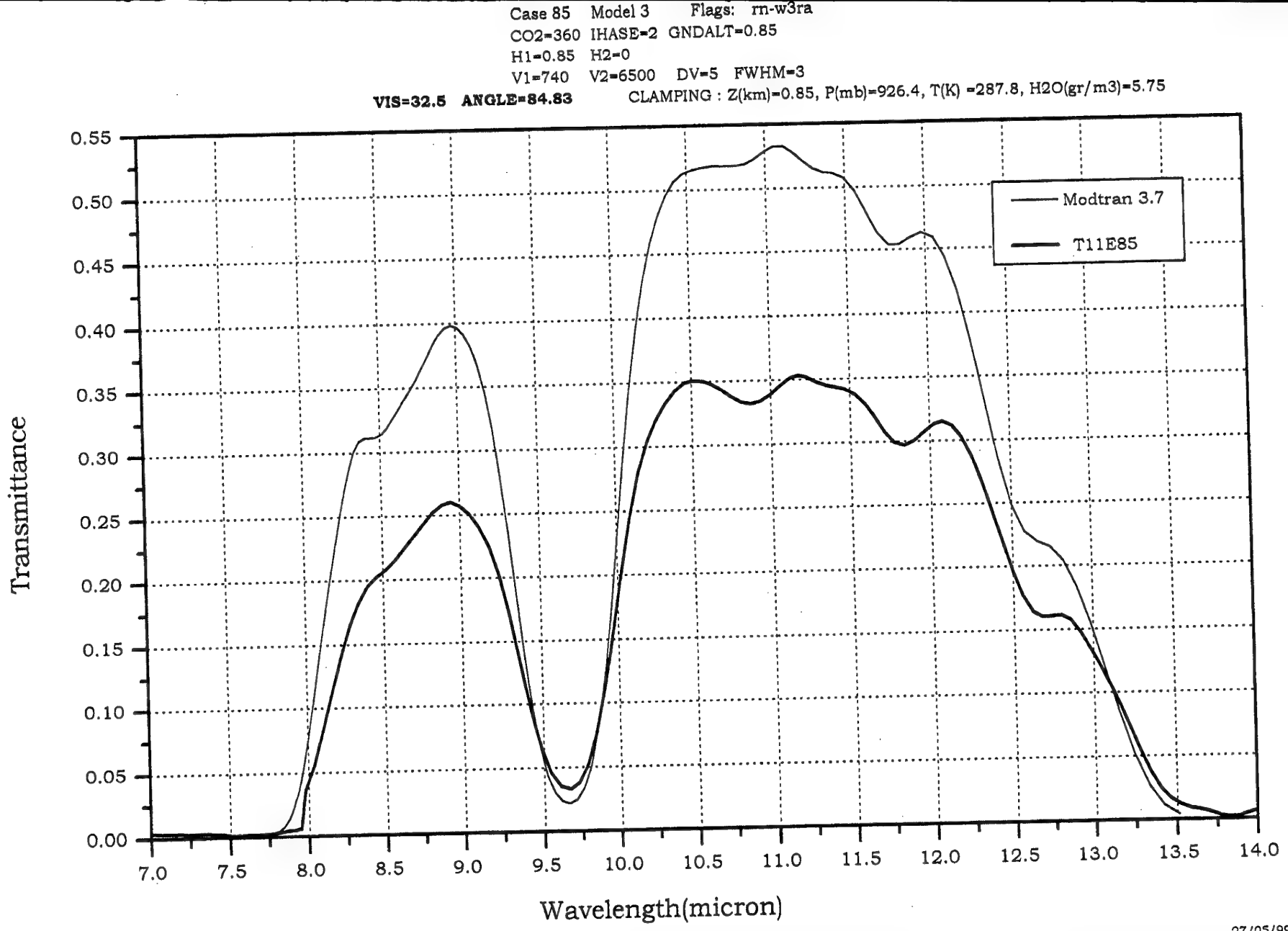

Figure 11b: The experimental results in the 7-14μm spectral region for zenith angle 85° compared to the prediction of the MODTRAN 3.7 code.

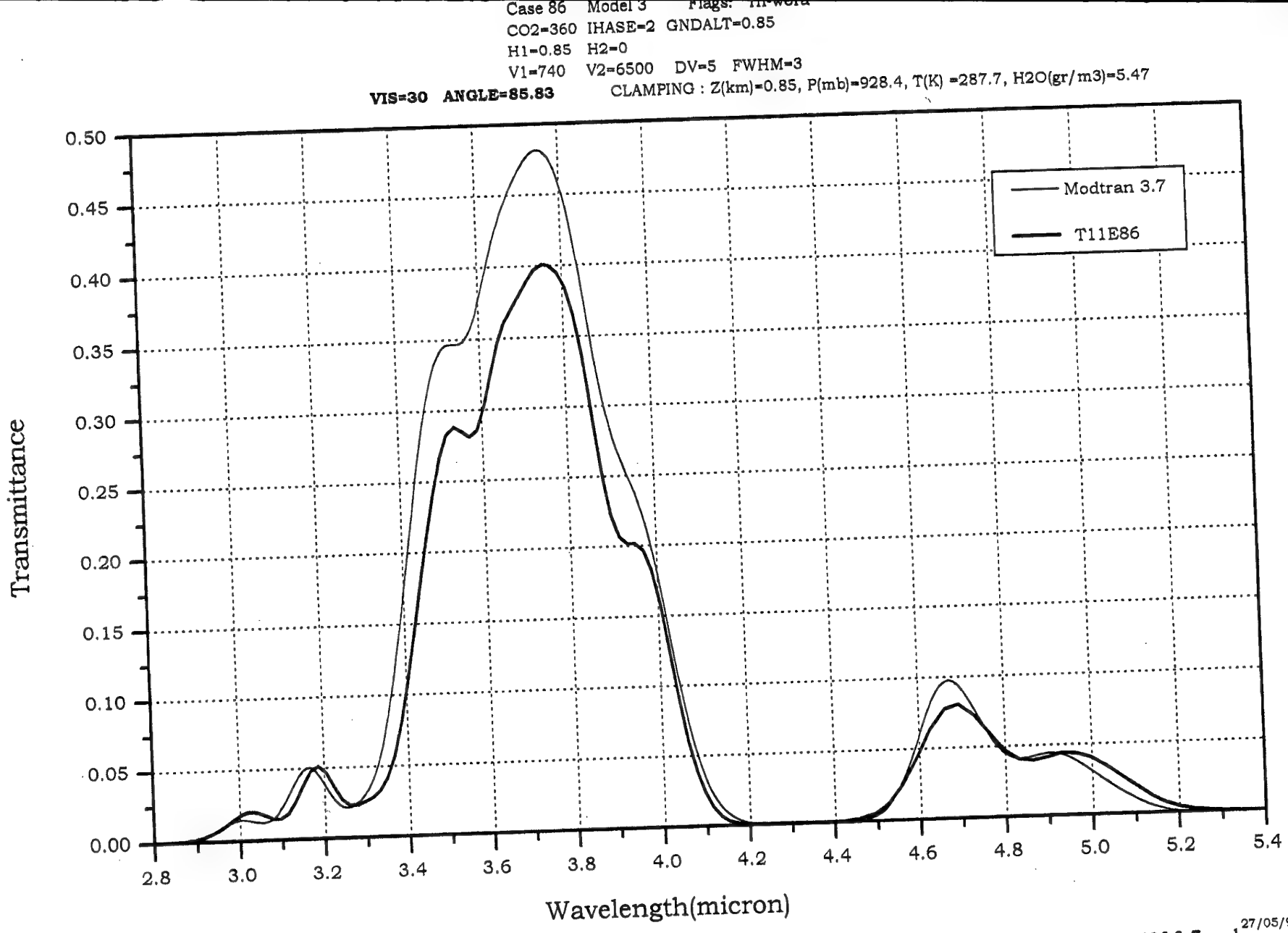

Figure 12a: The experimental results in the 2.8-5.4μm spectral region for zenith angle 86° compared to the prediction of the MODTRAN 3.7 code.

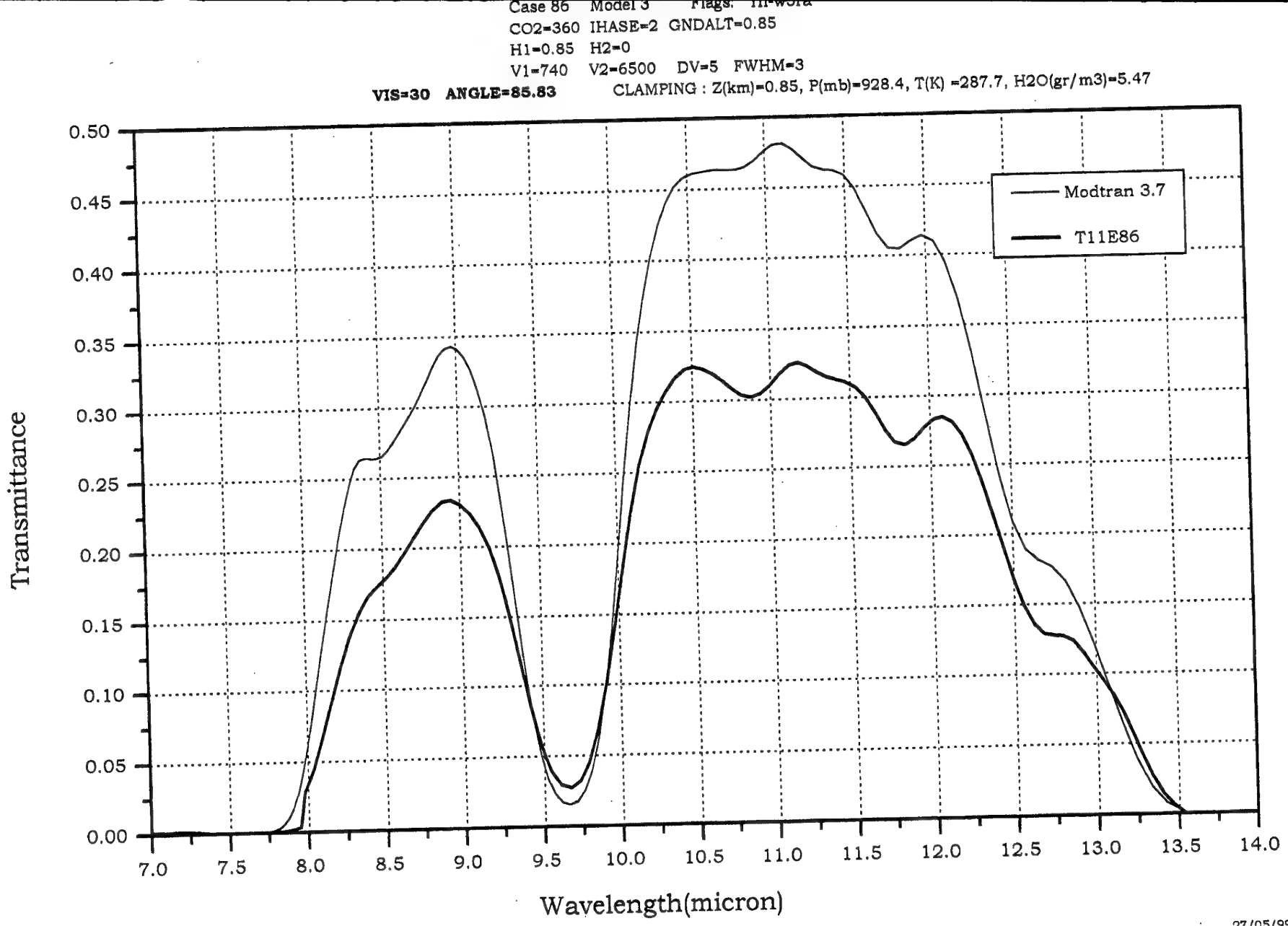

Figure 12b: The experimental results in the 7-14μm spectral region for zenith angle 86° compared to the prediction of the MODTRAN 3.7 code.

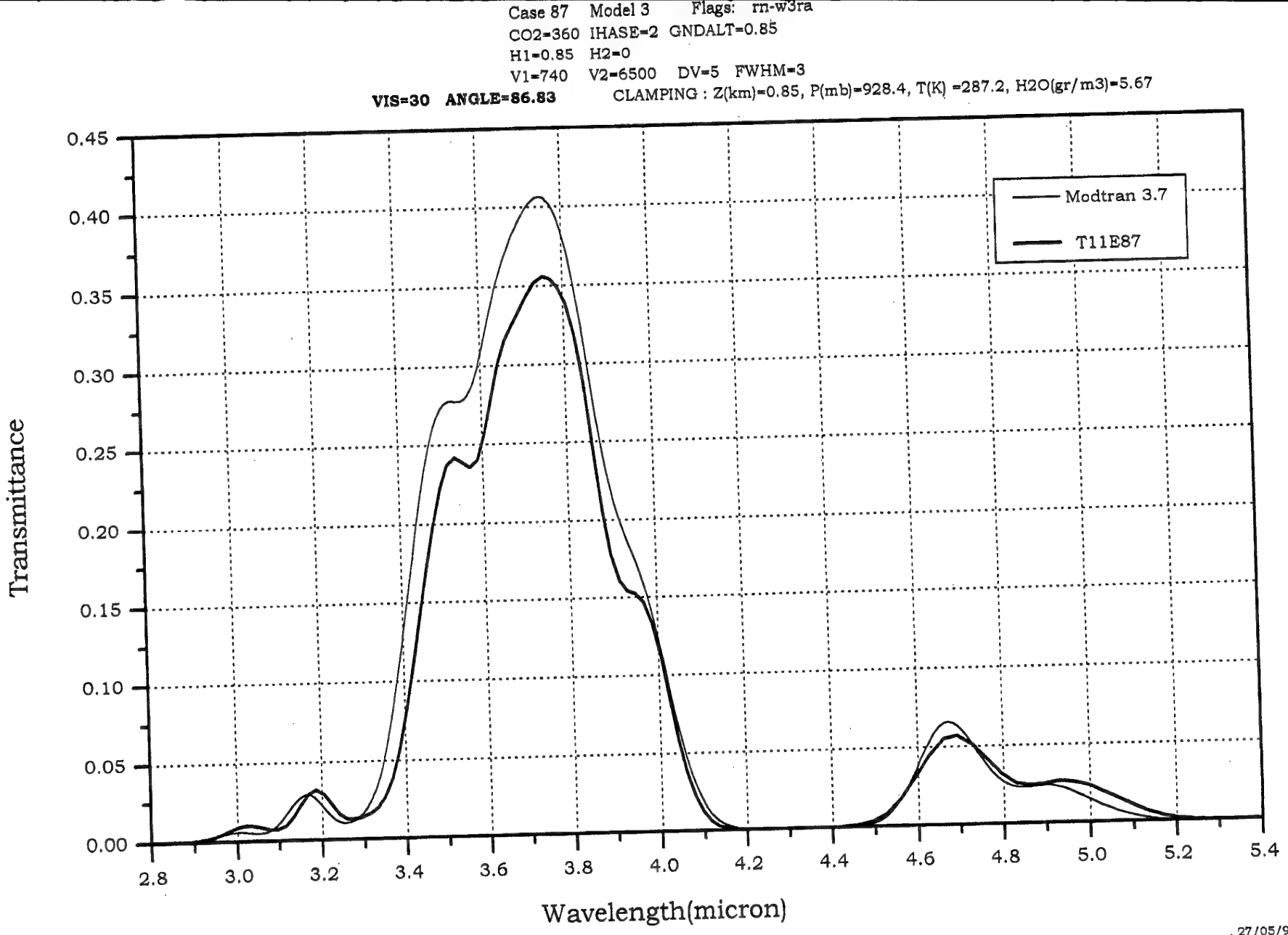

Figure 13a: The experimental results in the 2.8-5.4μm spectral region for zenith angle 87° compared to the prediction of the MODTRAN 3.7 code.

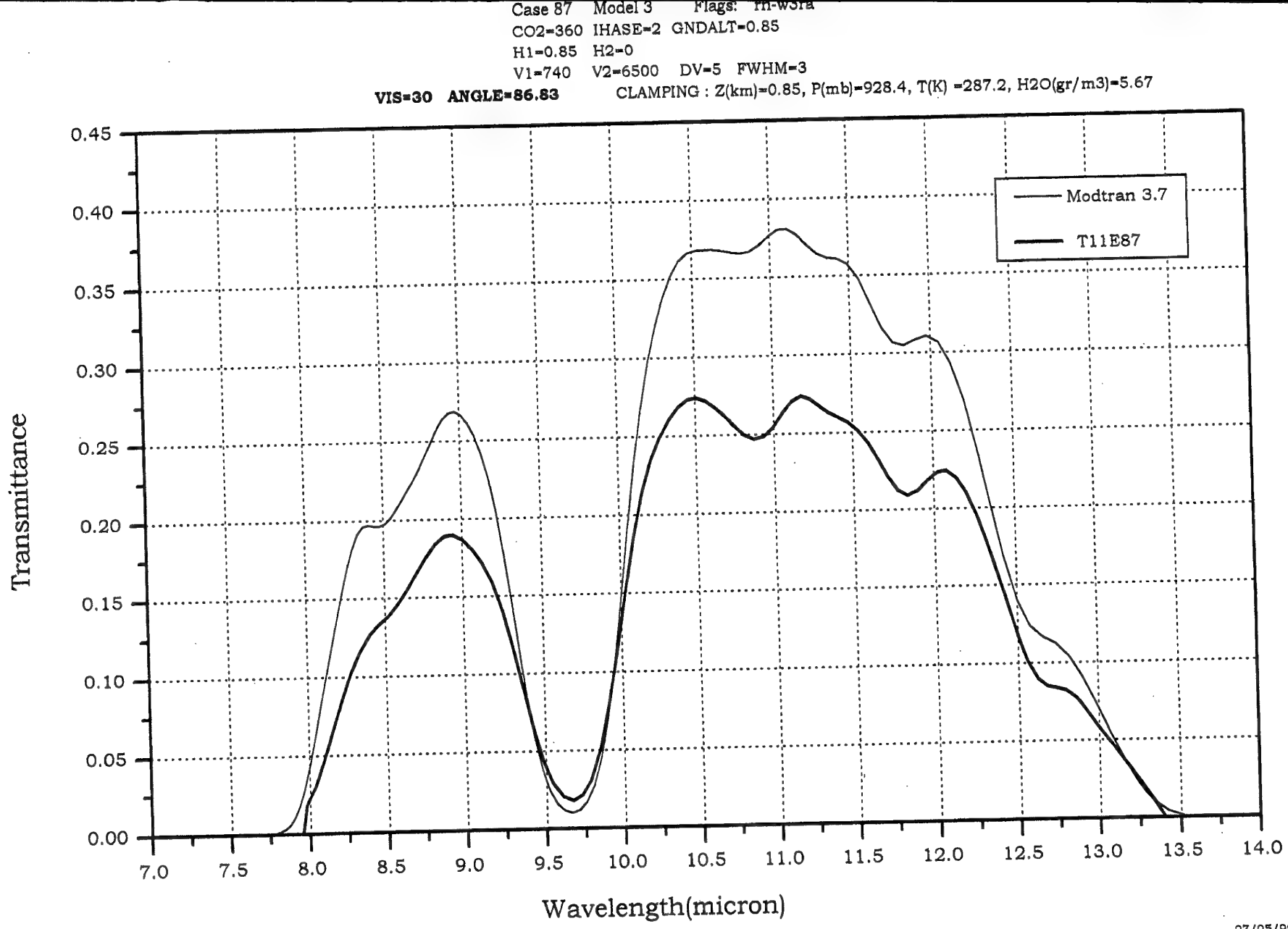

Figure 13b: The experimental results in the 7-14μm spectral region for zenith angle 87° compared to the prediction of the MODTRAN 3.7 code.

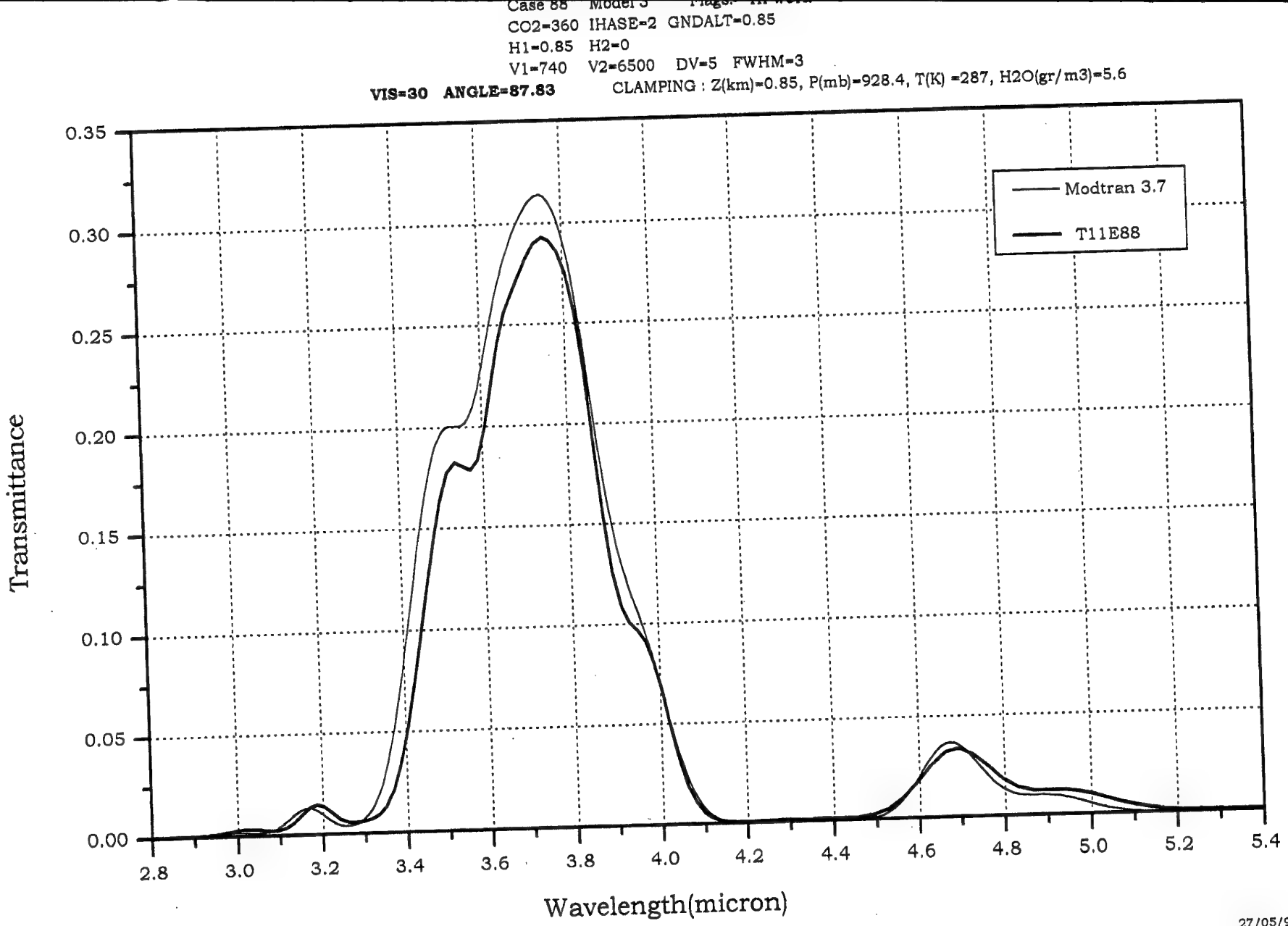

Figure 14a: The experimental results in the 2.8-5.4μm spectral region for zenith angle 88° compared to the prediction of the MODTRAN 3.7 code.

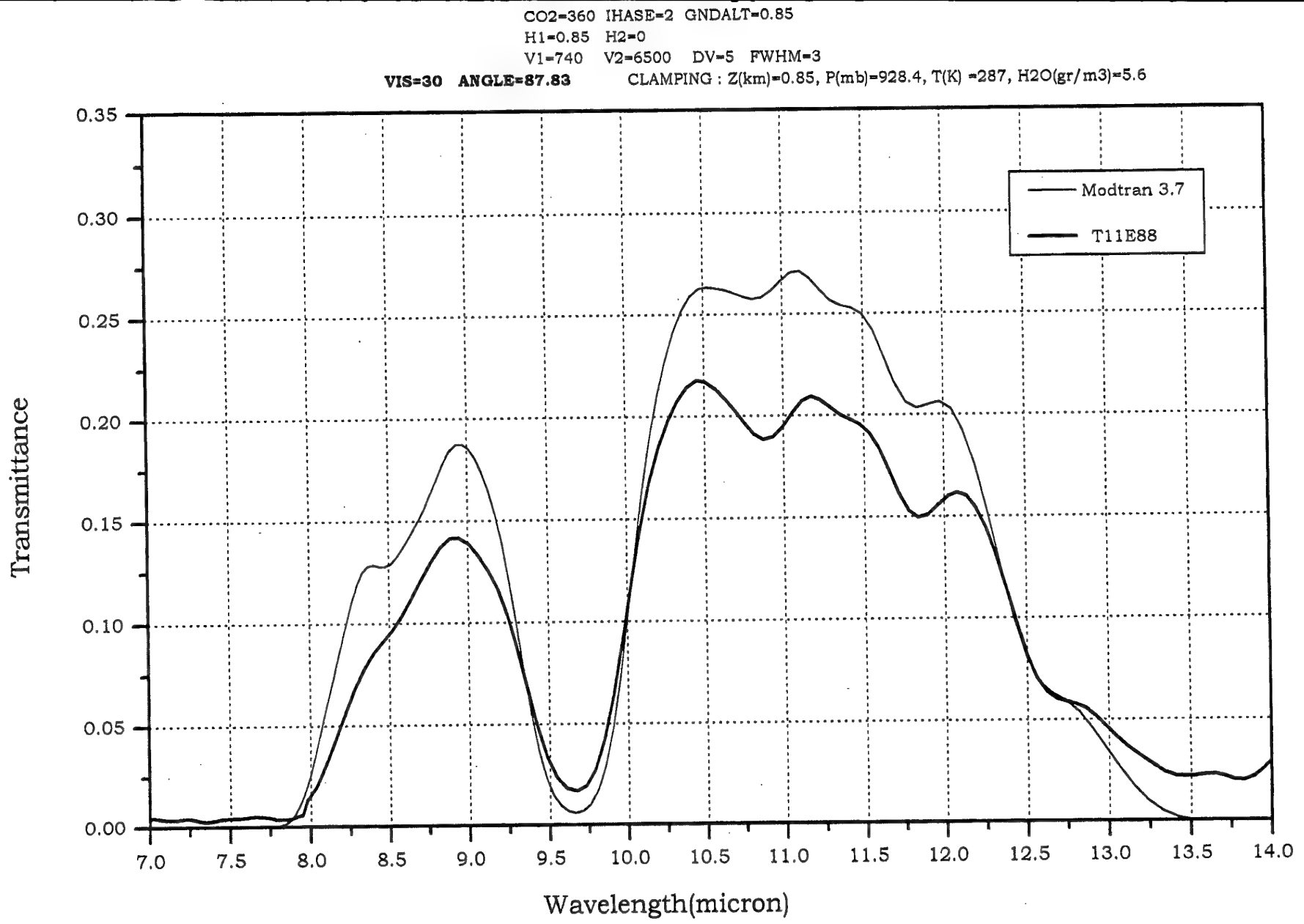

Figure 14b: The experimental results in the 7-14μm spectral region for zenith angle 88° compared to the prediction of the MODTRAN 3.7 code.

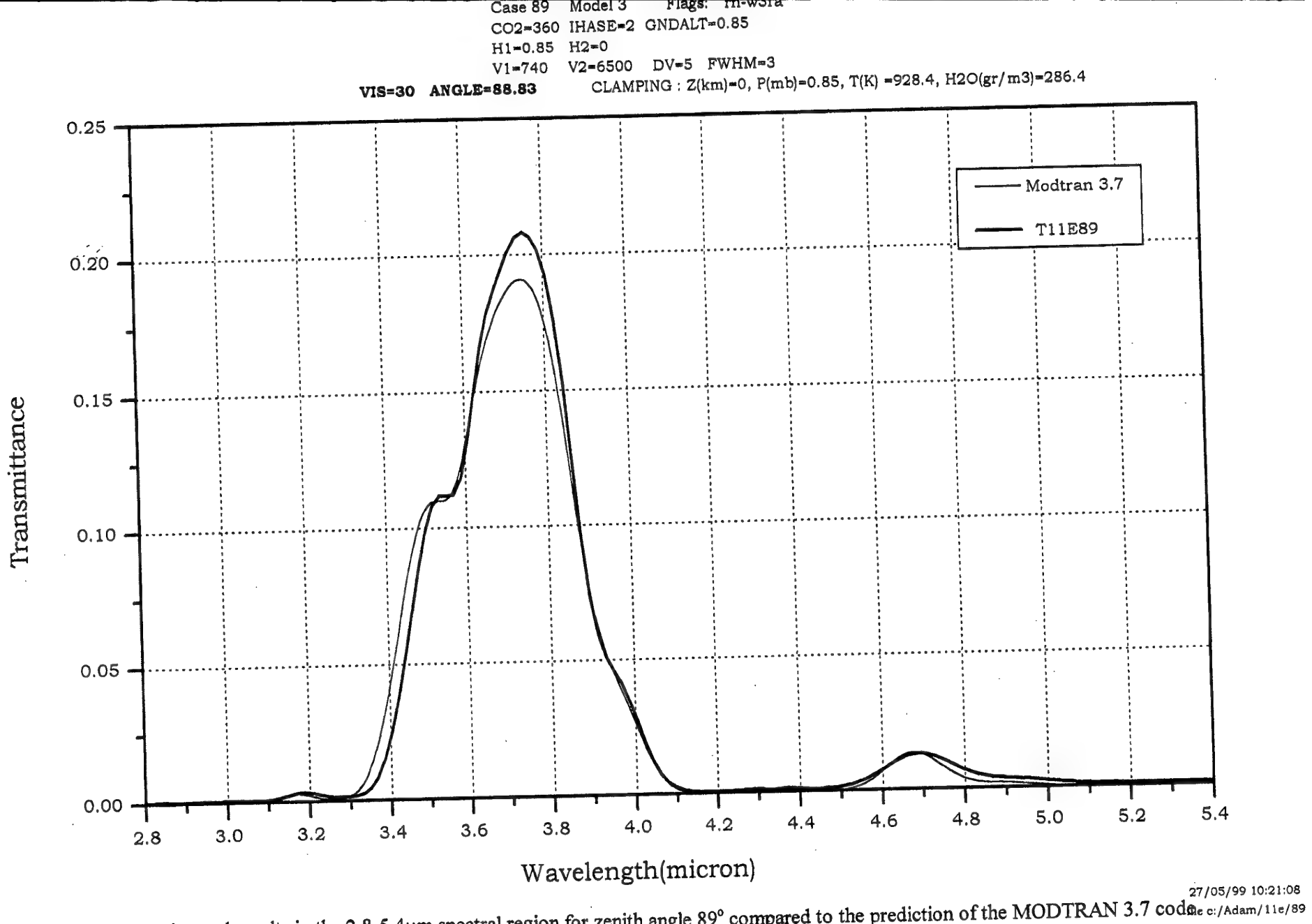

Figure 15a: The experimental results in the 2.8-5.4μm spectral region for zenith angle 89° compared to the prediction of the MODTRAN 3.7 code

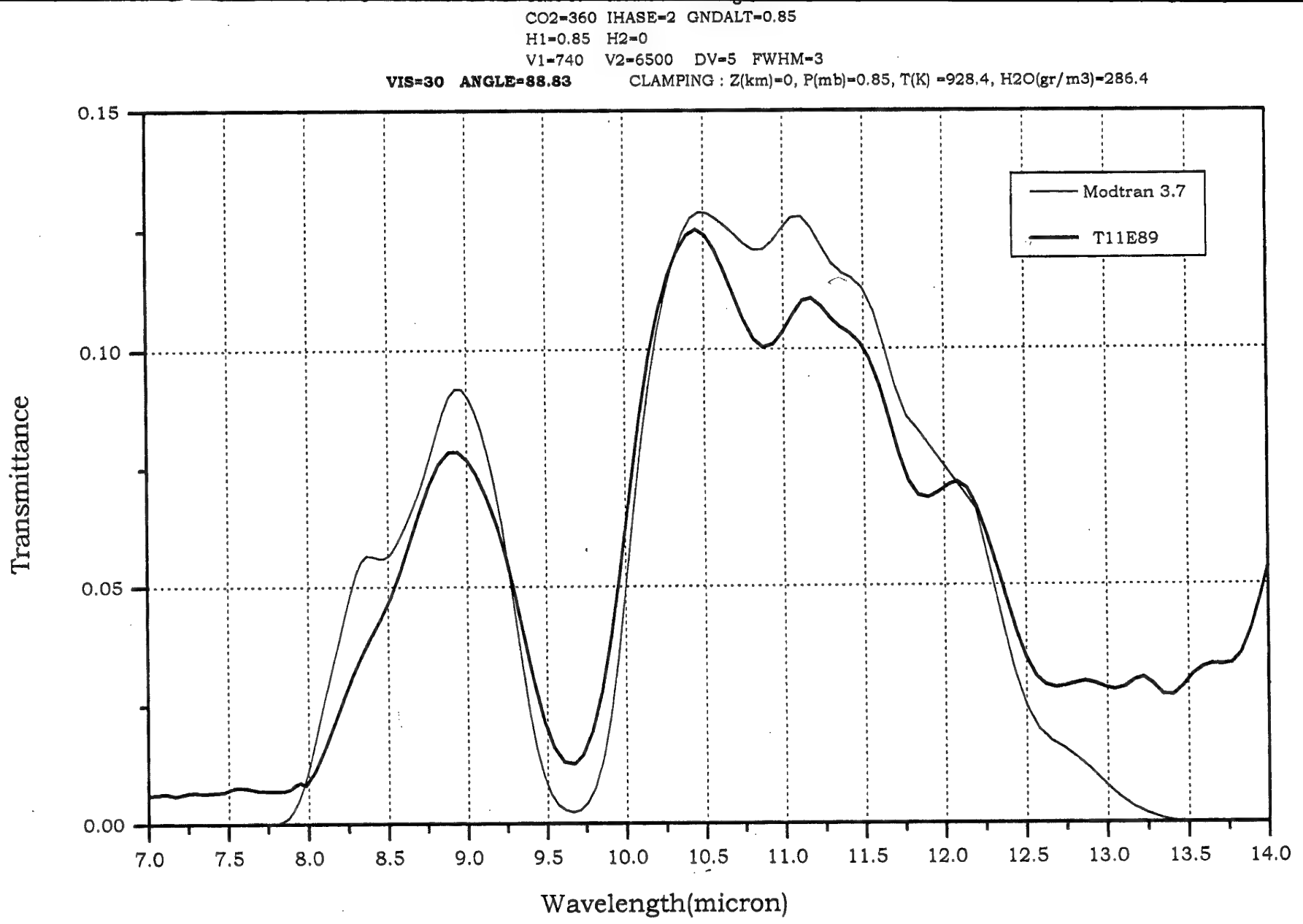

Figure 15b: The experimental results in the 7-14μm spectral region for zenith angle 89° compared to the prediction of the MODTRAN 3.7 code.

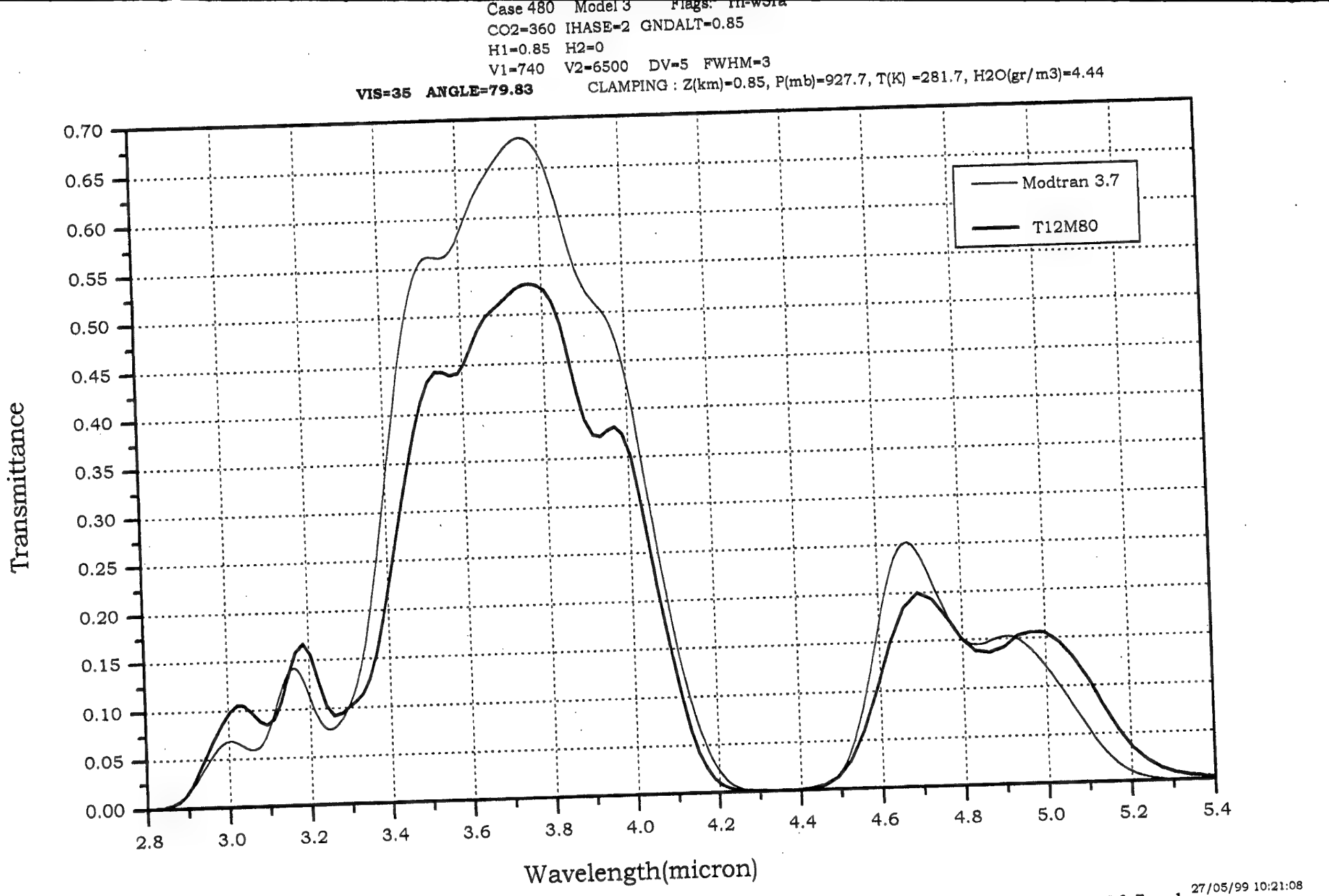

Figure 16a: The experimental results in the 2.8-5.4μm spectral region for zenith angle 80° compared to the prediction of the MODTRAN 3.7 code

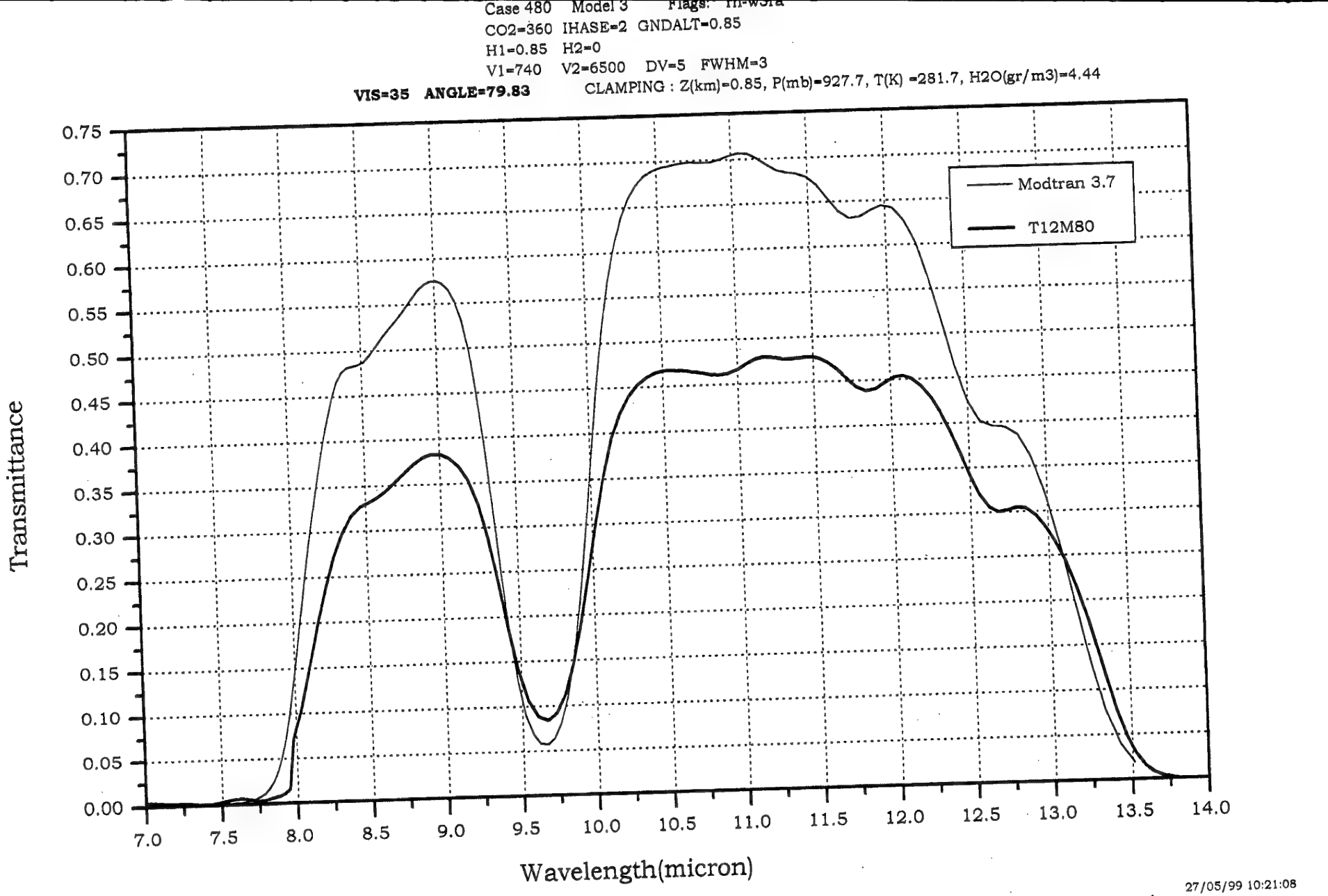

Figure 16b: The experimental results in the 7-14μm spectral region for zenith angle 80° compared to the prediction of the MODTRAN 3.7 code.

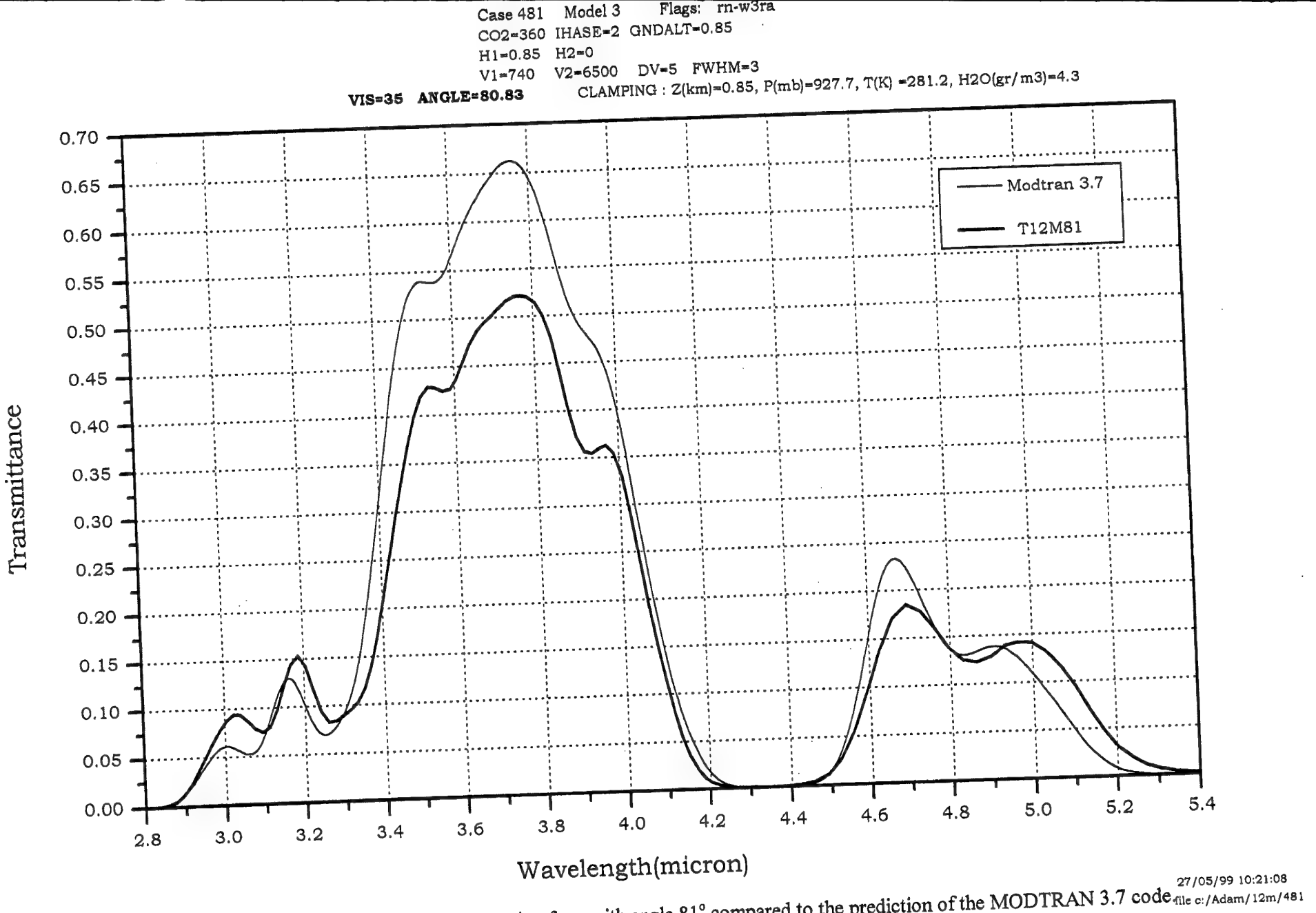

Figure 17a: The experimental results in the 2.8-5.4μm spectral region for zenith angle 81° compared to the prediction of the MODTRAN 3.7 code

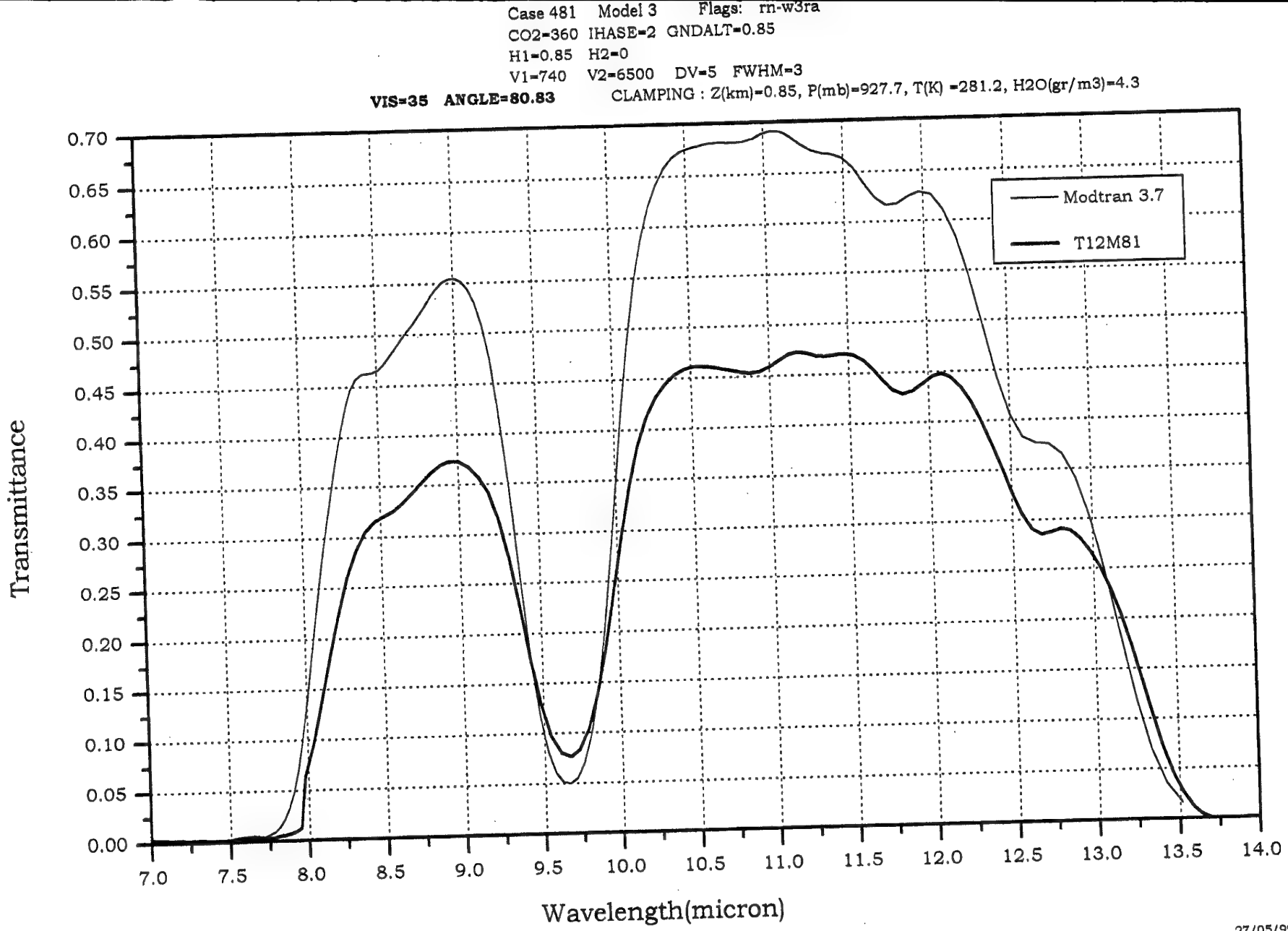

Figure 17b: The experimental results in the 7-14μm spectral region for zenith angle 81° compared to the prediction of the MODTRAN 3.7 code.

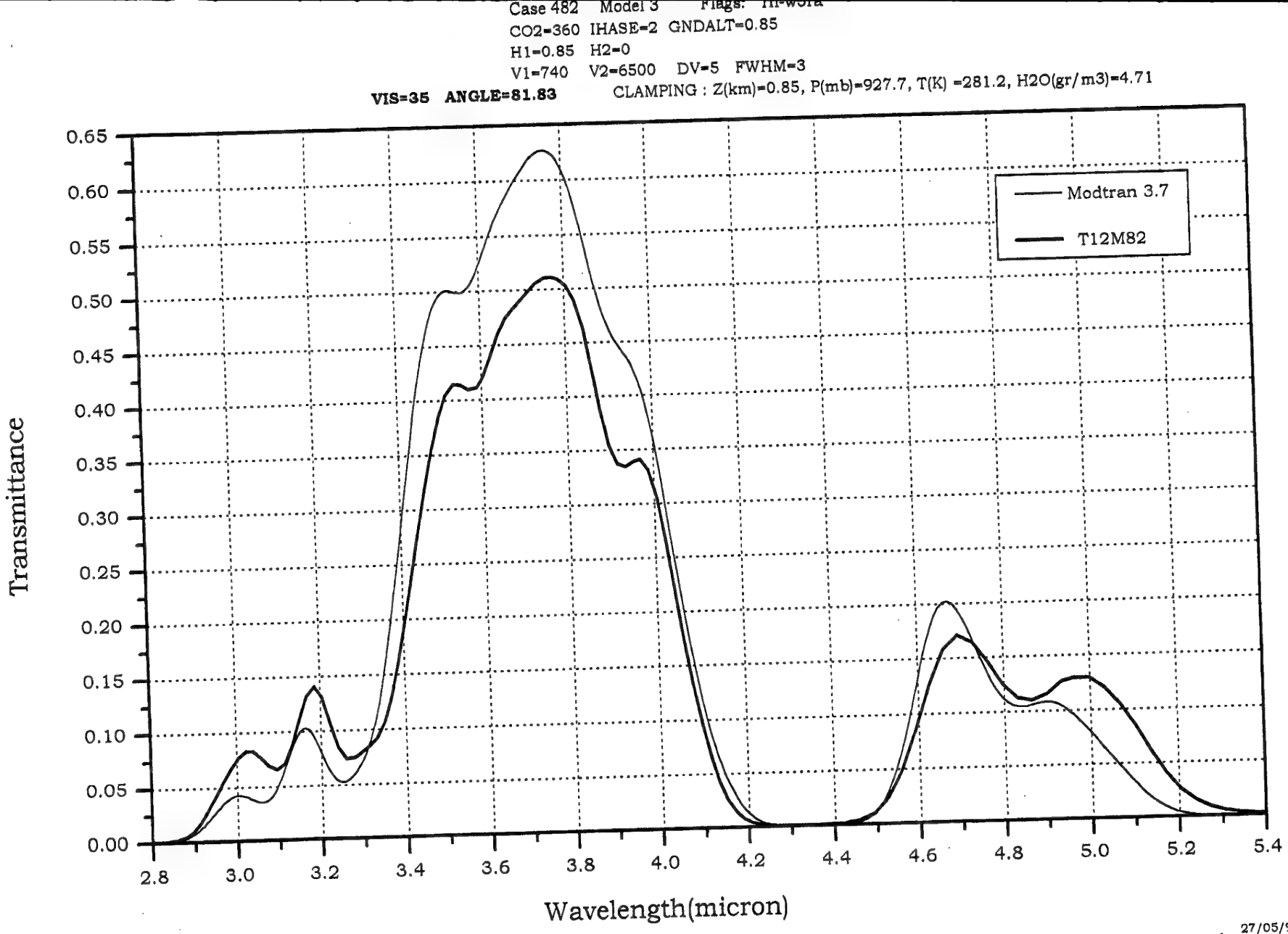

Figure 18a: The experimental results in the 2.8-5.4μm spectral region for zenith angle 82° compared to the prediction of the MODTRAN 3.7 code.

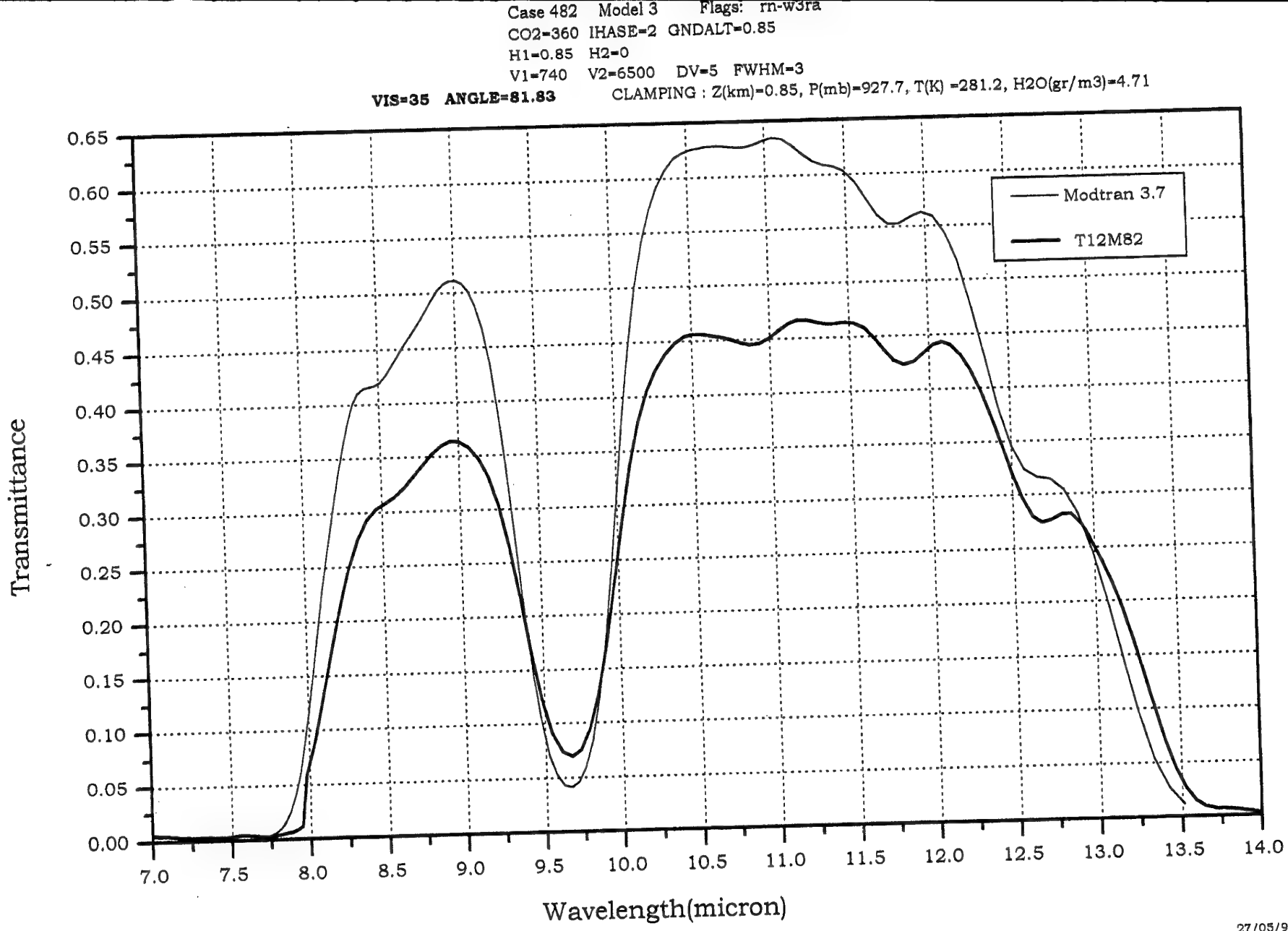

Figure 18b: The experimental results in the 7-14μm spectral region for zenith angle 82° compared to the prediction of the MODTRAN 3.7 code.

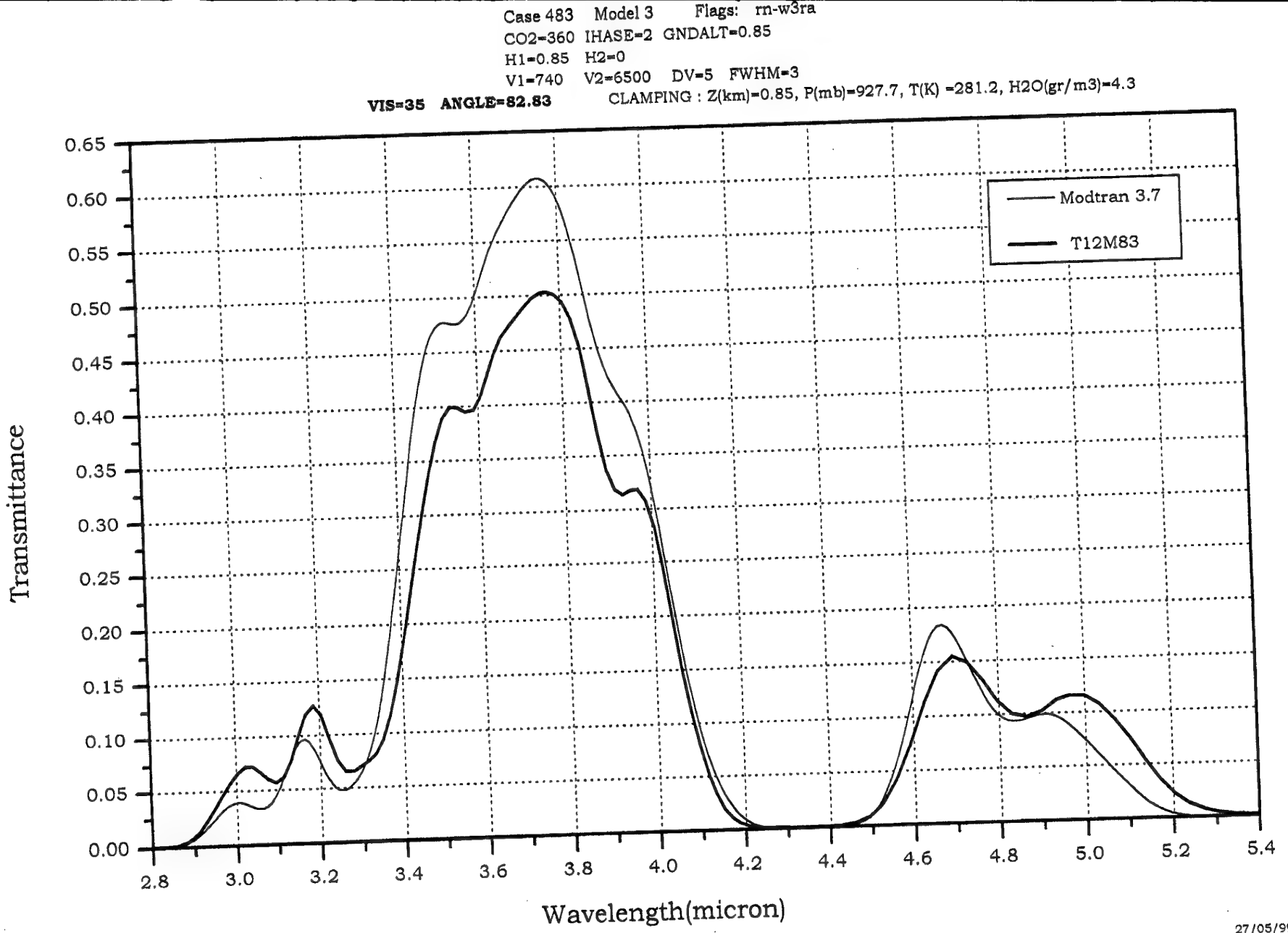

Figure 19a: The experimental results in the 2.8-5.4μm spectral region for zenith angle 83° compared to the prediction of the MODTRAN 3.7 code

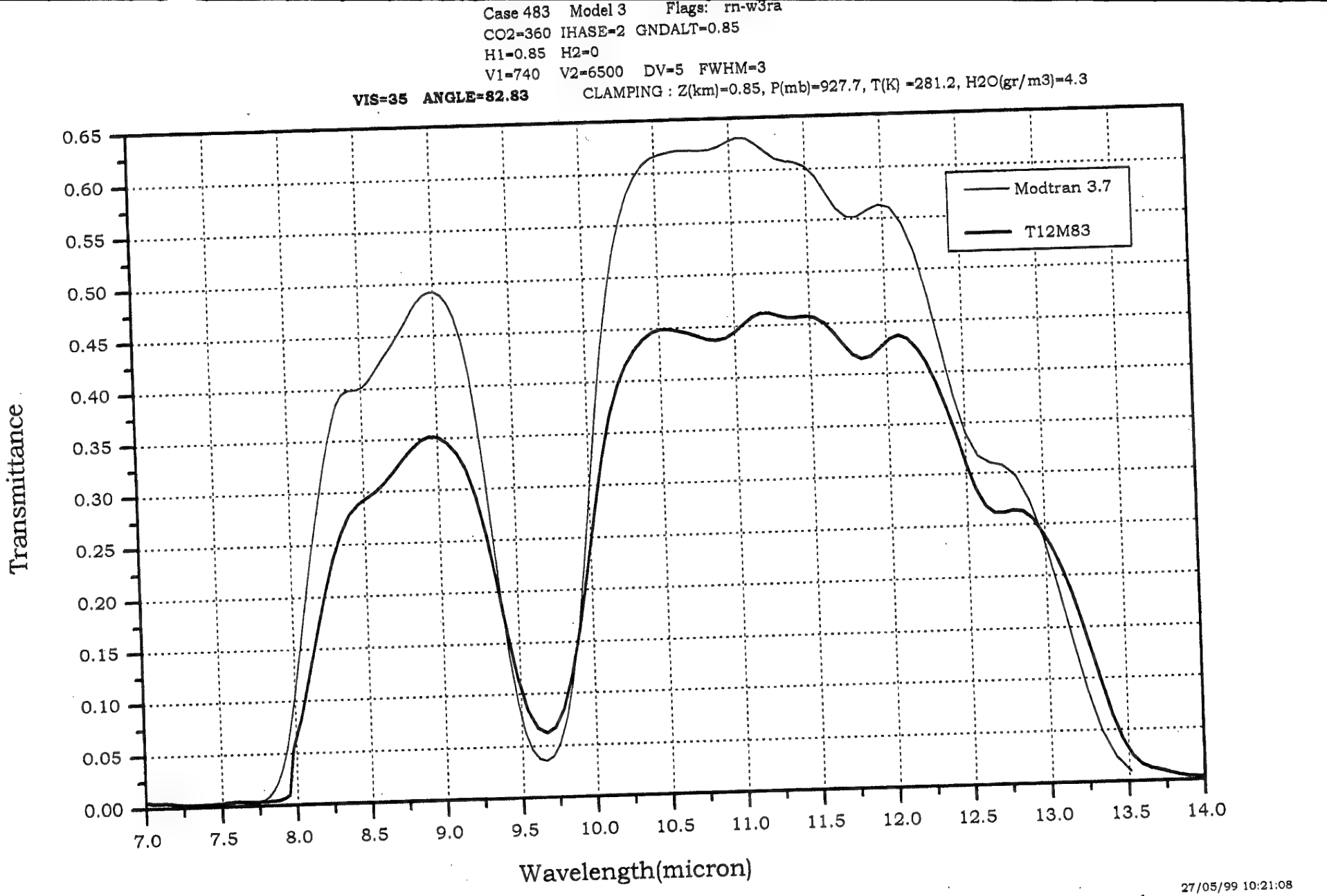

Figure 19b: The experimental results in the 7-14μm spectral region for zenith angle 83° compared to the prediction of the MODTRAN 3.7 code.

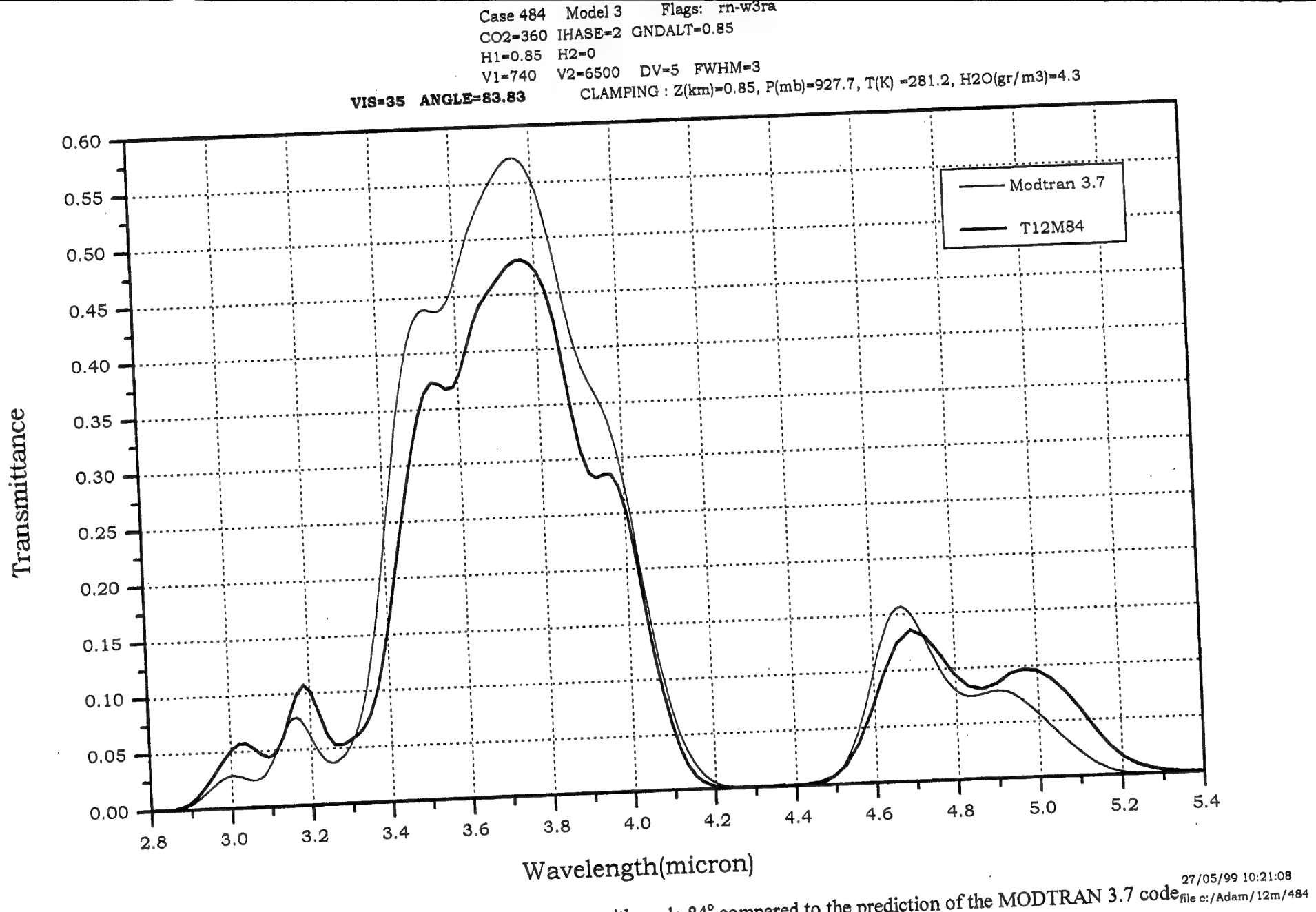

Figure 20a: The experimental results in the 2.8-5.4μm spectral region for zenith angle 84° compared to the prediction of the MODTRAN 3.7 code

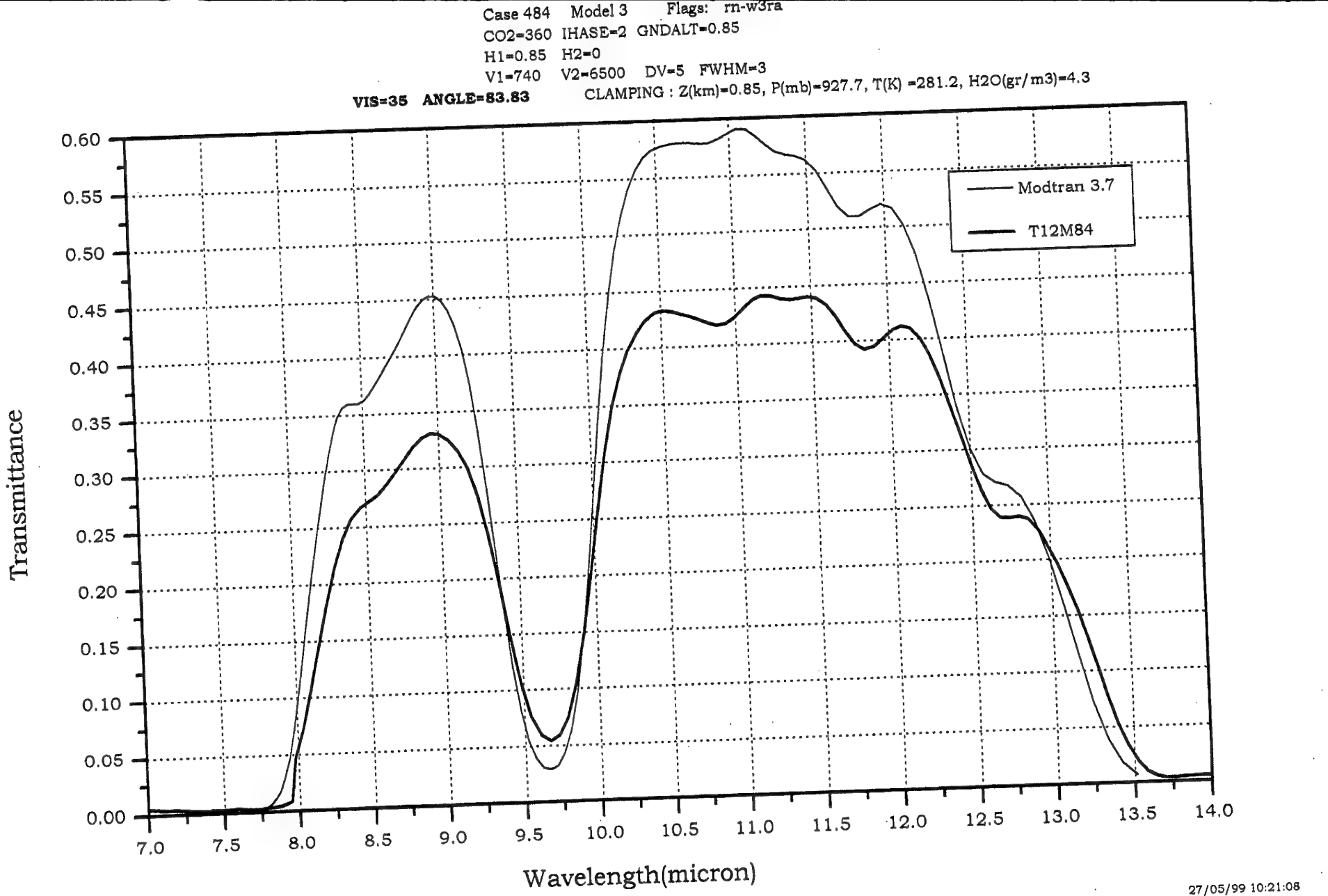

Figure 20b: The experimental results in the 7-14μm spectral region for zenith angle 84° compared to the prediction of the MODTRAN 3.7 code.

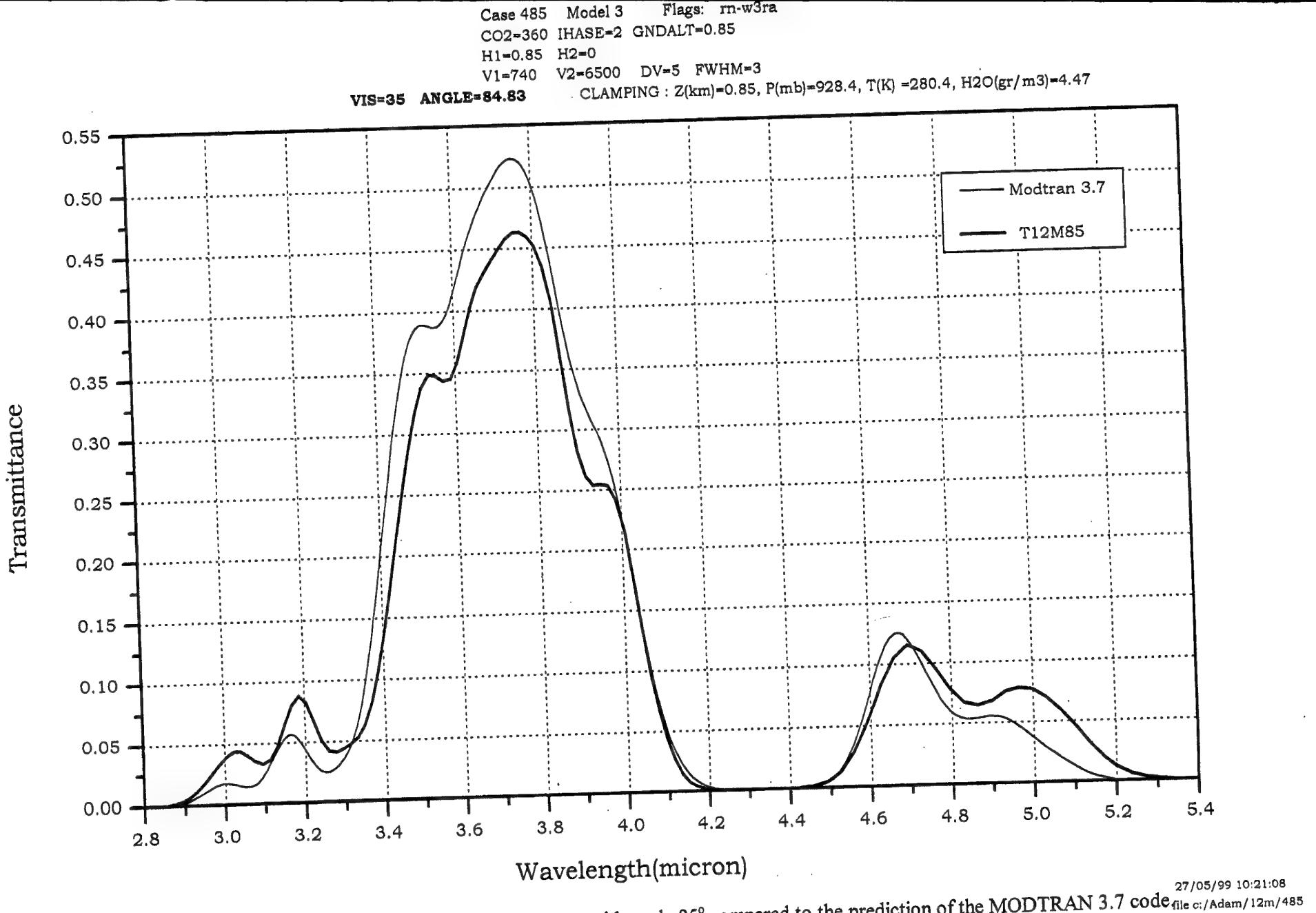

Figure 21a: The experimental results in the 2.8-5.4μm spectral region for zenith angle 85° compared to the prediction of the MODTRAN 3.7 code

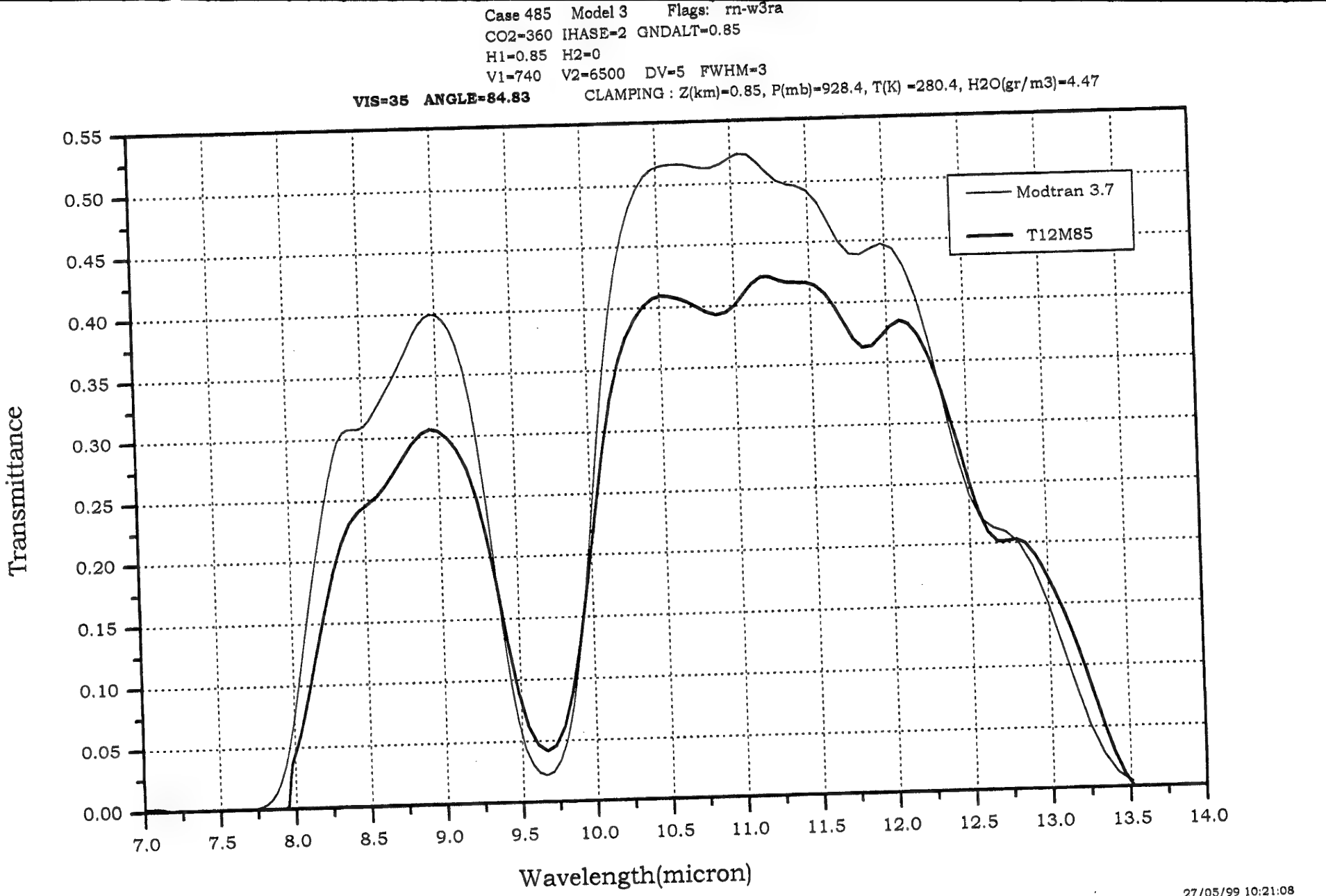

Figure 21b: The experimental results in the 7-14μm spectral region for zenith angle 85° compared to the prediction of the MODTRAN 3.7 code.

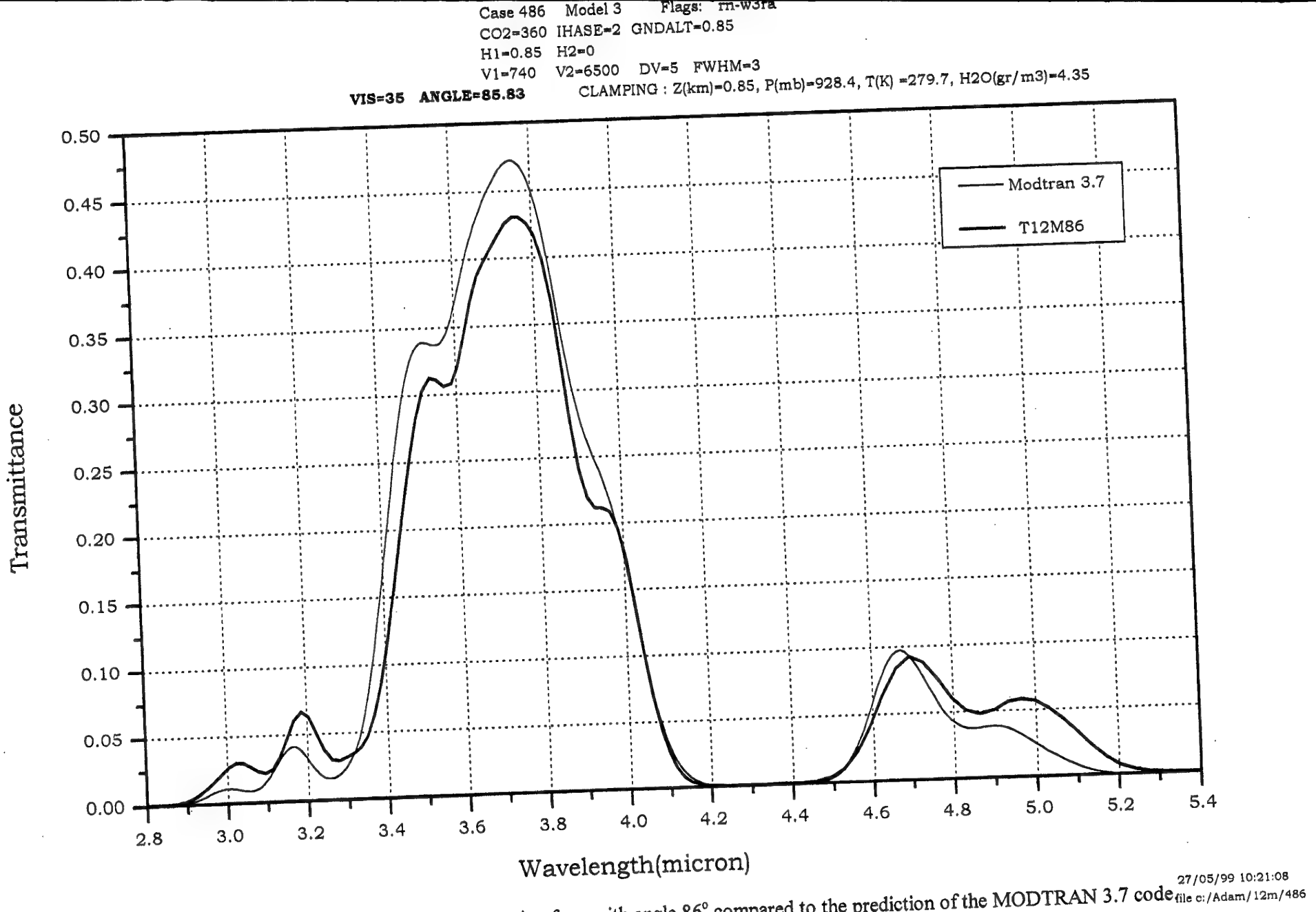

Figure 22a: The experimental results in the 2.8-5.4μm spectral region for zenith angle 86° compared to the prediction of the MODTRAN 3.7 code

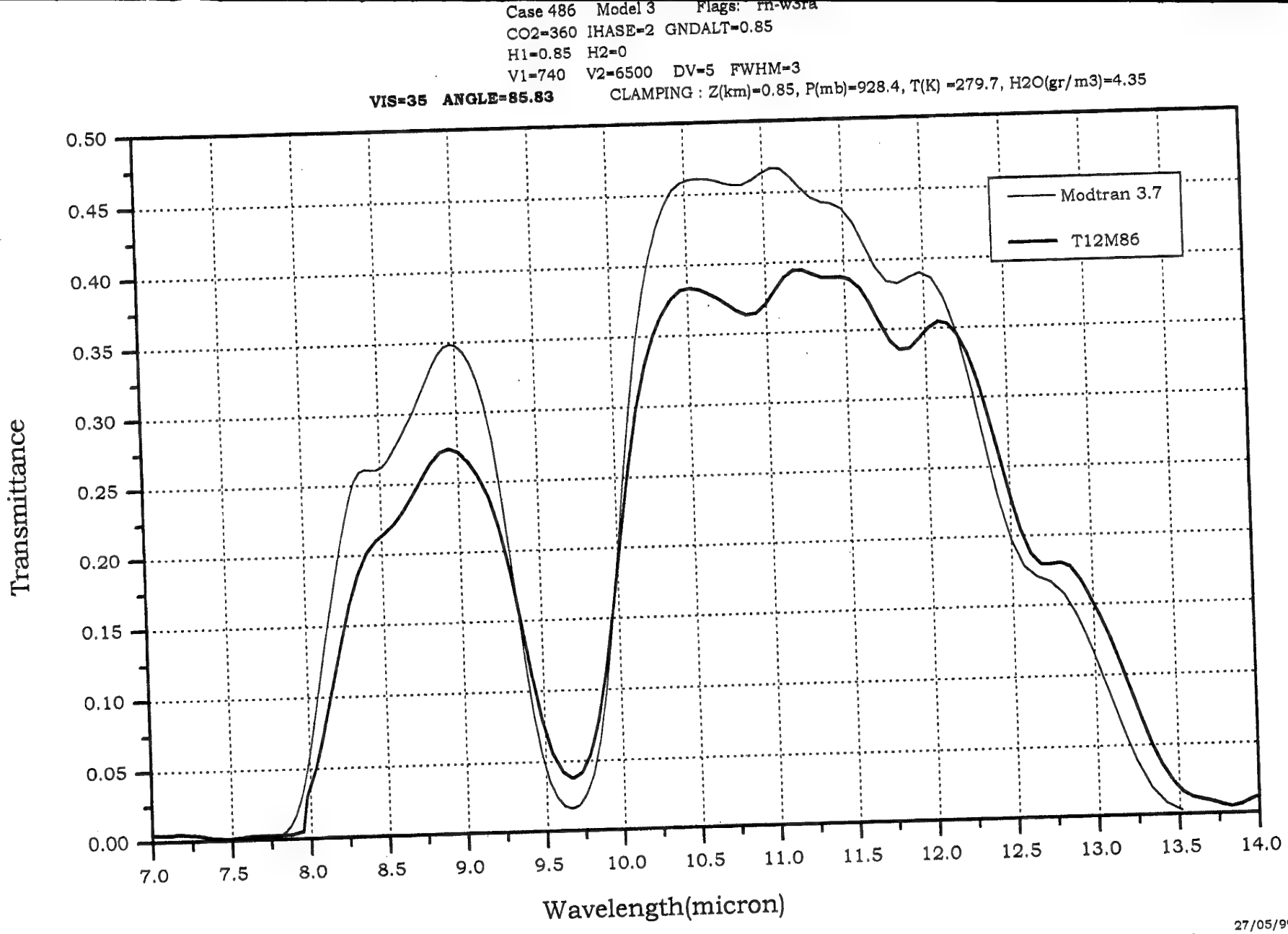

Figure 22b: The experimental results in the 7-14μm spectral region for zenith angle 86° compared to the prediction of the MODTRAN 3.7 code.

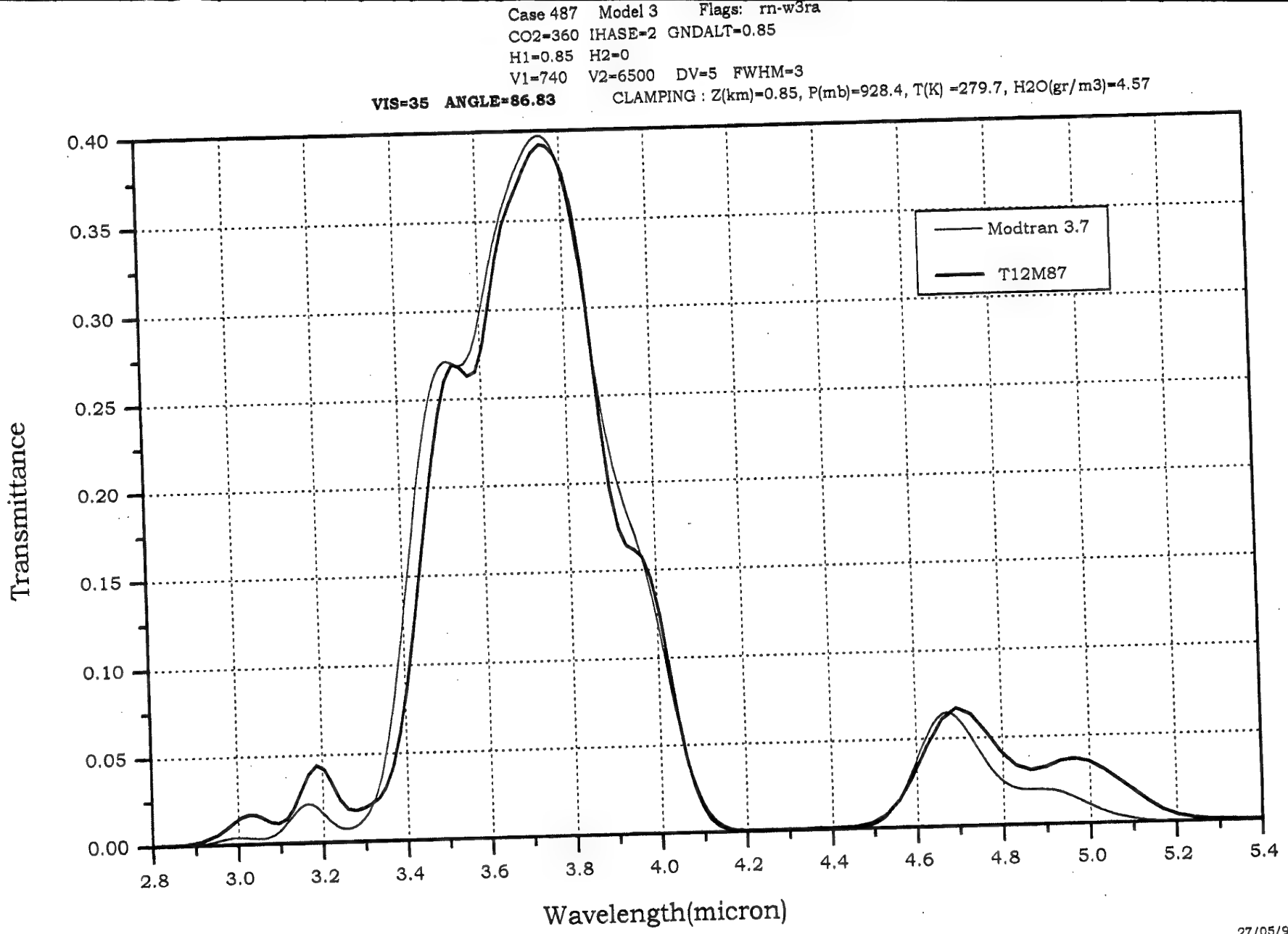

Figure 23a: The experimental results in the 2.8-5.4μm spectral region for zenith angle 87° compared to the prediction of the MODTRAN 3.7 code

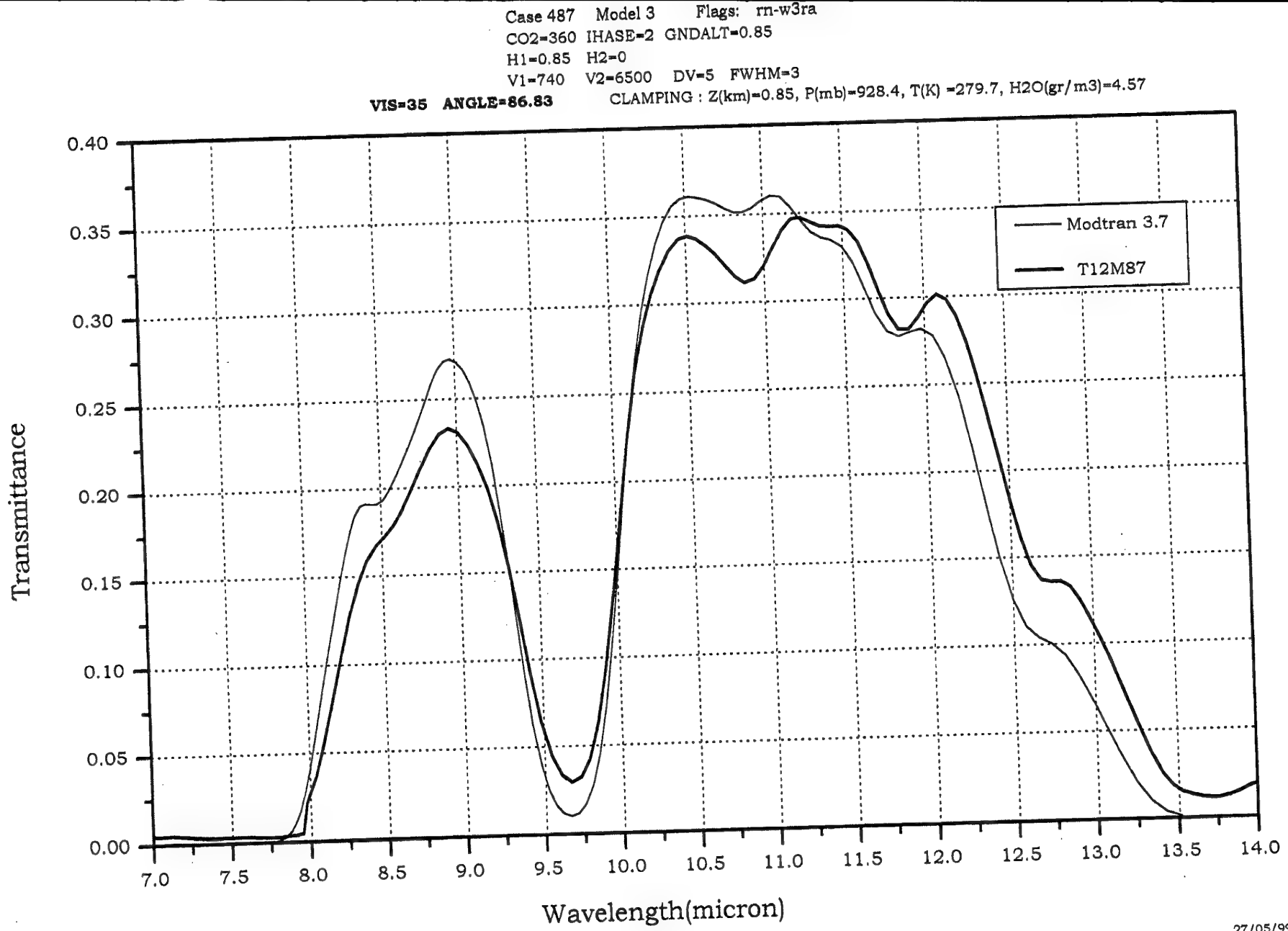

Figure 23b: The experimental results in the 7-14μm spectral region for zenith angle 87° compared to the prediction of the MODTRAN 3.7 code.

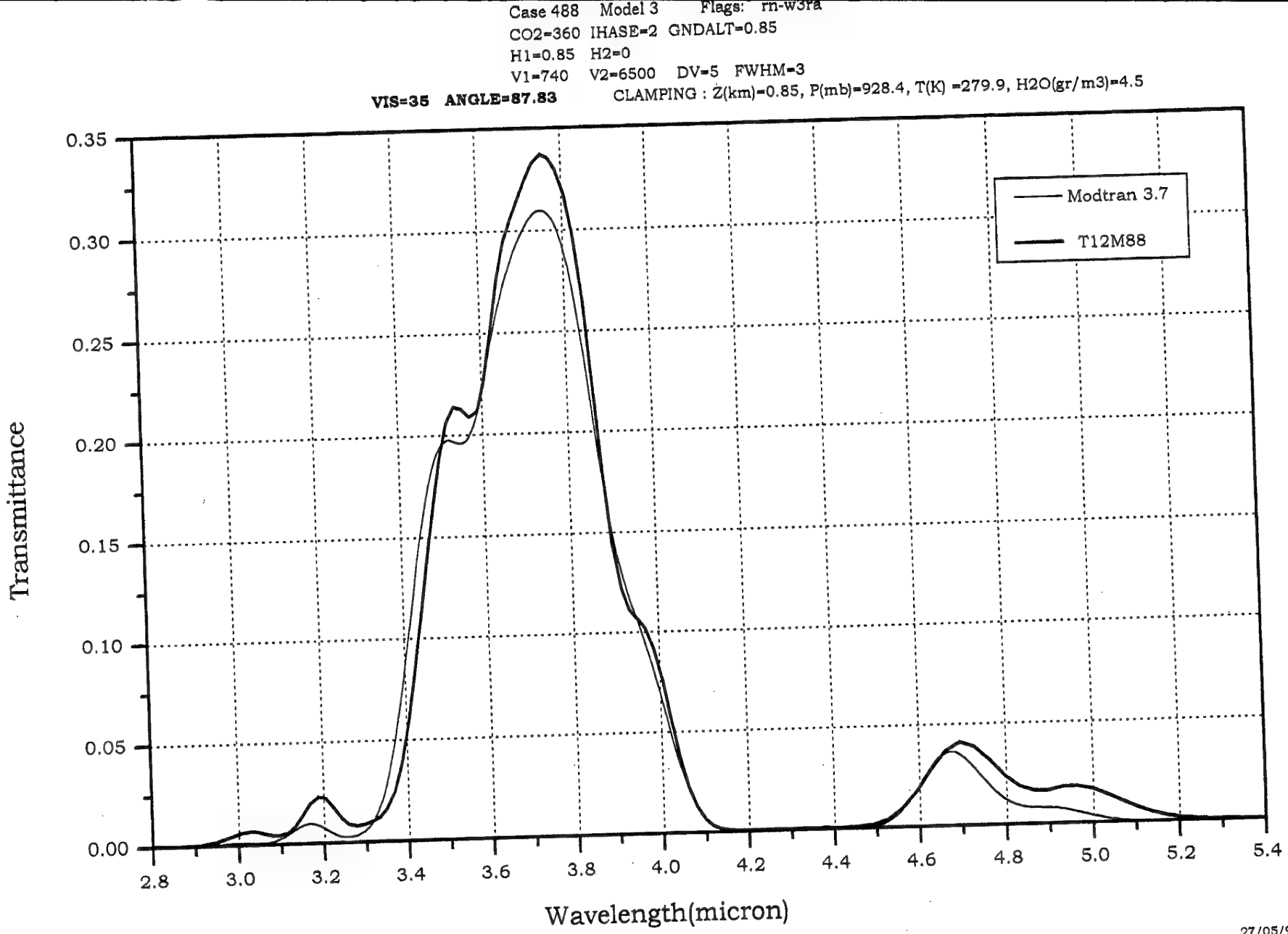

Figure 24a: The experimental results in the 2.8-5.4μm spectral region for zenith angle 88° compared to the prediction of the MODTRAN 3.7 code

CO2=360 IHASE=2 GNDALT=0.85
H1=0.85 H2=0
V1=740 V2=6500 DV=5 FWHM=3
VIS=35 ANGLE=87.83 CLAMPING : Z(km)=0.85, P(mb)=928.4, T(K) =279.9, H2O(gr/m3)=4.5

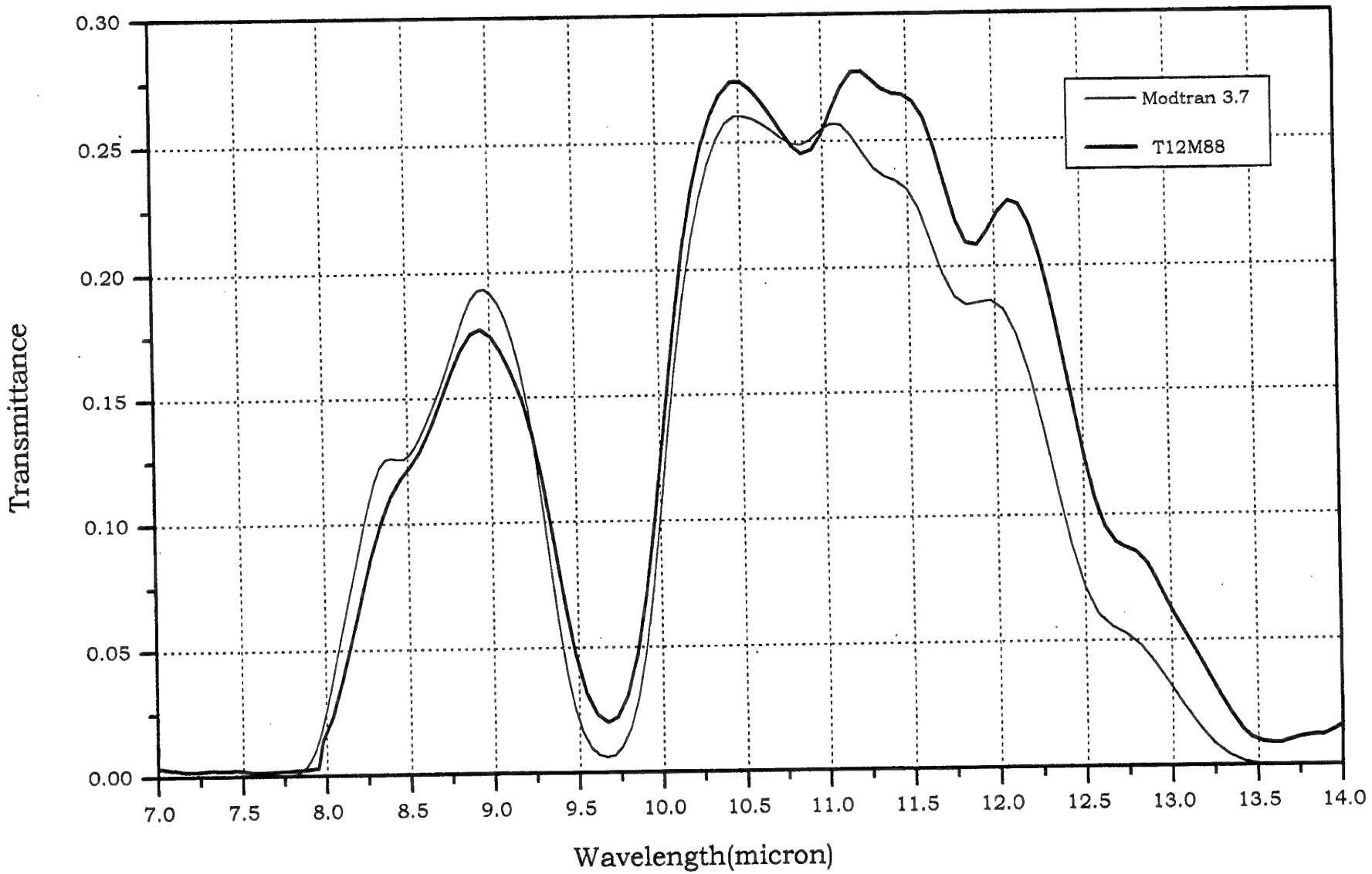

27/05/99 10:21:08
file c:/Adam/12m/488

Figure 24b: The experimental results in the 7-14μm spectral region for zenith angle 88° compared to the prediction of the MODTRAN 3.7 code.

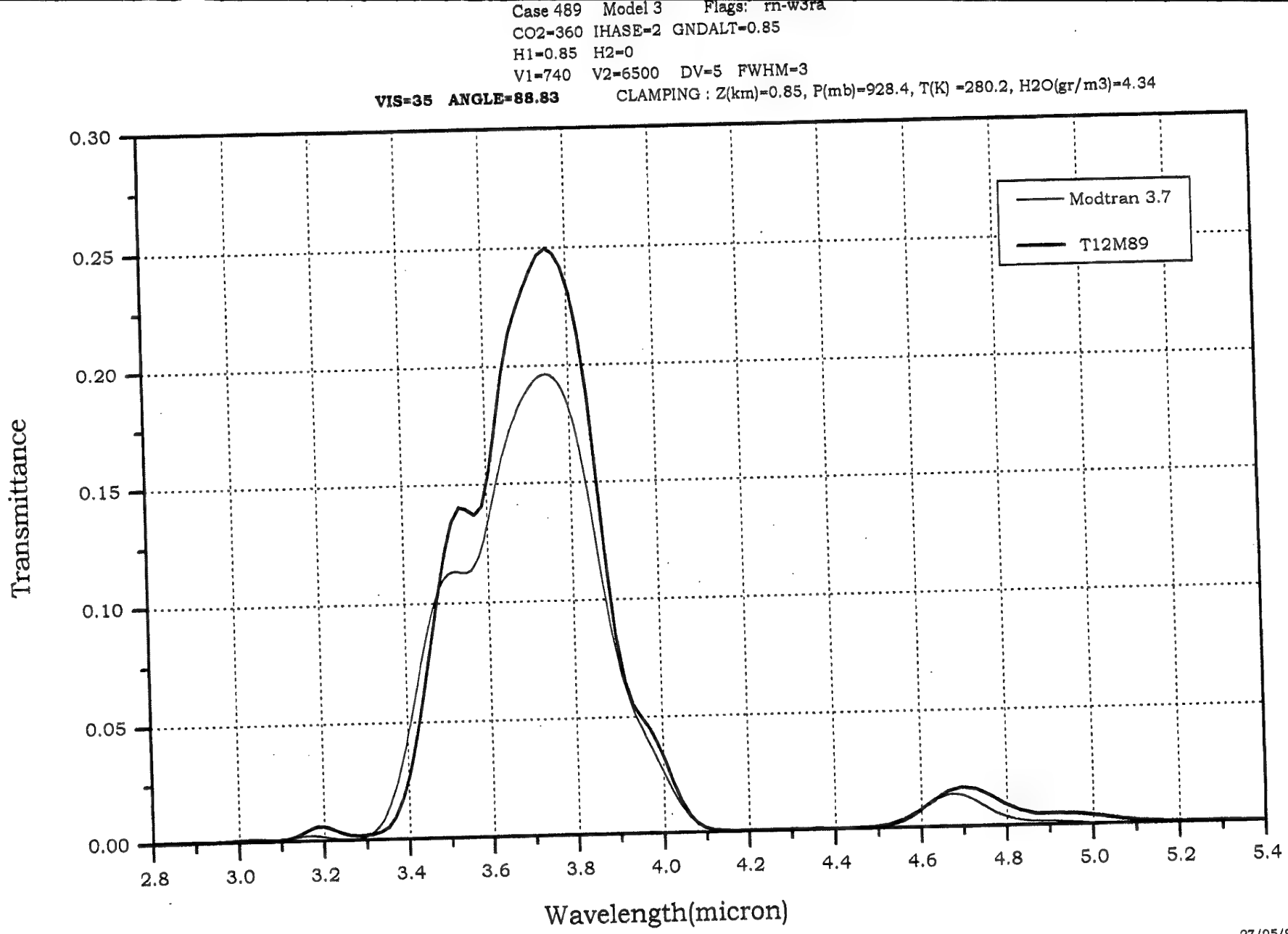

Figure 25a: The experimental results in the 2.8-5.4μm spectral region for zenith angle 89° compared to the prediction of the MODTRAN 3.7 code

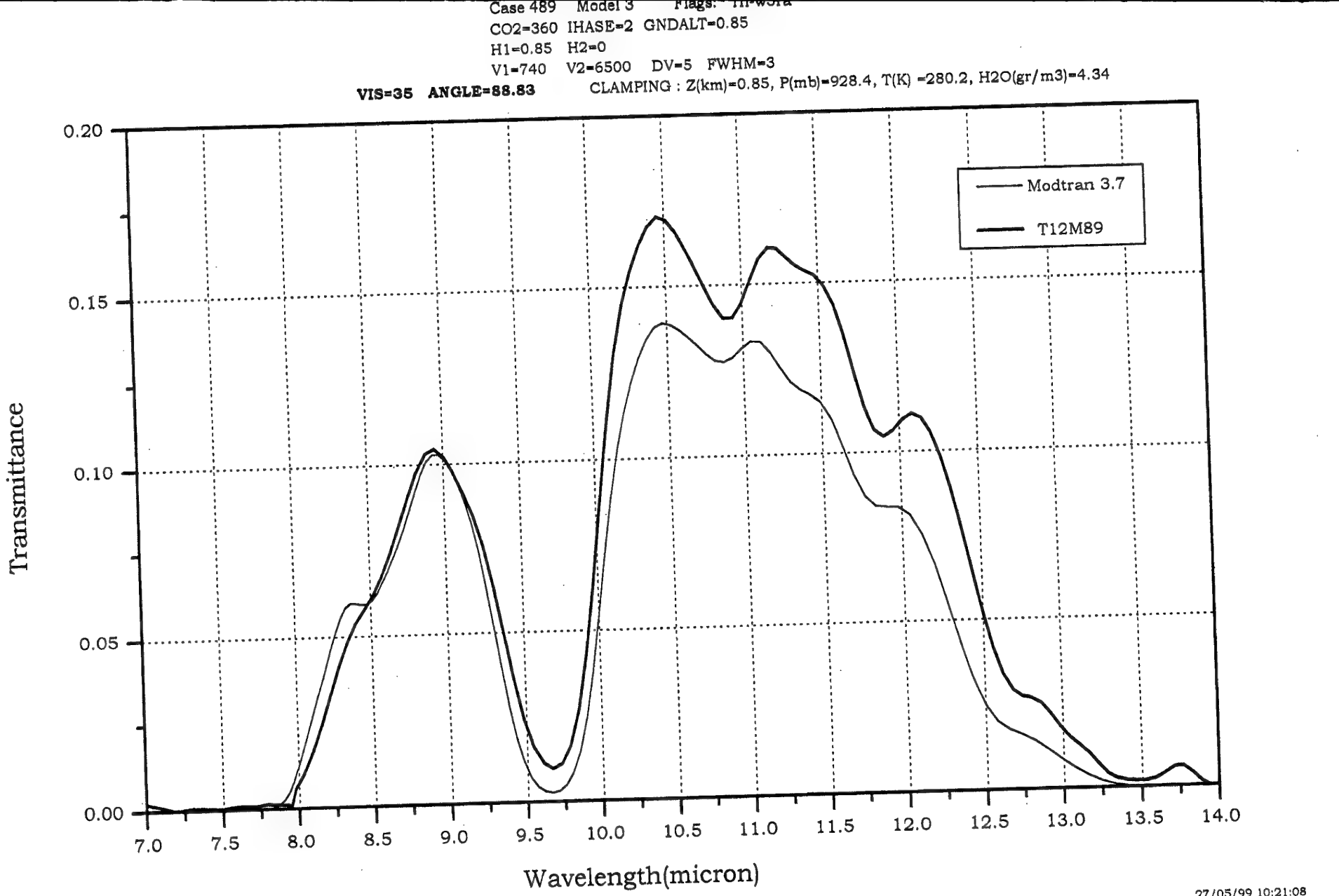

Figure 25b: The experimental results in the 7-14μm spectral region for zenith angle 89° compared to the prediction of the MODTRAN 3.7 code.

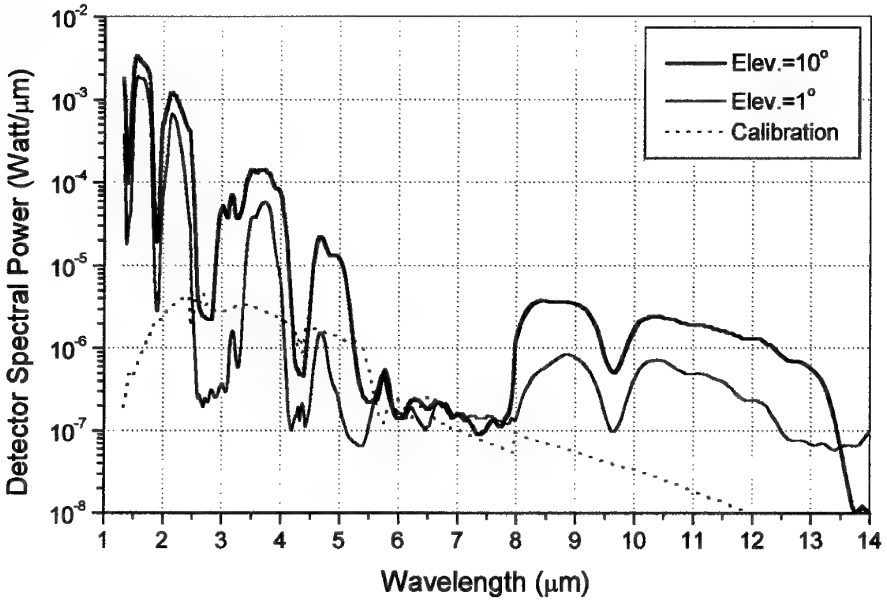

Figure 26: The spectral power that falls on the detector.

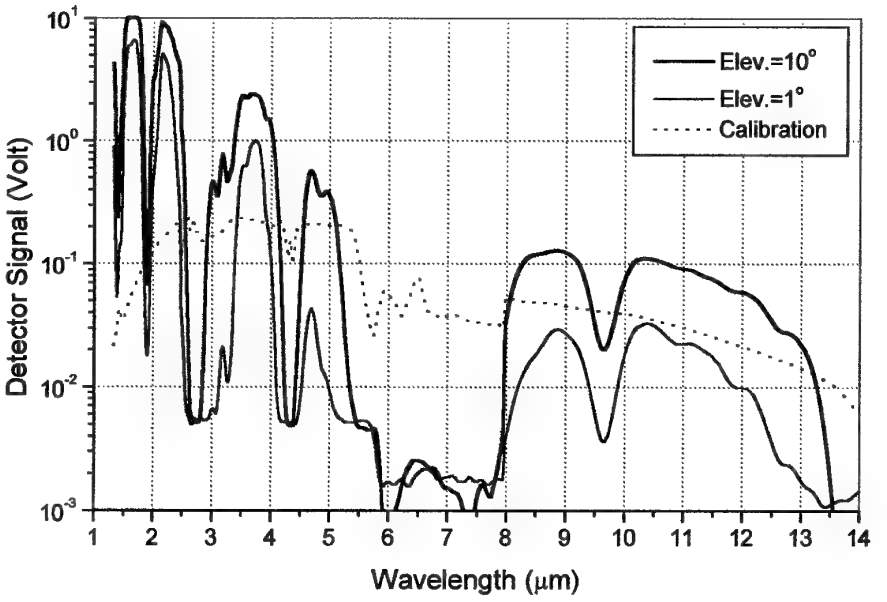

Figure 27: The raw signal that is generated by the detector.

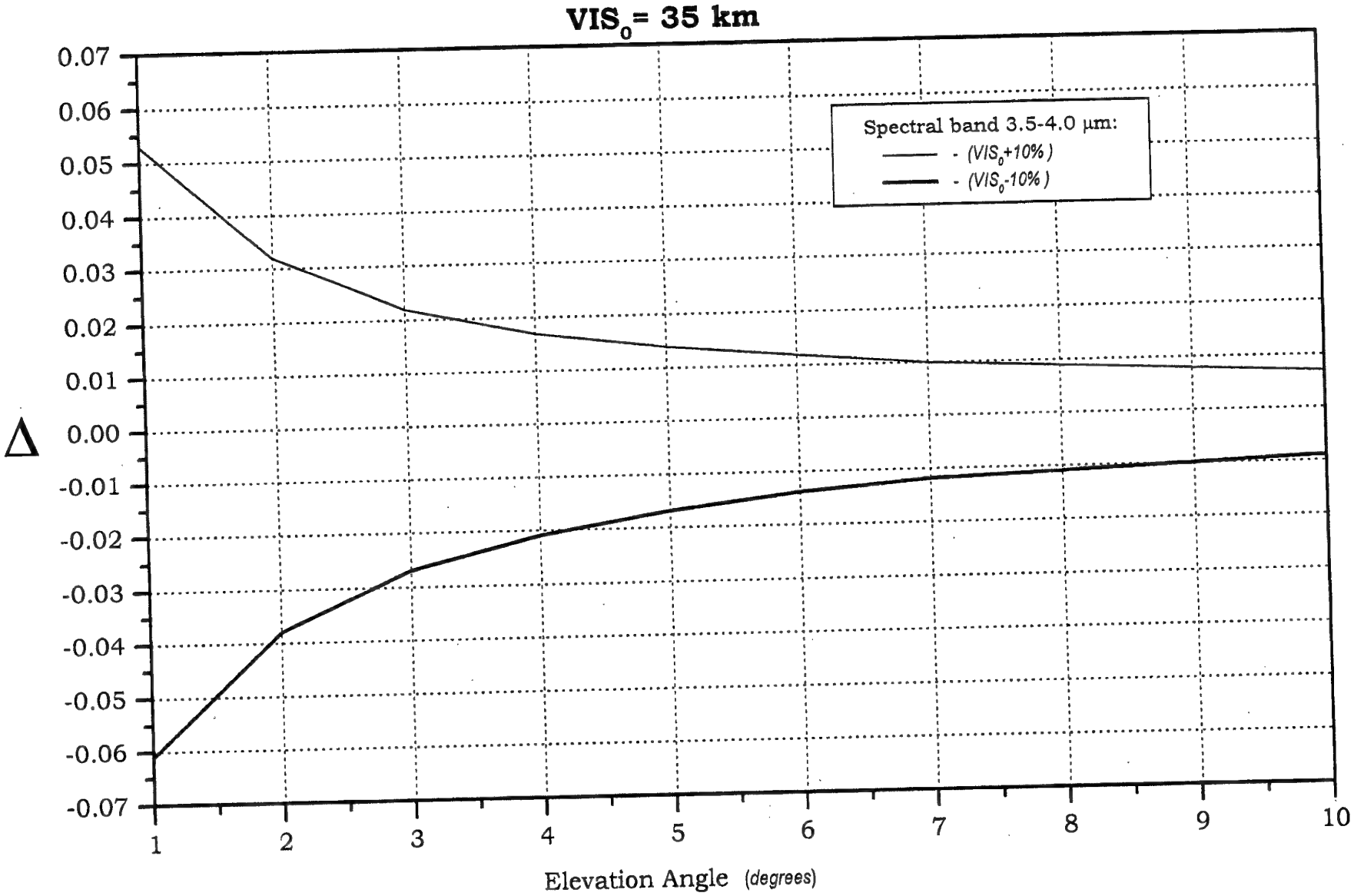

Figure 28: The averaged relative error of all our predicted transmittance in the spectral region 3.5-4.0μm (morning, January 12, 1999).

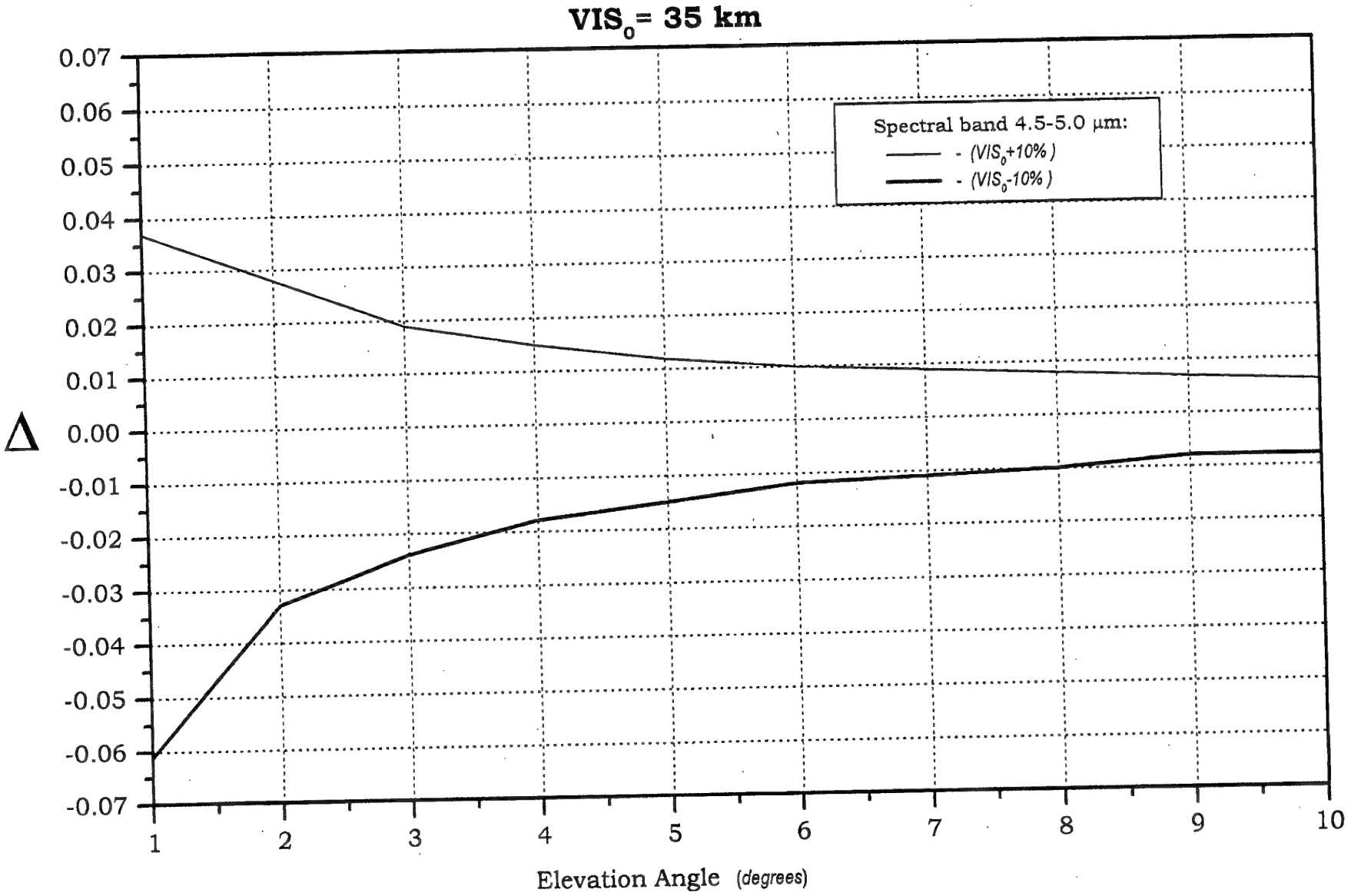

Figure 29: The averaged relative error of all our predicted transmittance in the spectral region 4.5-5.0μm (morning, January 12, 1999).

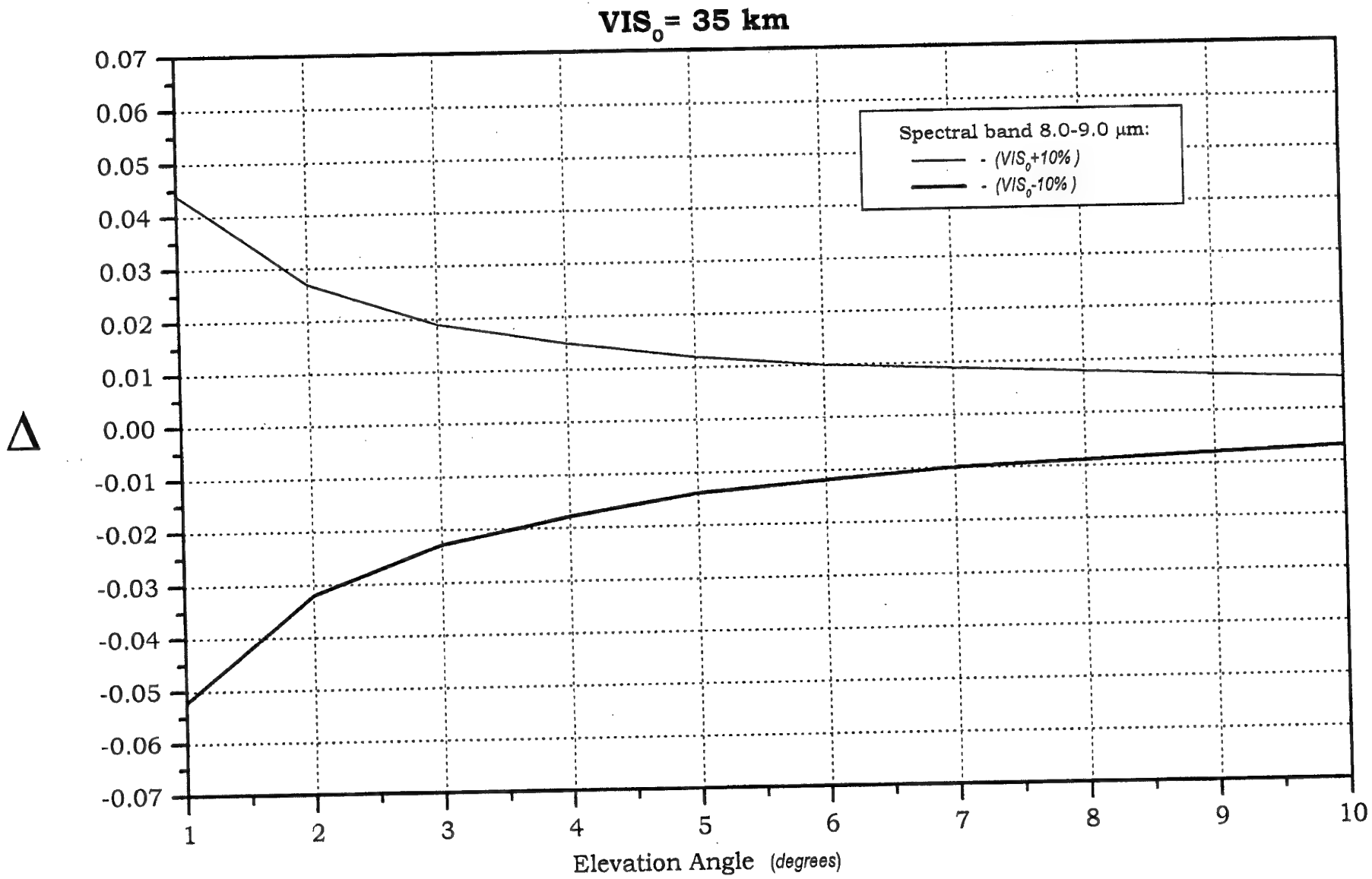

Figure 30: The averaged relative error of all our predicted transmittance in the spectral region 8.0-9.0μm (morning, January 12, 1999).

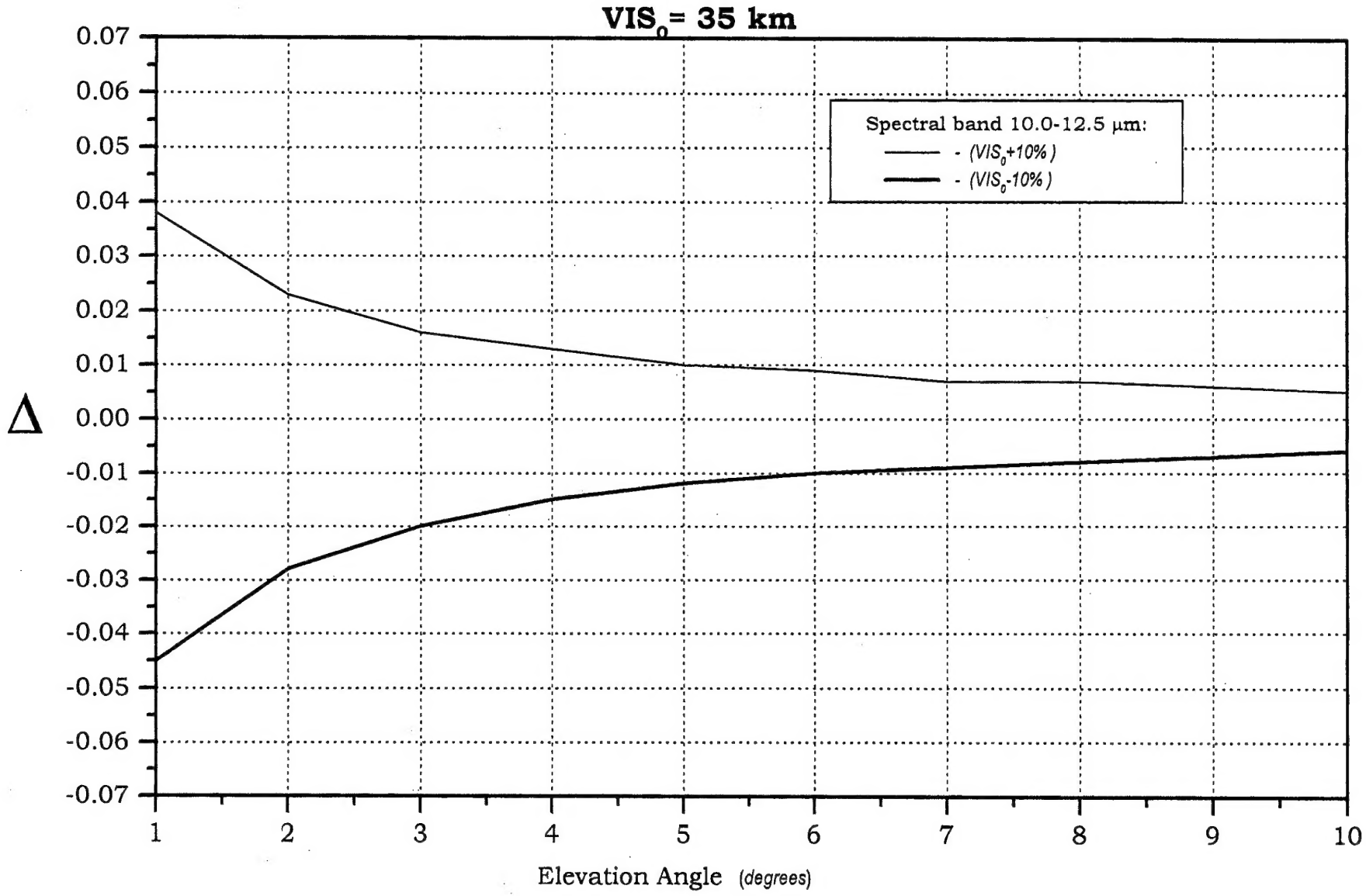

Figure 31: The averaged relative error of all our predicted transmittance in the spectral region 10.0-12.5μm (morning, January 12, 1999).

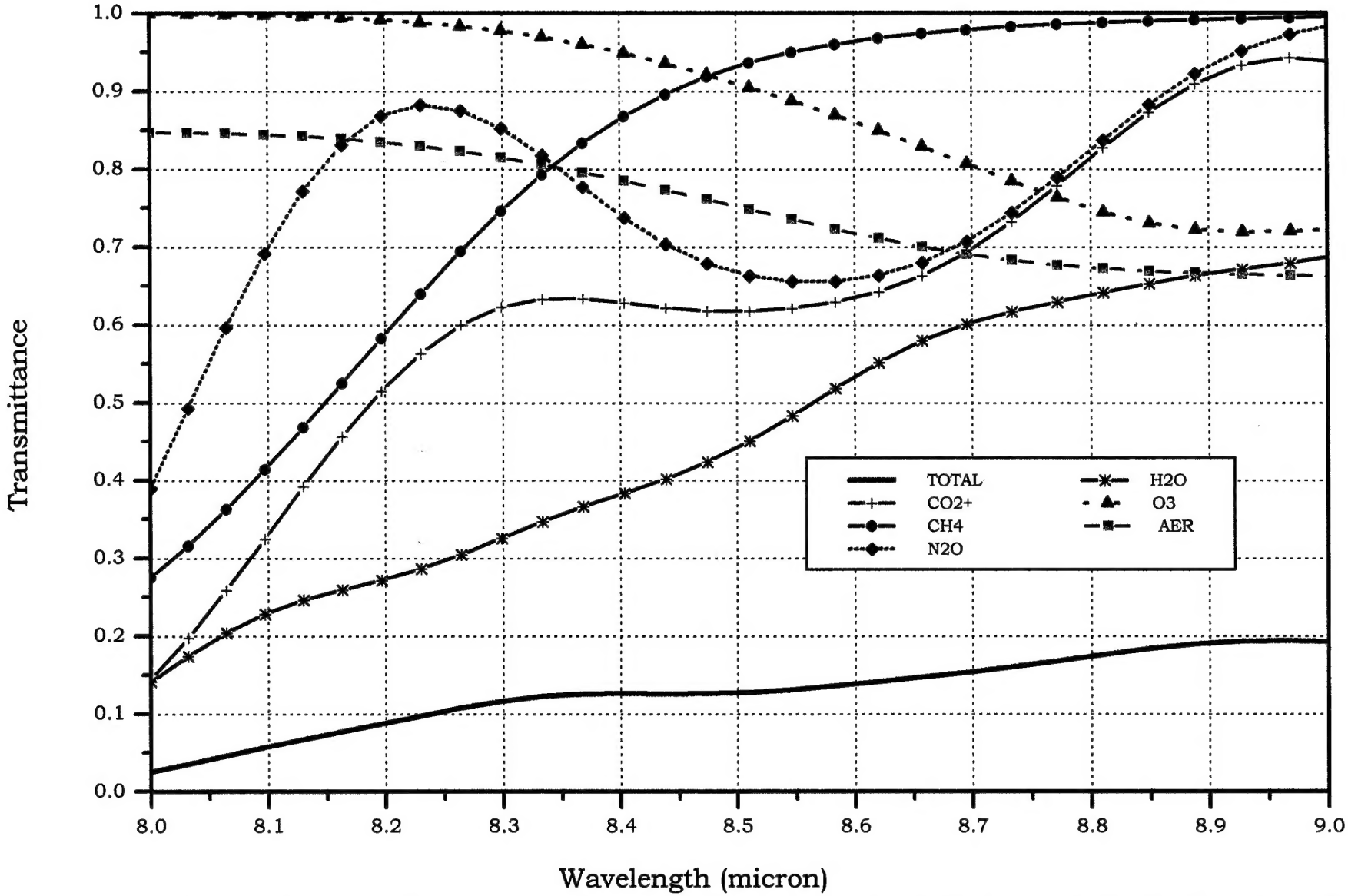

Figure 32: The detailed contribution of different atmospheric constituents to the total absorption in the 8-9μm spectral region at θ=88°.

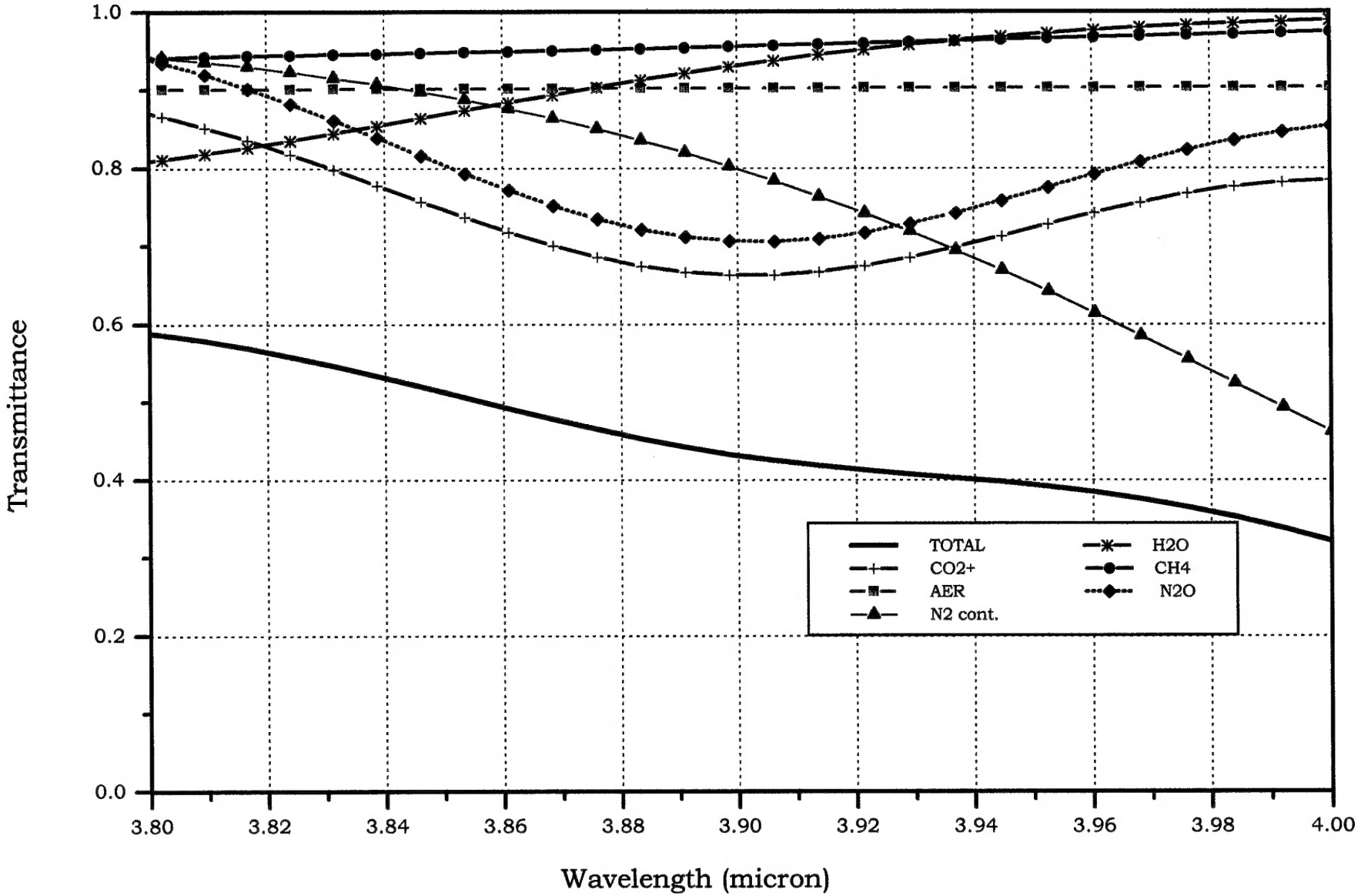

Figure 33: The detailed contribution of different atmospheric constituents to the total absorption in the 3.8-4.0μm spectral region at θ=83°

REPORT DOCUMENTATION PAGE

Form Approved OMB No. 0704-0188

1. AGENCY USE ONLY (Leave blank)	2. REPORT DATE	3. REPORT TYPE AND DATES COVERED
	June 1999	Final Report

4. TITLE AND SUBTITLE

Comparison of Atmospheric Transmittance Measurements in the 3-5μm and 8-12μm Spectral Regions with MODTRAN: Consideration for Long Path Geometries Applicable for Space-to-Ground Defense Theatre

5. FUNDING NUMBERS

F61775-98-WE082

6. AUTHOR(S)

Dr. Adam Devir

7. PERFORMING ORGANIZATION NAME(S) AND ADDRESS(ES)

IARD - Institute for Advanced Research and Development
Industry Park Tel-Hanan
Nesher, POB 271 20 302
Israel

8. PERFORMING ORGANIZATION REPORT NUMBER

N/A

9. SPONSORING/MONITORING AGENCY NAME(S) AND ADDRESS(ES)

EOARD
PSC 802 BOX 14
FPO 09499-0200

10. SPONSORING/MONITORING AGENCY REPORT NUMBER

SPC 98-4042

11. SUPPLEMENTARY NOTES

12a. DISTRIBUTION/AVAILABILITY STATEMENT

Approved for public release; distribution is unlimited.

12b. DISTRIBUTION CODE

A

13. ABSTRACT (Maximum 200 words)

This report results from a contract tasking IARD - Institute for Advanced Research and Development as follows: The contractor will investigate atmospheric transmittance under desert conditions to test the predictions of MODTRAN for the 3-5um and 8-12um spectral regions.

14. SUBJECT TERMS

EOARD, Sensor Technology, Atmospheric Science, Atmospheric Transmission

15. NUMBER OF PAGES

77

16. PRICE CODE

N/A

17. SECURITY CLASSIFICATION OF REPORT	18. SECURITY CLASSIFICATION OF THIS PAGE	19. SECURITY CLASSIFICATION OF ABSTRACT	20. LIMITATION OF ABSTRACT
UNCLASSIFIED	UNCLASSIFIED	UNCLASSIFIED	UL